TABLE OF CONTENTS

3. AIRFOIL THEORY

The purpose of this chapter is to present the reader with some fundamental knowledge of and practical limitations to airfoil (=section) aerodynamic behavior.

Basic geometric parameters used in describing airfoils are discussed in Section 3.1.

A discussion of the fundamental aerodynamic force behavior of airfoils including a corresponding non-dimensional parameter analysis is given in Section 3.2.

The most important aspects of section lift, drag and pitching moment behavior and mathematical modelling are the subject of Section 3.3.

The resultant force and moment coefficients (lift, drag and pitching moment) are the result of integrating the section pressure distribution. Section 3.4 presents a discussion of section pressure distributions.

The aerodynamic behavior of airfoil sections is very much affected by Mach number, i.e. by compressibility effects. Section 3.5 contains a basic discussion of compressibility.

Aerodynamic behavior of airfoil sections is also strongly affected by Reynolds number, i.e. by viscous effects. A discussion of Reynolds number effects is given in Section 3.6.

It is feasible in the current state of the art of aerodynamic computational theory to "design" airfoil shapes to meet certain prespecified behavior in lift, drag and pitching moment. A fundamental discussion of the effect of basic geometric airfoil parameters on airfoil performance is given in Section 3.7.

Because of the importance of section maximum lift coefficient in airplane design (wing and tail) a separate discussion on this subject is included in Section 3.8.

3.1 AIRFOIL GEOMETRY

An airfoil is a streamlined body which, when set at a suitable angle of attack, produces more lift than drag. The NACA (National Advisory Committee for Aeronautics and NASA's predecessor*) has developed and tested many series of airfoils, which are still being used today. Ref. 3.1 contains a systematic listing of the most

*NASA - National Aeronautics and Space Administration

important NACA airfoils. The geometrical features of airfoil sections are defined in the following, referring to Fig. 3.1.

Mean camber line is the line joining the midpoints between the upper and lower surfaces of an airfoil and measured normal to the mean camber line. Normally, the measurement can be made perpendicular to the chord line within acceptable engineering accuracy.

Chord line is the line joining the endpoints of the mean camber line.

Thickness is the height of profile measured normal to the chord line. The maximum thickness to chord ratio, t/c, is called the thickness ratio.

Camber is the maximum distance of the mean camber line from the chord line.

Leading-edge radius is the radius of a circle, tangent to the upper and lower surfaces, with its center located on a tangent to the mean camberline drawn through the leading edge of this line.

3.2 AERODYNAMIC FORCES AND MOMENTS ON AN AIRFOIL

When an airfoil is placed in a moving stream of air, an aerodynamic force acting on it will be created. Experimentally, this force (F) has been found to depend on the following variables: velocity of air, V; air density, ρ; characteristic area or size, S; coefficient of dynamic viscosity, μ; speed of sound (compressibility effect), V_a and angle of attack, α. To find the general form of dependence, a dimensional analysis may be used. Since there are six dimensional variables (F, V, ρ, S, μ, V_a), three dimensionless parameters can be found according to Buckingham's π - theorem*. Using V, ρ, and S as the repeating variables, the first dimensionless parameter may be written as:

$$\pi_1 = V^a \rho^b S^d F \tag{3.1}$$

In terms of the fundamental units: length, ℓ; time, t and mass, m; Eqn. (3.1) becomes:

$$\text{Dim}\pi_1 = \left(\frac{\ell}{t}\right)^a \left(\frac{m}{\ell^3}\right)^b (\ell^2)^d \left(\frac{m\ell}{t^2}\right) \tag{3.2}$$

Because π_1 is dimensionless, equating powers of like variables yields:

*Ref. 3.2, p. 183 and Ref. 3.3.

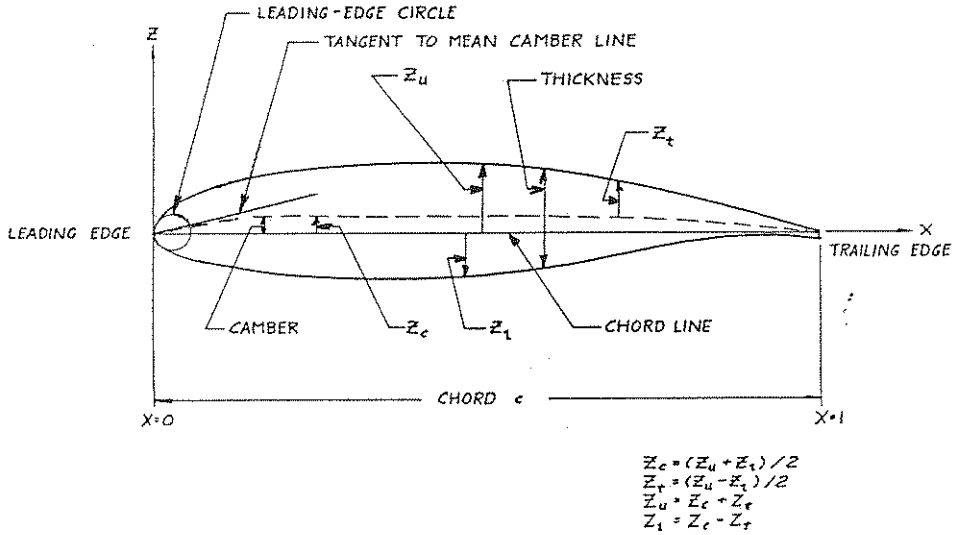

Figure 3.1 Definition of Airfoil Geometry

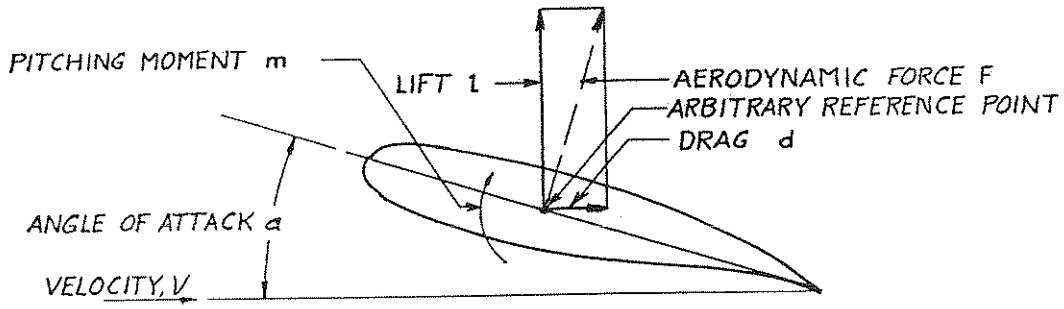

Figure 3.2 Definition of Section Forces and Moment

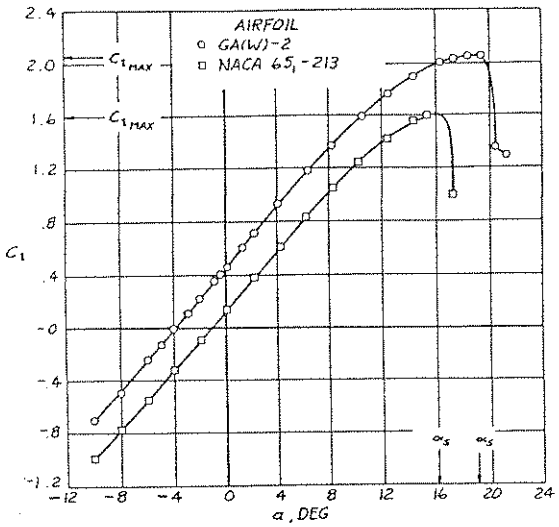

Figure 3.3 Example of Airfoil Lift Curve Slopes (Taken from Ref. 3.10)

57

for m: $0 = b + 1$

for ℓ: $0 = a - 3b + 2d + 1$ (3.3)

for t: $0 = -a - 2$

Solving the above equations simultaneously for a, b and d, it is obtained that $a = -2$, $b = -1$ and $d = -1$. Hence:

$$\pi_1 = F/\rho\, V^2 S \tag{3.4}$$

Similarly, the second dimensionless parameter can be written as:

$$\pi_2 = V^a \rho^b S^d \mu \tag{3.5}$$

From this it follows that:

$$\text{Dim}\pi_2 = (\frac{\ell}{t})^a (\frac{m}{\ell^3})^b (\ell^2)^d (\frac{m}{\ell t}) \tag{3.6}$$

Equating powers of like variables yields:

for m: $0 = b + 1$

for ℓ: $0 = a - 3b + 2d - 1$ (3.7)

for t: $0 = - a - 1$

Solving for a, b and d it is found that $a = -1$, $b = -1$ and $d = -\frac{1}{2}$, so that:

$$\pi_2 = \frac{\mu}{\rho V S^{\frac{1}{2}}} \tag{3.8}$$

By following the same procedure, the third parameter can be shown to be:

$$\pi_3 = \frac{V_a}{V} \tag{3.9}$$

According to the π-theorem, the dimensionless relation governing the aerodynamic forces can now be written as:

$$F/\rho\, V^2 S = f'(\frac{\mu}{\rho V S^{\frac{1}{2}}},\ \frac{V_a}{V},\ \alpha) \tag{3.10}$$

Replacing $S^{\frac{1}{2}}$ by c, a linear dimension, two important parameters can now be identified:

$$M = \text{Mach number} = \frac{V}{V_a} \tag{3.11}$$

and:

$$R_N = \text{Reynolds number} = \frac{\rho V c}{\mu} \tag{3.12}$$

Hence:

$$F = \rho V^2 S \, f(R_N, M, \alpha) \tag{3.13}$$

For airfoils, let S = c x 1, or the area per unit span. For the force component in the direction perpendicular to the freestream, i.e., the lift force, it is convenient to introduce:

$$f(R_N, M, \alpha) = \frac{c_\ell}{2} \tag{3.14}$$

It follows that Eqn. (3.12) is reduced to its conventional form:

$$\ell = c_\ell \tfrac{1}{2}\rho V^2 c = c_\ell \bar{q} c \tag{3.15}$$

where c_ℓ is the sectional lift coefficient and $\bar{q}$ is the dynamic pressure. Similarly, for the force component in the freestream direction, i.e., the drag force, it follows that:

$$d = c_d \bar{q} c \tag{3.16}$$

From this derivation, it is obvious that the lift and drag coefficients, c_ℓ and c_d, are functions of α, R_N and M. By the same process, a moment coefficient c_m can also be defined so that the pitching moment is computed as:

$$m = c_m \bar{q} c^2 \tag{3.17}$$

where c_m is regarded as positive if the moment is nose-up. Fig. 3.2 defines ℓ, d, m and F in relation to an airfoil at angle of attack, α.

Note that ℓ is the lift force in lb/ft, d is the drag force in lb/ft and m is the pitching moment in ft-lb/ft. This is so because the span was taken to be unity.

3.3 IMPORTANT AIRFOIL CHARACTERISTICS

The following relationships are of fundamental importance to airplane design and airplane performance analysis:

3.3.1 Lift Curve: c_ℓ versus α

3.3.2 Drag Polar: c_ℓ versus c_d

3.3.3 Pitching Moment Curve: c_m versus α or c_m versus c_ℓ

Examples of these relations are now discussed.

3.3.1 LIFT CURVE: c_ℓ VERSUS α

Typical lift curves are shown in Fig. 3.3. The linear portion of the lift curve can be represented mathematically by the equation:

$$c_\ell = a(\alpha - \alpha_o)$$

or: (3.18)

$$c_\ell = c_{\ell_\alpha}(\alpha - \alpha_o)$$

where "a" or "c_{ℓ_α}" is the lift curve slope and α_o the angle of attack for zero lift. The theoretical value of "a" is 2π per radian (Ref. 3.1, p. 69). However, experiments show small deviations from this value, depending on airfoil shape.

In the nonlinear range it is seen that a definite maximum value of section c_ℓ, called $c_{\ell_{max}}$ is reached. At that value the airfoil is said to be stalled. Section 3.8 presents a detailed discussion of airfoil $c_{\ell_{max}}$ and stall behavior.

3.3.2 DRAG POLAR: c_ℓ VERSUS c_d

Typical drag polars are shown in Fig. 3.4. An important parameter representing the aerodynamic efficiency of airfoils is the lift-drag ratio. The maximum c_ℓ/c_d magnitude can be obtained by drawing a tangent to the c_d-c_ℓ curve. Another important feature is the magnitude of c_ℓ for which $(c_\ell/c_d)_{max}$ occurs. The importance of this feature is illustrated in Chapters 8-12.

3.3.3 PITCHING MOMENT CURVE: c_m VERSUS α or c_m VERSUS c_ℓ

Figure 3.5 shows typical airfoil c_m-curves. The magnitude of c_m depends on the location of the moment center. One important moment center which is often used is the so-called aerodynamic center (a.c.). It is defined as the point about which the moment coefficient is independent of α. To find the a.c., assume that the moment center in an experimental set-up is at a distance x from the leading edge and the corresponding moment coefficient is c_{m_x}. Fig. 3.6 illustrates the geometry. Ignoring the drag effect it follows that:

$$c_{m_{ac}} \bar{q}c^2 = c_{m_x} \bar{q}c^2 + c_\ell \bar{q}c(x_{ac} - x) \qquad (3.19)$$

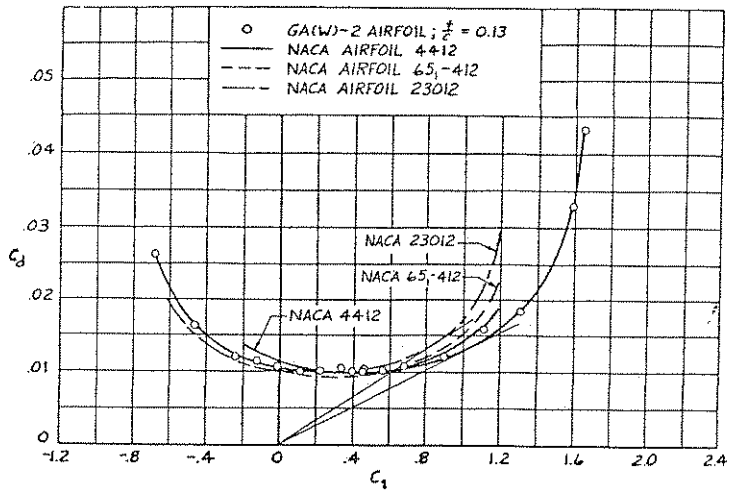

Figure 3.4 Examples of Airfoil Drag Polars. M = 0.15, R_N = 6.0 x 10^6 (Taken from Ref. 3.10)

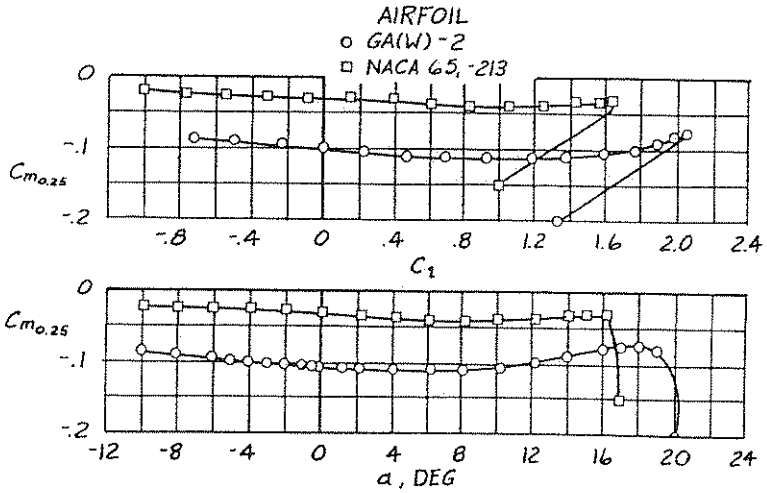

Figure 3.5 Example of Pitching Moment Curves (Taken from Ref. 3.10)

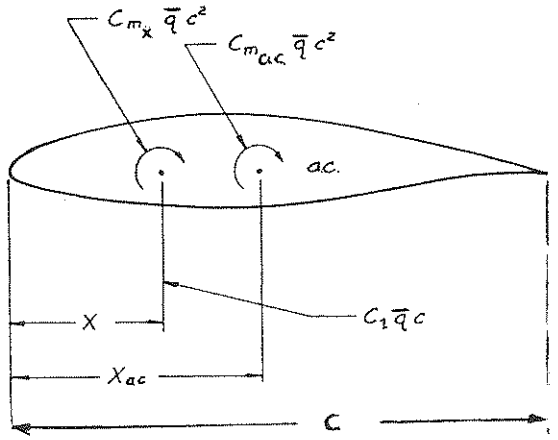

Figure 3.6 Geometry for Finding the Aerodynamic Center

61

or:

$$c_{m_{ac}} = c_{m_x} + c_\ell \frac{x_{ac} - x}{c} \tag{3.20}$$

Since $c_{m_{ac}}$ is independent of α, $dc_{m_{ac}}/d\alpha = 0$. Hence Eqn. (3.20) gives:

$$0 = \frac{\partial c_{m_x}}{\partial \alpha} + \frac{\partial c_\ell}{\partial \alpha}\left(\frac{x_{ac}}{c} - \frac{x}{c}\right) \tag{3.21}$$

from which it follows that:

$$\frac{x_{ac}}{c} = \frac{x}{c} - \frac{\partial c_{m_x}}{\partial c_\ell} \tag{3.22}$$

Therefore, the a.c. can be located by using the experimental c_{m_x}-c_ℓ curve and $c_{m_{ac}}$ computed with Eqn. (3.20). It is found that in low subsonic flow, the aerodynamic center of many airfoils is roughly at the .25 chord point.

3.4 AIRFOIL PRESSURE DISTRIBUTION

The pressure distribution over an airfoil is important in load distribution calculations and control surface hinge-moment calculations. The pressure distribution is normally expressed in terms of the so-called pressure coefficient C_p which is defined as:

$$C_p = \frac{p - p_\infty}{\frac{1}{2}\rho_\infty V_\infty^2} = \frac{p - p_\infty}{\bar{q}_\infty} \tag{3.23}$$

At low speeds, Eqn. (3.23) gives, according to the incompressible Bernoulli Equation (Eqn. 2.10),

$$C_p = 1 - \left(\frac{V}{V_\infty}\right)^2 \tag{3.24}$$

Eqn. (3.24) shows that $C_p = 1.0$ at a stagnation point ($V = 0$). An example of a typical low speed pressure distribution on an airfoil is shown in Fig. 3.7. The effect of angle of attack and of control surface deflection on airfoil pressure distribution is illustrated in Fig. 3.8. It is seen that there is a pressure peak near the leading edge due to the angle of attack and another pressure peak at the hinge due to control surface deflection. By integrating the measured pressure distribution properly, c_ℓ and c_d can be obtained. The force coefficients c_z and c_x follow from:

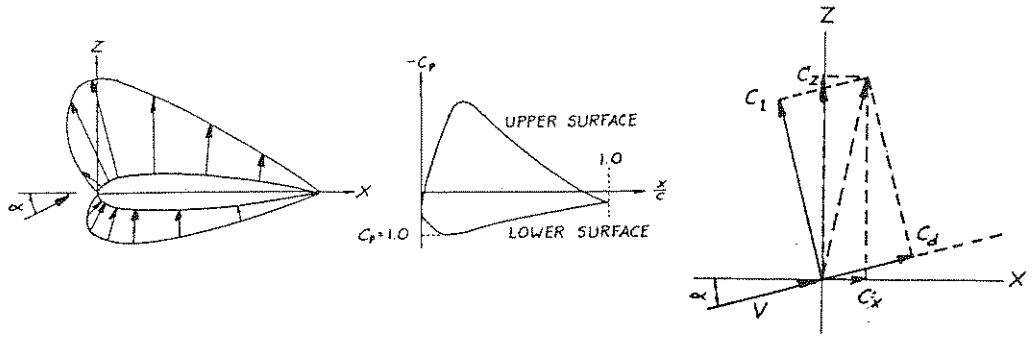

Figure 3.7 Example of a Low Speed Pressure Distribution

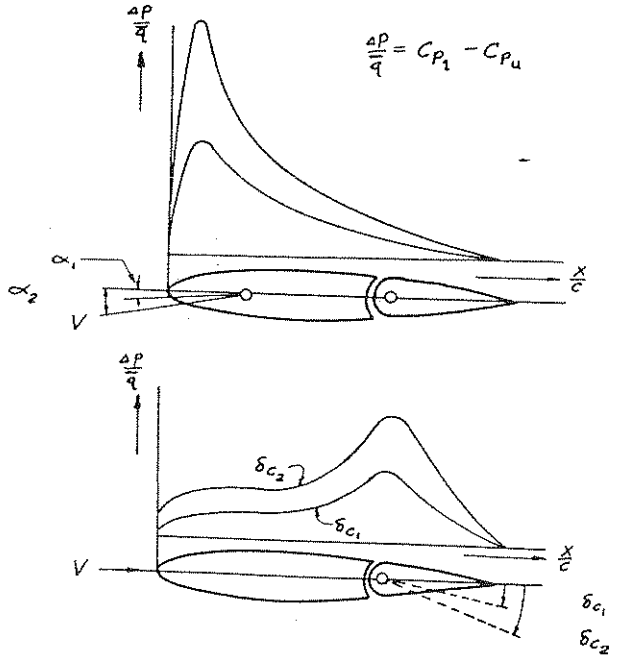

Figure 3.8 Examples of the Effect of α and δ_c on Pressure Distributions

$$c_z = \frac{Z}{\bar{q}c} = \int_o^1 (C_{p_\ell} - C_{p_u}) d(\frac{x}{c})$$

$$c_x = \frac{X}{\bar{q}c} = \int_o^1 (C_{p_\ell} - C_{p_u}) d(\frac{z}{c}) \qquad (3.25)$$

From these it is possible to compute c_ℓ and c_d as:

$$c_\ell = c_z \cos\alpha - c_x \sin\alpha$$

$$c_d = c_z \sin\alpha + c_x \cos\alpha \qquad (3.26)$$

The relation between c_ℓ, c_d, c_y and c_x is also illustrated in Fig. 3.7.

The pitching moment coefficient relative to the leading edge can be computed as:

$$c_{m_{l.e.}} = \int_o^1 (C_{p_\ell} - C_{p_u}) \frac{x}{c} d(\frac{x}{c}) \qquad (3.27)$$

3.5 COMPRESSIBILITY EFFECTS

Due to the variation of local velocity over the curved surface of the airfoil, the local Mach number of the flow varies considerably from that in the freestream. By increasing the freestream Mach number at a given α, eventually a freestream Mach number is reached at which sonic speed occurs on the airfoil surface. Such a freestream Mach number is called the critical Mach number.

From the compressible Bernoulli equation (Eqn. 2.36) it follows that:

$$\frac{V^2}{2} - \frac{V_\infty^2}{2} = -\frac{1}{\gamma-1}(\frac{\gamma p}{\rho} - \frac{\gamma p_\infty}{\rho_\infty})$$

$$= \frac{\gamma p_\infty}{\rho_\infty(\gamma-1)}(\frac{p}{\rho}\frac{\rho_\infty}{p_\infty} - 1)$$

$$= -\frac{\gamma}{\gamma-1}\frac{p_\infty}{\rho_\infty}[\frac{p}{p_\infty}(\frac{p}{p_\infty})^{\frac{-1}{\gamma}} - 1]$$

$$= -\frac{\gamma}{\gamma-1}\frac{p_\infty}{\rho_\infty}[(\frac{p}{p_\infty})^{\frac{\gamma-1}{\gamma}} - 1] = -\frac{V_{a_\infty}^2}{\gamma-1}[(\frac{p}{p_\infty})^{\frac{\gamma-1}{\gamma}} - 1] \qquad (3.28)$$

But from Eqn. (3.23):

$$\frac{p}{p_\infty} = 1 + \frac{C_p \bar{q}_\infty}{p_\infty} = 1 + \frac{\gamma C_p M_\infty^2}{2}$$

Therefore it follows that:

$$V^2 = V_\infty^2 - \frac{2V_{a_\infty}^2}{\gamma-1}\left[\left(1 + \frac{\gamma C_p M_\infty^2}{2}\right)^{\frac{\gamma-1}{\gamma}} - 1\right] \tag{3.29}$$

To find the critical Mach number, the expression for local speed of sound is needed:

$$V_a^2 = \frac{\gamma p}{\rho} = \frac{\gamma p_\infty}{\rho_\infty}\,\frac{p}{p_\infty}\,\frac{\rho_\infty}{\rho} = V_{a_\infty}^2\left(\frac{p}{p_\infty}\right)^{\frac{\gamma-1}{\gamma}} = V_{a_\infty}^2\left(1 + \frac{\gamma C_p M_\infty^2}{2}\right)^{\frac{\gamma-1}{\gamma}} \tag{3.30}$$

At the critical condition, Eqns. (3.29) and (3.30) are equated to solve for the critical pressure coefficient:

$$C_{p_{cr}} = \frac{2}{\gamma M_\infty^2}\left\{\left[\frac{M_\infty^2(\gamma-1) + 2}{\gamma + 1}\right]^{\frac{\gamma}{\gamma-1}} - 1\right\} \tag{3.31}$$

Eqn. (3.31) gives the value of C_p at that point on the airfoil where sonic velocity is first reached for a given free stream Mach number. This expression can be used to determine the critical Mach number of an airfoil at a given α. Assume that at $M_\infty = 0$, the most negative pressure on the airfoil is given by C_{p_o}. According to Glauert*, the pressure coefficient at the same point and same α but for another M_∞ is approximately given by:

$$C_p = \frac{C_{p_o}}{\sqrt{1 - M_\infty^2}} \tag{3.32}$$

where $\sqrt{1 - M_\infty^2}$ is known as the Prandtl-Glauert Transformation Factor. A more accurate formula was given by von Kármán and Tsien:**

---

*Ref. 3.1, p.256

**Ref. 3.1, p. 258

$$C_p = \frac{C_{p_o}}{\sqrt{1 - M_\infty^2} + \frac{C_{p_o} M_\infty^2}{2(\sqrt{1 - M_\infty^2} + 1)}} \tag{3.33}$$

By plotting Eqns. (3.31) and (3.32) or (3.33) simultaneously, the critical Mach number may be obtained as the corresponding Mach number at the intersection. This is illustrated in Fig. 3.9.

Since the lift coefficient of an airfoil is found by integrating C_p around the airfoil, it is seen that from Prandtl-Glauert's formula (3.32):

$$c_\ell = \frac{c_{\ell_o}}{\sqrt{1 - M_\infty^2}} \tag{3.34}$$

Similarly, the lift curve slope is estimated by Prandtl-Glauert's rule:

$$a = \frac{a_o}{\sqrt{1 - M_\infty^2}} \tag{3.35}$$

Prandtl-Glauert's formula and Kármán-Tsien's are valid only below M_{cr}. Because the lift curve slope is increased, the lift curves of airfoils at different subsonic M_∞ are as shown in Fig. 3.10.

With further increase in freestream Mach number beyond the critical value, a supersonic region on the upper surface will appear. Eventually, a strong enough shock wave will terminate the supersonic region and may even separate the boundary layer. This is illustrated in Fig. 3.11. Due to shock induced flow separation, the drag coefficient will increase sharply. The freestream Mach number at which $\partial c_d / \partial M = 0.1$ has been defined as the drag divergence Mach number (M_{dd}). This is the so-called Douglas-definition. Another definition of drag-divergence Mach number is the so-called Boeing-definition. This latter is that Mach number for which $\Delta c_d = .0020$ above the incompressible drag level. Both definitions are illustrated in Fig. 3.12.

Airfoils designed for transonic cruise applications should have as high a drag divergence Mach number as possible. Typical examples of actual dragrise data of some airfoils are shown in Fig. 3.13.

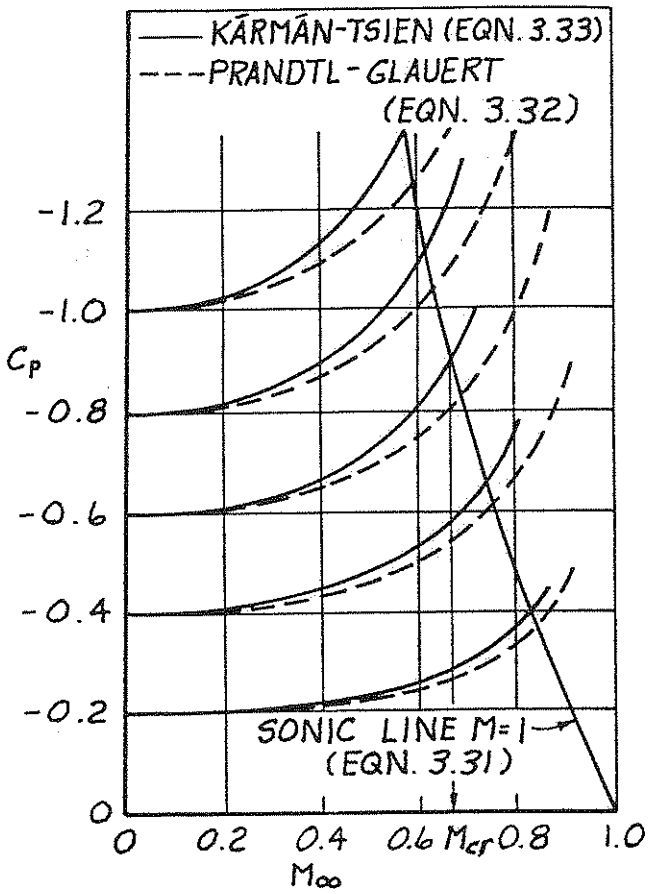

Figure 3.9 Variation of Peak Pressure (Neg.) and Critical Pressure with Free Stream Mach Number

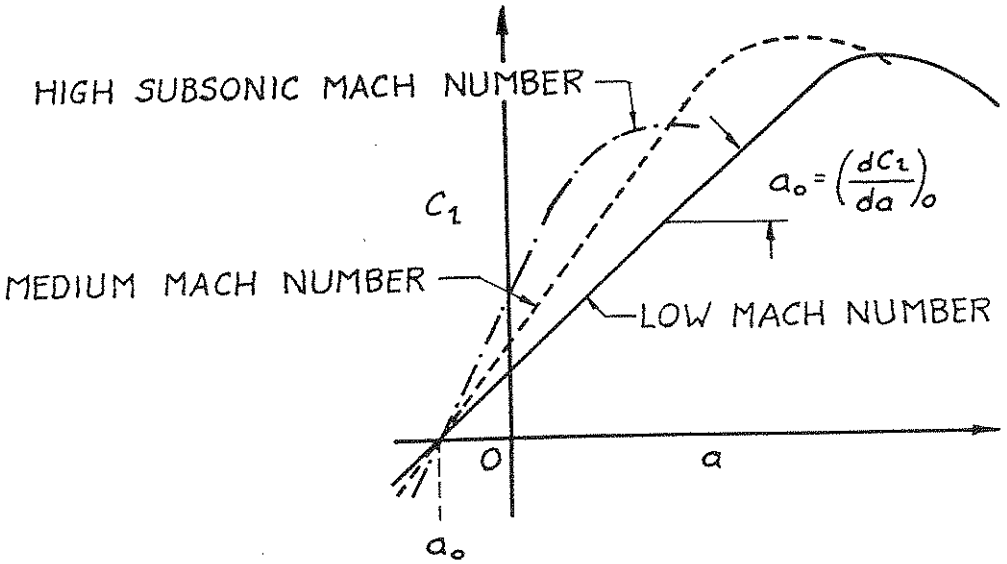

Figure 3.10 Compressibility Effect on Airfoil Lift Curve Slope

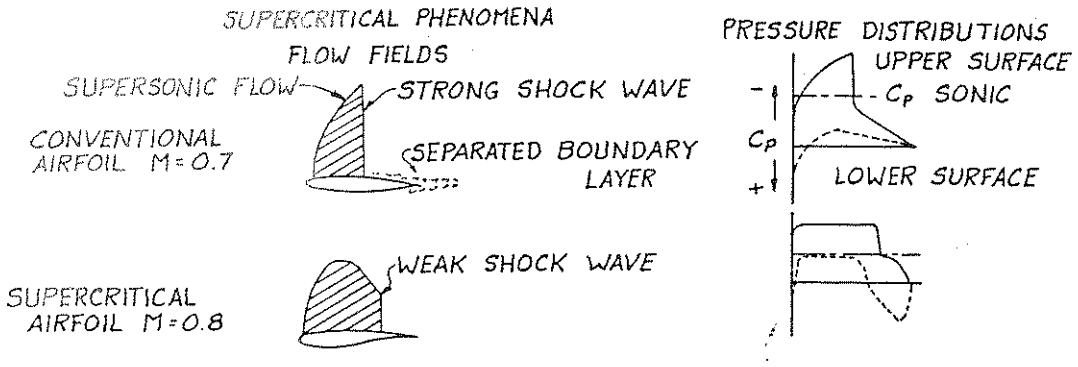

Figure 3.11 Illustration of Occurrence of Shocks on Airfoils

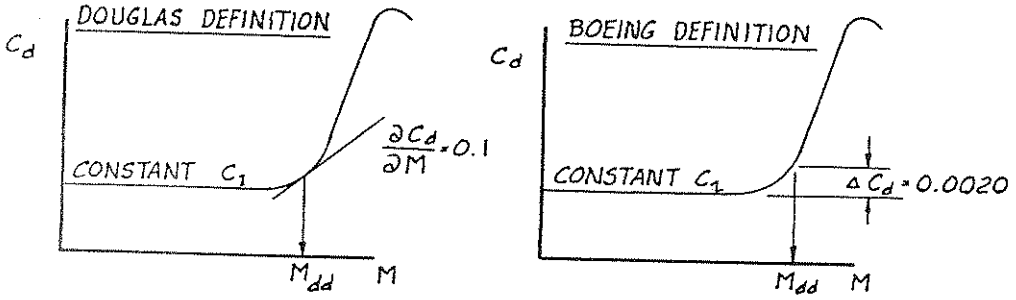

Figure 3.12 Definition of Drag Divergence Mach Number, M_{dd}

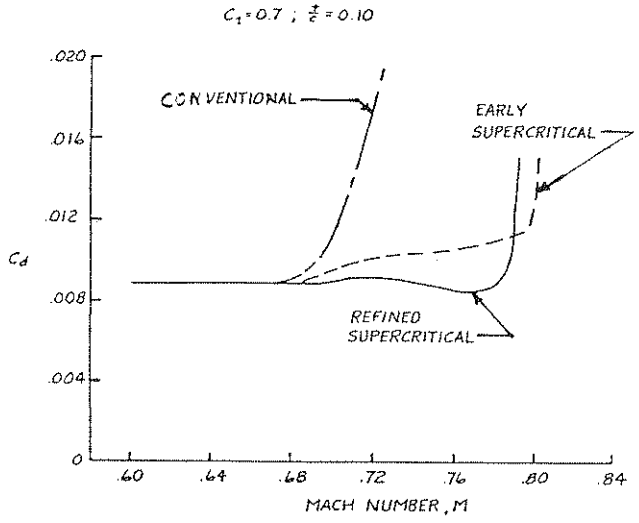

Figure 3.13 Example of Typical Airfoil Drag Rise Data

3.6 REYNOLDS NUMBER EFFECTS

Due to the large difference in Reynolds number between wind tunnel and full-scale flight, the model boundary layer characteristics will not correctly simulate those of the full scale airplane thereby creating some obvious variations in aerodynamic forces. While the boundary layer on a full-scale wing is often mostly turbulent, extensive regions of laminar flow may exist on a wind tunnel model at a low Reynolds number. The most noticeable effect of Reynolds number is on the drag level and on the maximum lift coefficient. Therefore, it is essential to simulate the full-scale fully turbulent condition on the model surface before the model data can be extrapolated. The standard practice is to use a so-called trip-strip located at 5% to 10% chord. Such a trip-strip consists of a narrow band of distributed roughness of known grit-size. Fig. 3.14 illustrates an example of trip-strips on a tunnel model. Ref. 3.4 can be used as a guide in determining the location and grit-size of the trip-strip.

Experiments in subsonic flow indicated that if narrow, sparsely distributed, bands of roughness are used, the measured minimum drag is nearly unchanged for any roughness height less than the boundary layer thickness (Ref. 3.5). This implies that a proper choice of roughness grit can provide essentially a zero drag penalty due to roughness itself as long as the transition occurs. For the transition to occur, the roughness size for a given wind-tunnel Reynolds number based on the roughness height should be at least 600.

Once the boundary layer characteristics have been correctly simulated, the Reynolds number correction can be applied as follows. The minimum profile drag coefficient can be written as:

$$c_{d_{min}} = (S.F.) \times 2C_f \tag{3.36}$$

where C_f is the skin friction coefficient of a flat plate with the same transition location as the airfoil. The shape factor (S.F.) represents the effect of thickness and the associated viscosity effects. For a fully turbulent boundary layer, C_f may be calculated according to Schlichting's formula (Eqn. 2.97):

$$C_f = \frac{0.455}{(\log_{10} R_N)^{2.58}} \tag{3.37}$$

Several forms of the shape factor are in existence. Hoerner (Ref. 3.6, p. 6-6) has shown, from a collection of early data, that the shape factor for sections with maximum thickness at 30% chord can be represented empirically as:

$$S.F. = 1 + 2\left(\frac{t}{c}\right) + 60\left(\frac{t}{c}\right)^4 \tag{3.38}$$

Figure 3.14 Example of Trip Strip on a Wind Tunnel Model of the S211 Jet Trainer. Arrows Indicate Location of Trip Strips (Courtesy SIAI-Marchetti)

It follows that the full-scale minimum profile drag can be obtained as:

$$c_{d_{min}}\text{(full-scale)} = c_{d_{min}}\text{(model)} - \Delta c_{d_{min}} \tag{3.39}$$

where:

$$\Delta c_{d_{min}} = 2(\text{S.F.})[C_f\text{(model)} - C_f\text{(full-scale)}] \tag{3.40}$$

There are as yet no accurate theoretical methods available for correcting the maximum lift coefficient. Jacobs and Sherman have shown some experimental results for the Reynolds number effect on $c_{\ell_{max}}$ for some NACA airfoils (Ref. 3.7). Additional data can be found in Ref. 3.8. Most airplane companies have their own correction procedures for extrapolating tunnel $c_{\ell_{max}}$ to full scale. Such procedures are based upon their experience obtained in comparing model and airplane data.

3.7 DESIGN OF AIRFOILS

To design an airfoil for any specific use, the following effects of airfoil geometry should be noted:

Camber shape and thickness distribution affect the location of boundary layer transition and separation points, pressure distribution, stall characteristics, $c_{\ell_{max}}$ values, M_{dd}, c_ℓ/c_d, etc.

(1) Camber shape will affect mainly α_o and c_m. Any increase in camber will make α_o and c_m more negative.

(2) Thickness distribution will change the value of lift curve slope, a.c. location, and center of pressure location.

(3) The leading-edge shape has a pronounced effect on stall characteristics and on $c_{\ell_{max}}$.

NACA has developed several series of airfoils for various applications. The meaning of the most important airfoil designations is shown in Table 3.1. Ref. 3.1 contains a fairly complete listing of NACA airfoils including their aerodynamic characteristics.

Note that the 6-series airfoils were designed to have mean camber lines producing a uniform chordwise loading from the leading edge to x/c = a, and a linearly decreasing load from this point to the

Table 3.1 Examples of NACA Airfoil Designation

4-digit airfoils: Example NACA 4412

4 -- camber 0.04c

4 -- Position of the camber at 0.4c from L.E.

12 -- Max. thickness 0.12c

5-digit airfoils: Example NACA 23012

2 -- camber 0.02c

This design lift coefficient is 0.15 times the first digit for this series.

30 -- Position of camber at $\frac{0.30}{2}$ c = 0.15c

12 -- Max. thickness 0.12c

6-series airfoils: Example NACA 65_3 - 421

6 -- Series designation

5 -- Minimum pressure at 0.5 c

3 -- The drag coefficient is near its minimum value over a range of lift coefficient of 0.3 above and below the design lift coefficient.

4 -- design lift coefficient 0.4

21 -- max. thickness 0.21c

7-series airfoils: Example NACA 747A315

7 -- series designation

4 -- favorable pressure gradient on the upper surface from L.E. to 0.4c at the design lift coefficient.

7 -- favorable pressure gradient on the lower surface from L.E. to 0.7c at the design lift coefficient.

A -- a serial letter to distinguish different sections having the same numerical designation but different mean line or thickness distribution.

3 -- design lift coefficient 0.3

15 -- max. thickness 0.15 c

trailing edge. When this is the case, the a-value is given after the airfoil designation.

Examples are: NACA 66(215)-216, a = 0.6 and 65(318)-217, a = 0.5. The last two examples are airfoils having thickness distributions obtained by linearly increasing or decreasing the ordinates of the originally derived thickness distribution. In the last example, the airfoil has a 17% thickness ratio which was derived from the airfoil with 18% thickness distribution. The digit 3 represents in tenths, one half of the extent of the low drag range. When this digit is omitted, it implies the low drag range to be less than 0.1.

Since the late 1950's NASA has engaged in designing airfoils for transonic transport and fighter applications. These so-called supercritical airfoils have higher M_{dd} than the conventional NACA 6-series airfoils as illustrated in Fig. 3.13. These airfoils are characterized by very little camber in the forward portion. On the other hand, the rear portion is severely cambered. Fig. 3.15 presents an example.

During the course of these recent airfoil research activities, new airfoils for lower speed applications have also been derived. They are low-speed airfoils, such as LS(1)-0417 and LS(1)-0413, and medium-speed airfoils, such as MS(1)-0313. The LS(1)-0417 airfoil is popularly known as the GA(W)-1 airfoil and LS(1)-0413 is known as the GA(W)-2 airfoil. The thickness and camber line of this airfoil are compared with a 65-series airfoil in Fig. 3.16. Several key design features of this 17% thick airfoil are:

(1) A large upper surface leading-edge radius (0.06c) was used to alleviate the peak negative pressure coefficients and therefore delay airfoil stall to high angles of attack.

(2) The airfoil was contoured to provide an approximate uniform chordwise load distribution near the design lift coefficient of 0.4.

(3) A blunt trailing edge was provided with the upper and lower surface slopes approximately equal to moderate the upper surface pressure recovery and thus postpone the stall.

Test results in Refs. 3.9 (for GA(W)-1) and 3.10 (for GA(W)-2) show that $c_{\ell_{max}}$ of this type airfoils is about 30% greater than a typical older NACA 6-series airfoil and c_ℓ/c_d at $c_\ell = 0.9$ was about 50% greater. Fig. 3.17a and b show some examples. In Fig. 3.17b, the so-called NACA standard roughness is a large wrap-around roughness as compared with the narrow roughness strip now used as NASA standard.

Figure 3.15 Example of Supercritical Airfoil

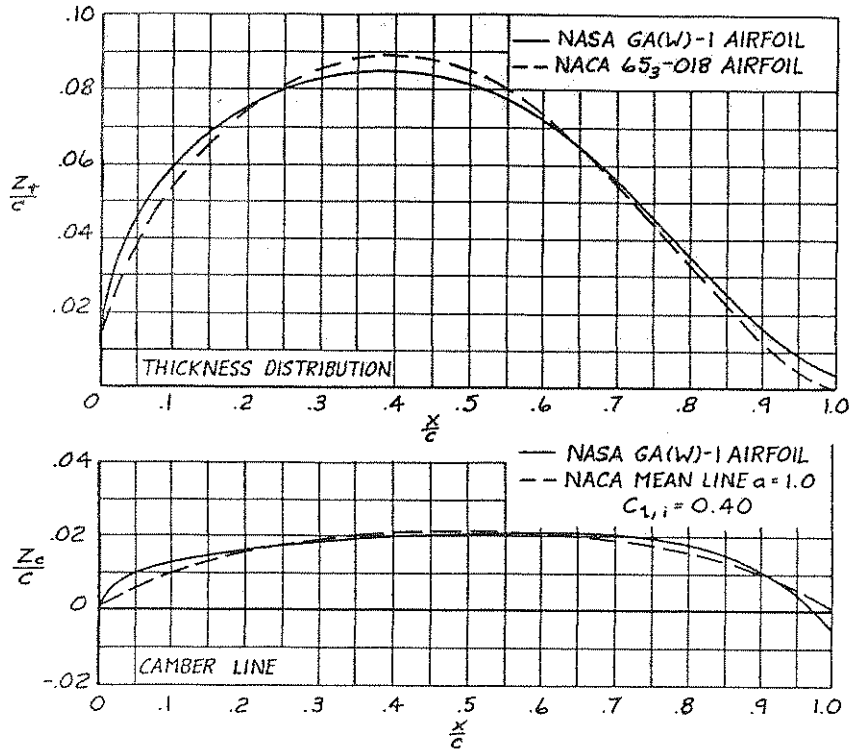

Figure 3.16 Comparison of GA(W)-1 and 65_3-018 Airfoils

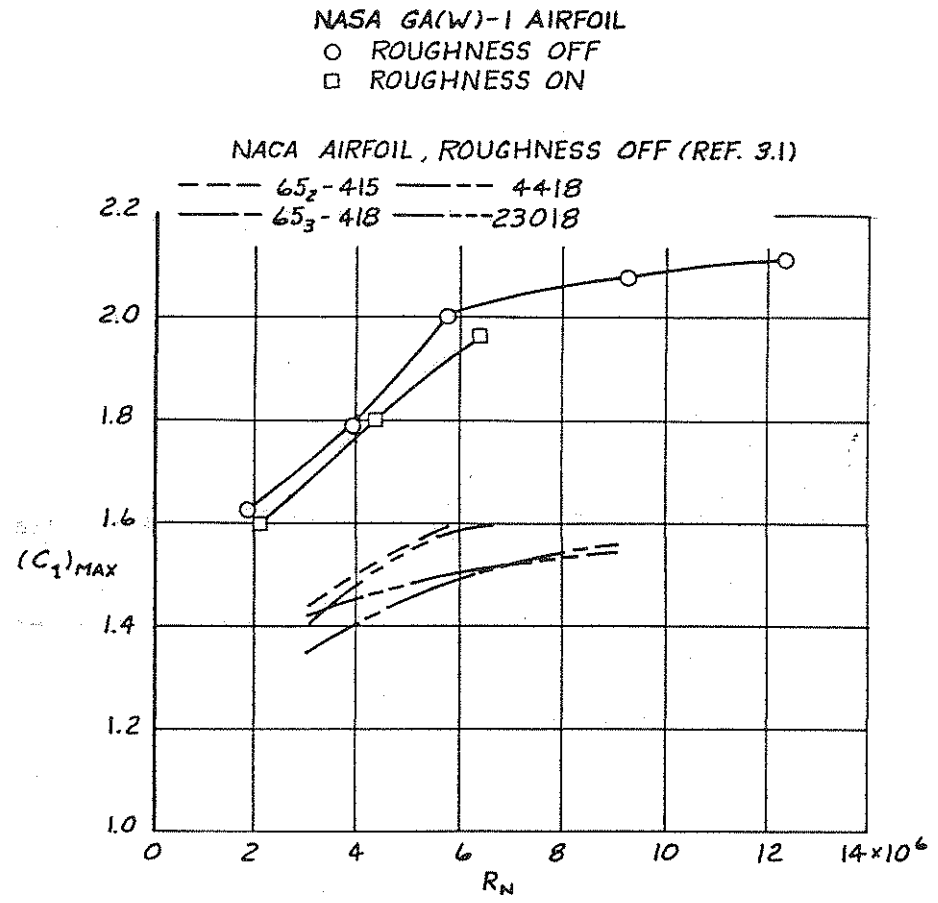

(a) VARIATION OF $C_{l\,MAX}$ WITH R_N, M=0.15

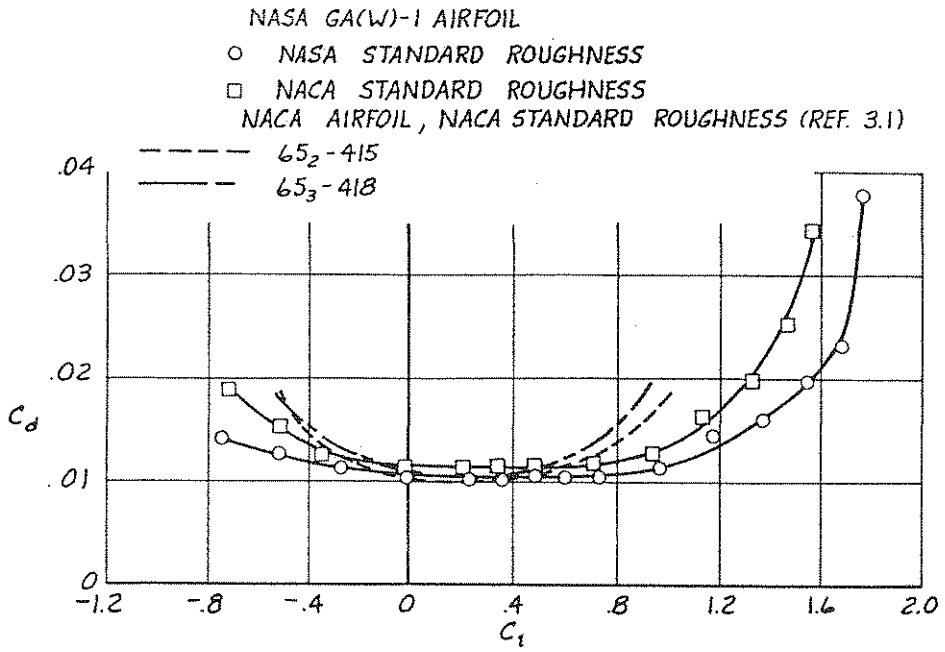

(b) VARIATION OF C_d WITH C_ℓ, M=.20, $R_N \cong 6\times10^6$

Figure 3.17 Comparison of Important Aerodynamic Characteristics of Some NACA and NASA Airfoils

In selecting an airfoil for an airplane lifting surface (wing, tail or canard) the following considerations are important:

(1) Drag (for example: to obtain the highest possible cruise speed)

(2) Lift-to-drag ratio at values of C_L important to airplane performance (for example: engine-out climb)

(3) Thickness (to obtain the lowest possible structural weight)

(4) Thickness distribution (to obtain favorable span loading and/or high fuel volume)

(5) Stall characteristics (to obtain gentle stall characteristics)

(6) Drag-rise behavior (associated with item 1).

It is evident from these six items already that airfoil selection will be based on a number of compromises between conflicting requirements.

Table 3.2 lists a number of practical airfoil applications.

3.8 AIRFOIL MAXIMUM LIFT CHARACTERISTICS

The maximum lift characteristics of an airfoil as well as the associated stall-behavior is of great importance in airplane performance.

Whenever the airflow around an airfoil separates, stall is said to have started. From a c_ℓ-α viewpoint there are two types of stall: gradual and abrupt. Fig. 3.18 shows examples of each type.

The first type is typified by a gradual stall and a shallow drop-off of c_ℓ. It frequently occurs with moderate or thick sections.

The second type is typified by an abrupt stall and is often associated with thin sections. The main features of airfoil design which affect wing stall and hence, the maximum lift coefficient, are:

a. thickness ratio
b. the leading-edge radius
c. camber
d. location of maximum thickness.

These factors will be discussed in Subsection 3.8.1.

Table 3.2 Examples of Airfoil Application

Airplane Type	Wing	Hor. Tail	Vert. Tail
Beech Bonanza	NACA 23016.5(mod) at root NACA 23012(mod) at tip -3° twist	NACA 0009	NACA 0009
Beech Queen Air B80	NACA 23020 at root NACA 23012 at tip -3° 54' twist	NACA 0009	NACA 0009
Beech Skipper	NASA GAW-1	NACA 0009	NACA 0009
Beech Duchess	NAGA 63_2A415(mod) at root	NACA 0009	NACA 0009
Cessna Centurion	NACA 64_2A215 at root NACA 64_1A412 at tip -3° twist	NACA 0009	NACA 0009
Cessna T-37	NACA 2418 at root NACA 2412 at tip	NACA 0012	NACA 0012
Cessna 337 Skymaster	NACA 2412 at root NACA 2409 at tip -2° twist	NACA 0009	NACA 0009
Cessna 500 Citation	NACA 23014(mod) at root NACA 23012 at tip -3° twist	NACA 0009 -	NACA 0009
Piper PA-23 Aztec	USA*35-B(mod) t/c = 14% -2.5° twist	NACA 0009	NACA 0009
Piper PA-31T Cheyenne	NACA 63_2-415 at root NACA 63A212 at tip -2.5° twist	NACA 0009	NACA 0009
Lockheed 1329-25 Jetstar II	NACA 63A112 at root NACA 63A309 at tip -2° twist	NACA 0009	NACA 0009
LTV A-7 Corsair	NACA 65A007	Not Av.	Not Av.
Northrop F-5A	NACA 65A 004.8(mod)	Not Av.	Not Av.
Boeing 747	Boeing Airfoil t/c = 13.44% inbd 7.8% midspan 8% tip	Not Av.	Not Av.
McDonnell Douglas DC-10	Douglas Airfoil t/c = 12.2% inbd 8.4% tip	Not Av.	Not Av.

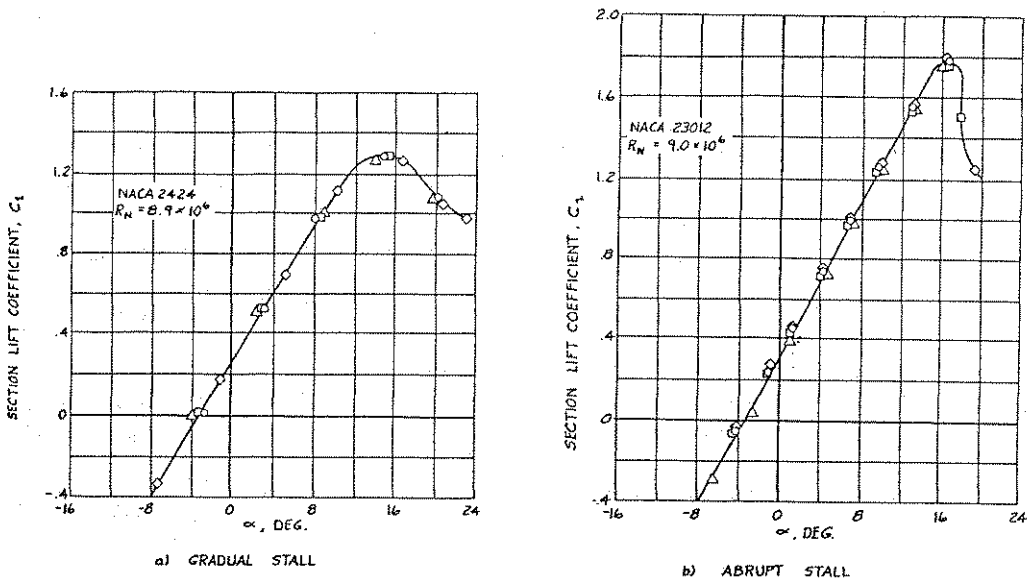

Figure 3.18 Example of Gradual and Abrupt Airfoil Stalls

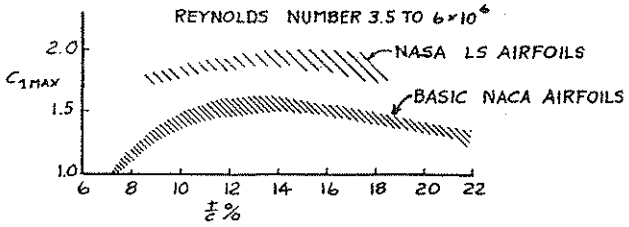

Figure 3.19 Trends of Best Maximum Lift Values of NACA Sections vs. Thickness Ratio

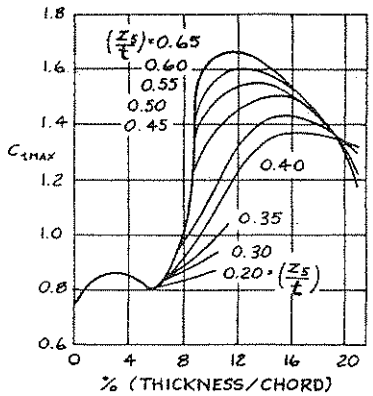

Figure 3.20 Variation of Maximum Lift Coefficient with Geometry of NACA Symmetrical Airfoils, RN = 6 x 10^6

3.8.1 GEOMETRIC FACTORS AFFECTING AIRFOIL MAXIMUM LIFT AT LOW SPEEDS

3.8.1.1 Thickness Ratio

Fig. 3.19 shows how airfoil $c_{\ell_{max}}$ is affected by airfoil thickness ratio, t/c. Note that for a given thickness ratio, $c_{\ell_{max}}$ very much depends on the leading-edge radius. Fig. 3.19 indicates that the new NASA LS(=low speed) airfoils have much higher $c_{\ell_{max}}$ than conventional NACA airfoils. For the NACA airfoils, a thickness ratio of about 13% will produce the best value of maximum lift. For the newer LS airfoils the maximum lift occurs at around 15% thickness.

3.8.1.2 Leading Edge Radius

Fig. 3.20 summarizes the data of NACA symmetrical airfoils (Ref. 3.11). It shows that $c_{\ell_{max}}$ depends not only on the thickness ratio, but also on the ratio of section thickness at 5% chord to the maximum thickness (z_5/t). The ratio (z_5/t) is indicative of leading-edge radius. Therefore, a relatively large leading-edge radius is beneficial to producing large $c_{\ell_{max}}$ at low speeds.

3.8.1.3 Camber and Location of Maximum Thickness

Experimental data showed that the maximum lift coefficient of a cambered section depends not only on the amount of camber and camber line shape, but also on the thickness and nose radius of the section on which it is used. In general, the addition of camber is always beneficial to $c_{\ell_{max}}$ and the benefit grows with increasing camber. The increment to maximum lift due to camber is least for sections with relatively large radius leading edges (i.e. the benefit of camber grows with reducing z_5/t); and camber is more effective on thin sections than on thick sections. In addition, a forward position of maximum camber produces higher values of $c_{\ell_{max}}$. For example, the NACA 23012 airfoil (with 2% maximum camber at 0.15 chord) has a $c_{\ell_{max}}$ of 1.79 as compared with 1.67 for NACA 4412 (with 4% camber at 0.4 chord but the same thickness distribution) at a Reynolds number of 9×10^6.

3.8.2 EFFECT OF REYNOLDS NUMBER ON AIRFOIL MAXIMUM LIFT

For airfoils with moderate thickness ratio, there is a significant increase in $c_{\ell_{max}}$ with increasing Reynolds number. See Fig. 3.17a. On the other hand, for thin airfoils the effect of Reynolds number is relatively insignificant. In general, these Reynolds number effects are less for cambered than for symmetrical sections. At low Reynolds number, the effect of camber is more significant. The opposite is true at Reynolds numbers greater than 6×10^6, where camber loses some of its effect.

3.8.3 EFFECT OF HIGH LIFT DEVICES ON AIRFOIL MAXIMUM LIFT

The airfoil maximum lift coefficient can be largely increased by using high lift devices. In the following, effects of trailing-edge flaps, leading-edge devices and boundary layer control (BLC) on $c_{\ell_{max}}$ will be discussed.

3.8.3.1 Trailing-Edge Flaps

(a) Plain Trailing-Edge Flaps

Plain trailing-edge flaps are formed by hinging the rear-most part of the wing section about a point within the contour, as shown in Fig. 3.21a. Downward deflection is regarded as positive. The main effect produced by the flap deflection is an increase in the effective camber of the wing. The resulting lift curve is compared with that of the plain wing in Fig. 3.22. The flap also makes the angle of zero lift more negative without significantly changing the lift-curve slope. However, the stall angle is reduced. The drag coefficient will be increased such as to reduce the lift-drag ratio. The pitching moment will be more negative. For most commonly used wing sections, the deflection angle can be increased up to 15 deg. without flow separation on the surface. Generally, $c_{\ell_{max}}$ increases with deflection of this flap up to about 60 to 70 degrees for flap chord ratios less than 0.3.

It should be emphasized that conventionally $c_{\ell_{max}}$ values are based on the flap-up chord!

It should be remembered that leaving a gap between the airfoil and the flap at the hinge line can result in severe loss in flap effectiveness. This is because the gap allows the high pressure air on the lower surface to leak through to the low pressure region on the upper surface. It has been observed that a gap of 1/300th of the chord resulted in a loss of 0.35 in $c_{\ell_{max}}$ (Ref. 3.11).

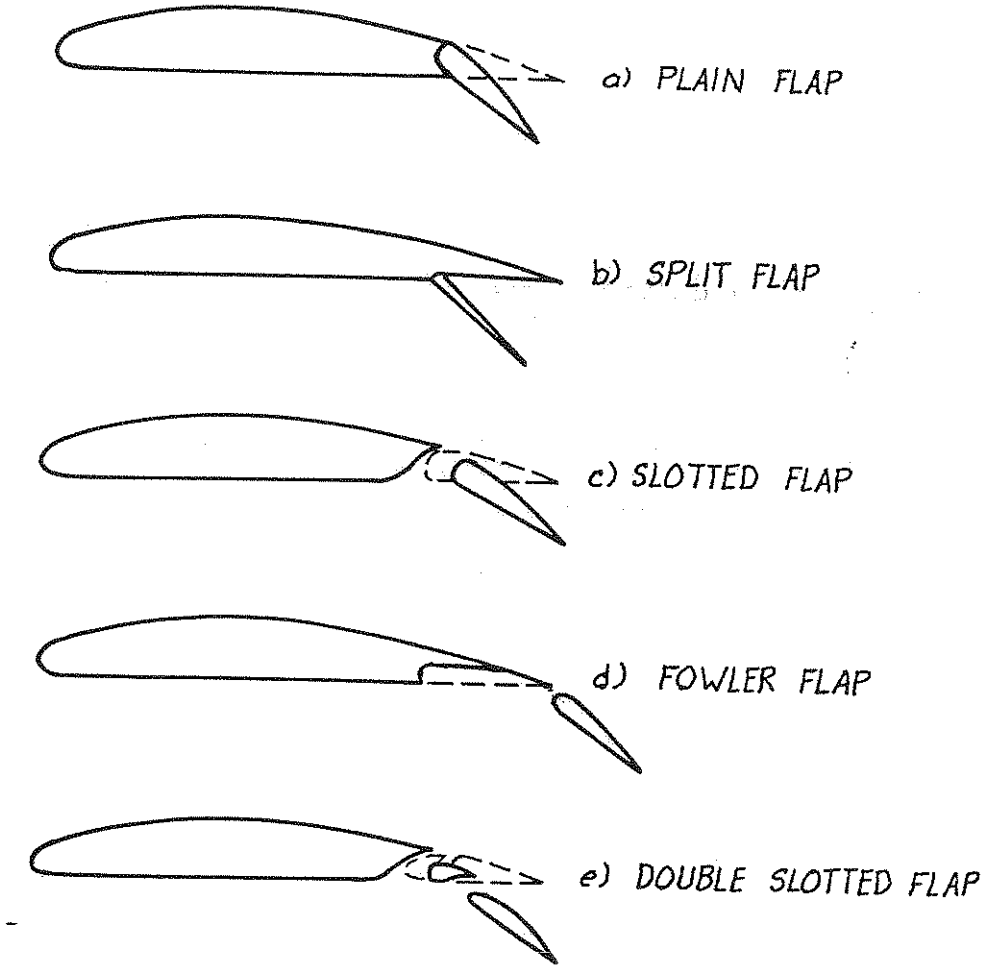

Figure 3.21 Various Configurations of Trailing-Edge Flaps

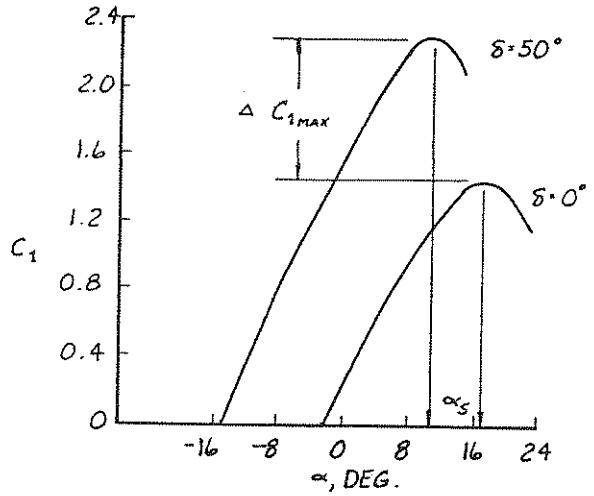

Figure 3.22 Lift Curves for NACA 66(215)-216 Airfoil With 0.20c Sealed Plain Flap

(b) Split Flaps

The usual split flap is formed by deflecting the aft portion of the lower surface about a hinge point on the surface at the forward edge of the deflected portion (Fig. 3.21b). Split flaps derive their effectiveness from the large increase in camber produced. However, since the upper surface is not so highly cambered, separation effects are less marked, so that the performance at high α is improved. The lift-curve slope with split flaps is higher and the stall angle is somewhat lower than that for the plain airfoil, but higher than that for a plain flap. The angle of zero lift is reduced, but not by quite so much as is the case with a plain flap. The increment in $c_{\ell_{max}}$ is larger than with a plain flap, but the drag increment will be higher because of the large wake.

For airfoils of normal thickness ratio, optimum benefit can be obtained by using 20 or 25% flap with deflection angles of 60 or 70 degrees. This is illustrated in Fig. 3.23 (Ref. 3.1).

(c) Slotted Flaps

Slotted flaps provide one or more slots between the main portion of the wing section and the deflected flap: see Fig. 3.21c. The slots duct high-energy air from the lower surface to the upper surface and direct this air in such a manner as to delay flow separation over the flap by providing boundary-layer control. The high lift is again derived mainly from increasing the camber. The increment in $c_{\ell_{max}}$ is much higher than that for a plain or a split flap with less drag because of BLC effect. However, the pitching moment is relatively large and negative.

Common flap chord ratios used with slotted flaps are 0.25 and 0.30.

The aerodynamic characteristics of slotted flaps depend very much on the detailed design of the slot entry and lip. Fig. 3.24 shows some typical results for a single-slotted flap in comparison with split flaps.

(d) Fowler Flaps

The Fowler flap uses the same principle as the slotted flap, except that the flap also moves backwards in addition to a downward deflection: see Fig. 3.21d. Thus, the effective wing area is increased!

The effectiveness of the preceding flaps a) through d) is compared in Fig. 3.25. One important experimental result is that $\Delta c_{\ell_{max}}$ due to flaps may be considered as independent of Reynolds

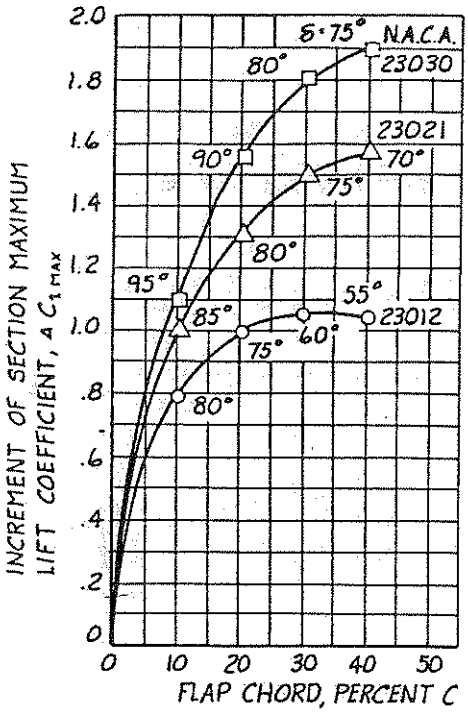

Figure 3.23 Increment of Maximum Lift Coefficient for Three Airfoils with Split Flaps (Ref. 3.1)

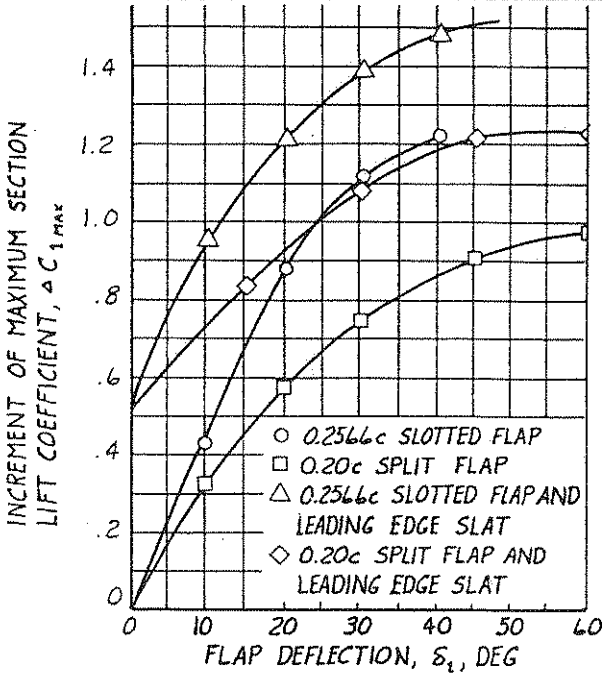

Figure 3.24 Effect of Flaps on Increment of Maximum Lift Coefficient for NACA 23012 Airfoil (Ref. 3.1)

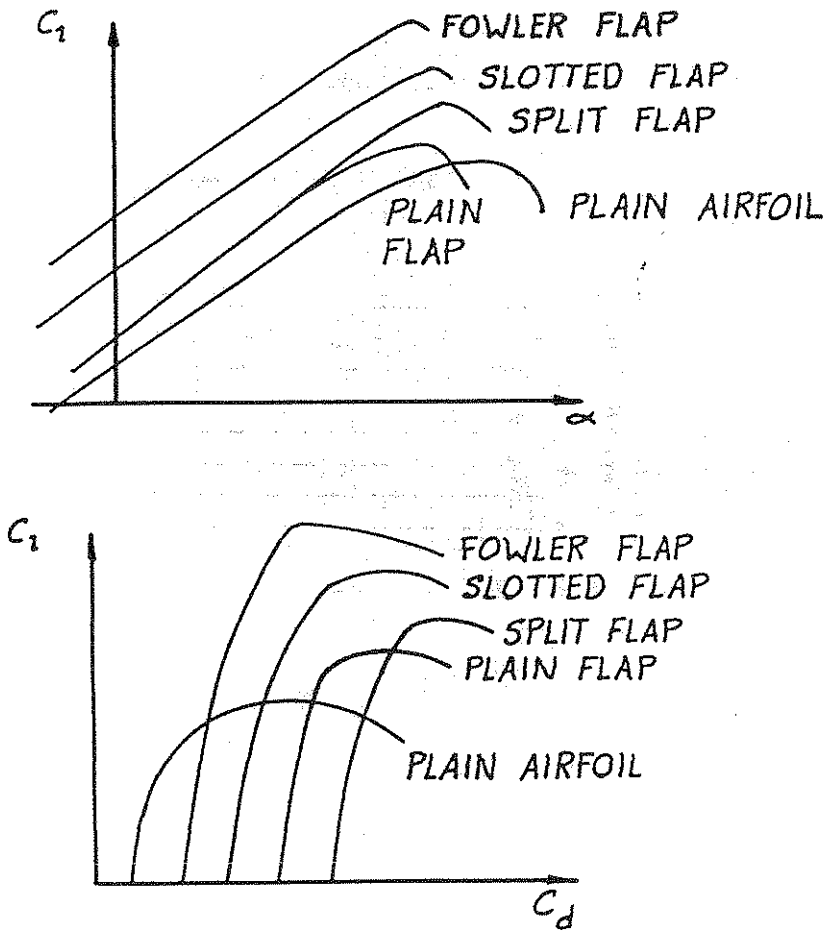

Figure 3.25 Comparison of Effectiveness of Various Flaps

number. Also, the flap does not have a significant effect on dc_m/dc_ℓ and hence the aerodynamic center is not significantly affected.

Table 3.3 lists typical trailing edge flaps used on contemporary airplanes.

Table 3.3 Examples of Leading and Trailing Edge Devices in Use

Airplane	Tailing Edge Flaps	Leading Edge Devices
Cessna 152	Simple Slotted	None
Cessna 414A (Chancellor)	Split	None
Cessna 425 (Titan)	Fowler	None
Boeing 707	Fowler	Krüger Flaps
Boeing 737	Triple Slotted Fowler	Krüger Flaps and Slats
Boeing 747	Triple Slotted Fowler	Variable Camber Flaps and 3-section Krüger flaps
Beech Duke	Single Slotted	None
Beech King Air	Single Slotted	None
Grumman E-2 Hawkeye	Fowler and Drooped Ailerons	None
Grumman Gulfstream II	Single Slotted Fowler	Slats

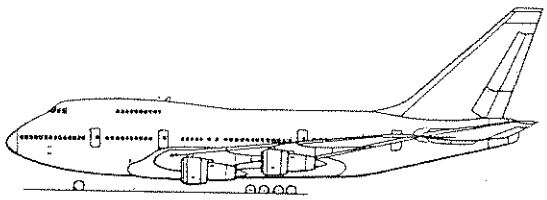

3.8.3.2 Leading-Edge Devices

Various leading-edge devices are shown in Fig. 3.26.

(a) and (b) Slats

Leading-edge slats (see Figs. 3.26a and b) are airfoils mounted ahead of the leading edge of the wing such as to assist in turning the air around the leading edge at high α and thus delay leading-edge stalling. They may be either fixed in position or retractable. The use of slats may increase $c_{\ell_{max}}$ by as much as 0.5. The effect can also be seen in Fig. 3.24.

(c) Slots

When the slot (see Fig. 3.26c) is located near the leading edge, the configuration differs only in detail from the leading-edge slat. Additional slots may be introduced at varous chordwise stations. The effectiveness of the slot derives from its BLC (=Boundary Layer Control) effect. At low α, the minimum profile drag may be greatly increased with such slots.

(d) through (g) Leading-Edge Flaps

A leading-edge flap may be formed by bending down the forward portion of the wing section to form a droop: see Fig. 3.26d. Other types of leading-edge flaps are formed by extending a surface downward and forward from the vicinity of the leading edge (Krüger flap): see Figs. 3.26e through g. Although they are not as powerful as trailing-edge flaps, they are mechanically simpler and they are effective when combined with trailing-edge high lift devices. Leading-edge flaps reduce the severity of the pressure peak ordinarily associated with high α and thereby delay separation.

Some test results for NACA 64_1-012 airfoil with leading- and trailing-edge split flaps are presented in Fig. 3.27. The flap angle indicated in the figure is measured clockwise from the airfoil lower surface. It is seen that the upper surface leading-edge flaps appear to be more effective in increasing $c_{\ell_{max}}$.

3.8.3.3 Boundary Layer Control

Higher maximum lift coefficients can also be achieved by boundary layer control (BLC). This idea may involve injecting high-speed gas parallel to the wall (called "blowing"), or removing the low-

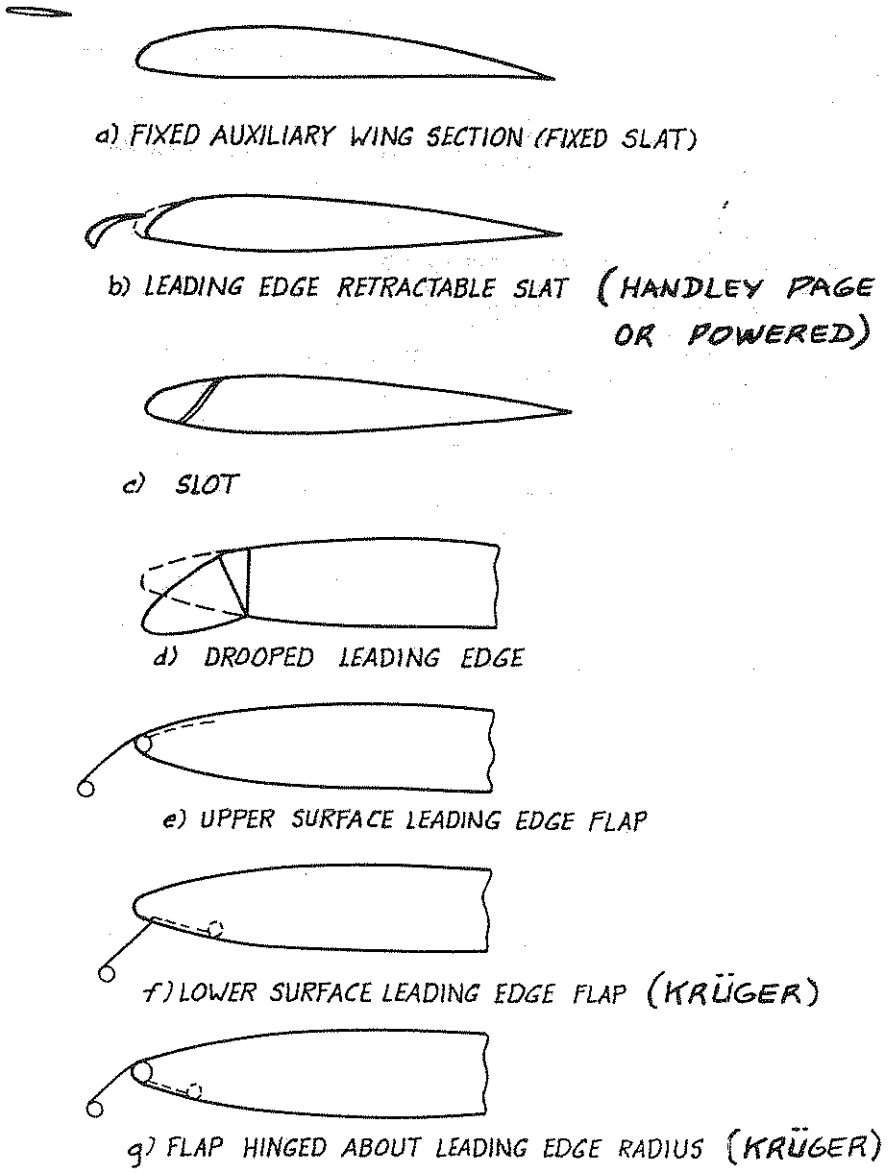

Figure 3.26 Various Configurations of Leading-Edge Devices

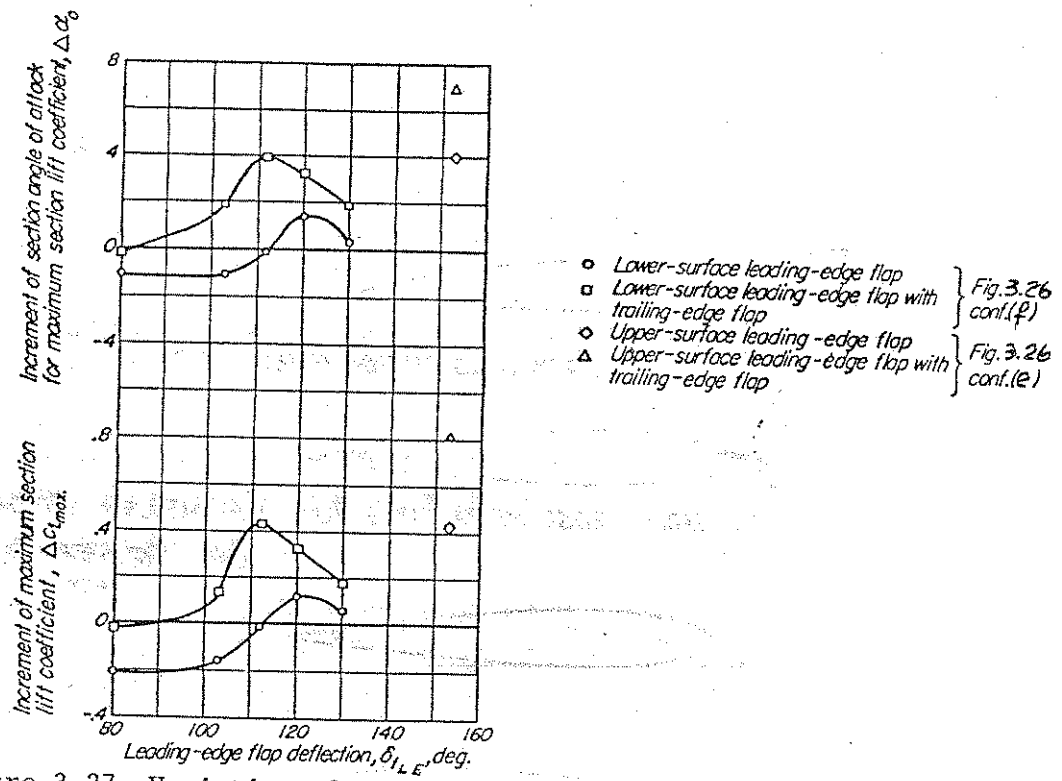

Figure 3.27 Variation of $\Delta C_{l_{max}}$ and $\Delta\alpha_s$ for NACA 64_1-012 Airfoil with Leading-Edge Flap Deflection (NACA TN 1277)

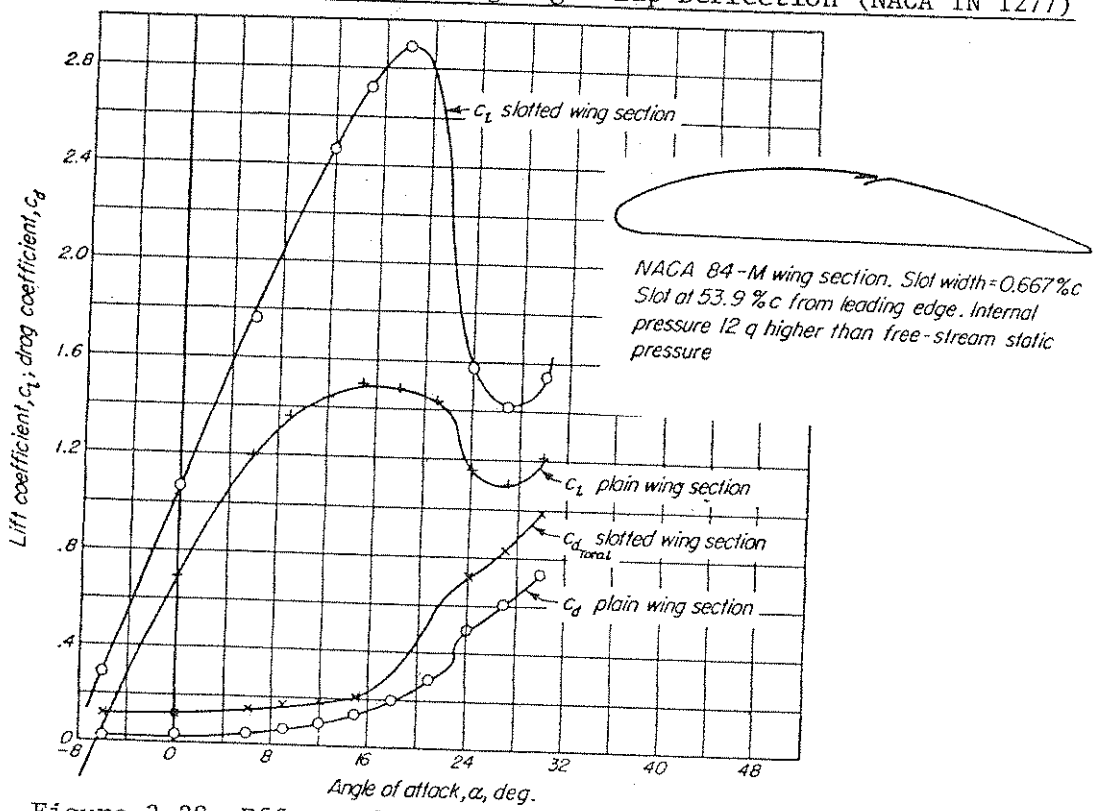

Figure 3.28 Effect of Blowing on Aerodynamic Characteristics. Slot at 53.9%c from Leading Edge (NACA TN 323)

energy boundary layer flow by "suction," or both. Blowing is done to re-energize the boundary layer flow to delay the separation, while suction is equivalent to eliminating the low-energy shear layer. Fig. 3.28 shows that with the slot internal pressure 12 $\bar{q}$ higher than the free-stream static pressure and slot width of 0.667%c, $c_{\ell_{max}}$ can be increased from 1.5 without blowing to 2.9 with blowing.

Suction effect can be provided by using a suitable suction pump to suck the shear layer through porous airfoil skin. This was successfully applied to an F-86F airplane in 1953. This type of boundary layer control can not only increase the lift, but also delay transition to reduce the skin friction drag. This is one concept used in the so-called laminar flow control. On the other hand, some suction can also be achieved by ejector blowing, as shown in Fig. 3.29. This principle has been used in the design of the NASA Augmentor Wing STOL airplane.

It should be noted that when the blowing slot is at the flap hinge and the blowing air momentum is high, the device is frequently referred to as the blown flap. In this case, not only can the flow separation over the flap surface be delayed, but also the circulation, and hence the lift, can be increased. For more detail on the effect of blowing the reader should consult Refs. 3.13 and 3.14.

3.9 SUMMARY

In this chapter several important airfoil characteristics were described and experimental evidence shown.

Based on the currently existing computational state-of-the-art of airfoil design (Refs. 3.15 and 3.18) it seems reasonable to state that for any new airplane design specific airfoils should be tailored.

To achieve the desired balance between conflicting requirements for stability and control on the one hand and performance (such as fuel efficiency) on the other hand it is mandatory to derive specific airfoils to meet specific design objectives.

An indication of the excellent agreement between computational theory and experimental data which is now quite common is given in Fig. 3.30.

The reader might ask the question whether or not it is possible to control camber in flight in a continual manner. This thought is behind the so-called NASA mission adaptive wing concept, being tested on an F-111 fighter (Ref. 3.19).

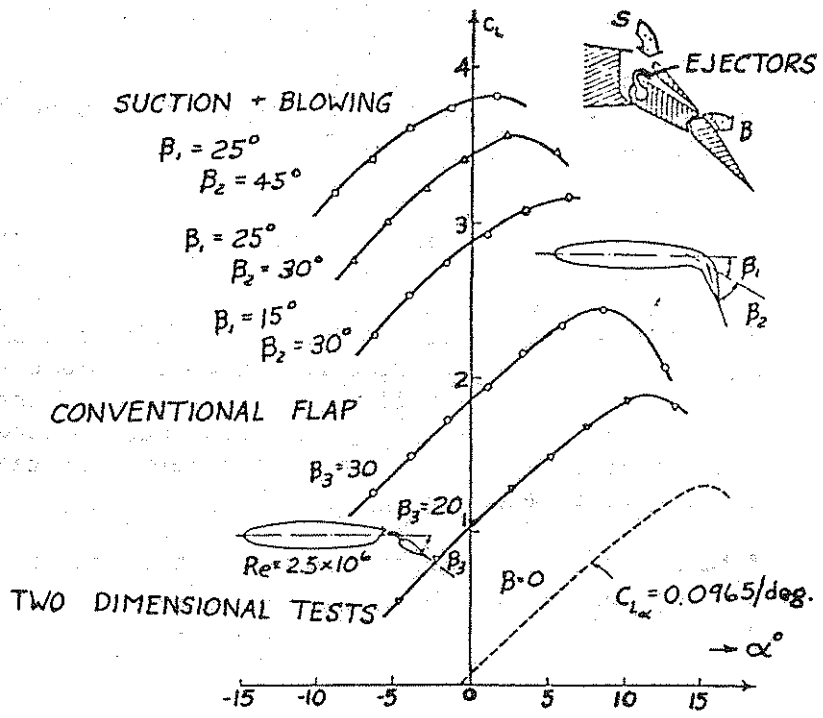

Figure 3.29 Comparison of Lift Curves for a Double Flap with Suction and Blowing, and a Typical Slotted Flap (Ref. 3.12)

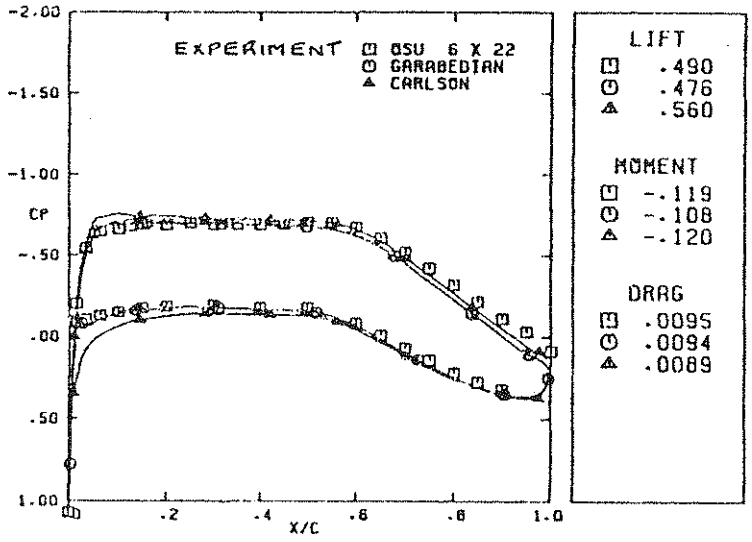

M = 0.578; RE = 4.98 million; $\alpha = -0.07°$.

Figure 3.30 Correlation Between Theory and Experiment of a Modern Low Speed Airfoil

Problems for Chapter 3

3.1 An airfoil of thickness ratio of 17% has the following geometrical and aerodynamic characteristics:

x/c	(z/c)upper	(z/c)lower	C_p(upper) at $M_\infty = 0.0$
0.0	0.	0.	
0.005	0.02035	-0.01444	-0.35
0.0125	0.03069	-0.02052	-0.13
0.025	0.04165	-0.02691	-0.48
0.05	0.05600	-0.03569	-0.70
0.075	0.06561	-0.04209	-0.76
0.100	0.07309	-0.04700	-0.77
0.150	0.08413	-0.05426	-0.75
0.20	0.09209	-0.05926	-0.75
0.25	0.09778	-0.06265	-0.73
0.30	0.10169	-0.06448	-0.73
0.35	0.10409	-0.06517	-0.73
0.40	0.10500	-0.06483	-0.725
0.45	0.10456	-0.06344	-0.723
0.50	0.10269	-0.06091	-0.72
0.55	0.09917	-0.05683	-0.71
0.60	0.09374	-0.05061	-0.66
0.65	0.08604	-0.04265	-0.588
0.70	0.07639	-0.03383	-0.50
0.75	0.06517	-0.02461	-0.35
0.80	0.05291	-0.01587	-0.26
0.85	0.03983	-0.00852	-0.16
0.90	0.02639	-0.00352	-0.05
0.95	0.01287	-0.00257	-0.05
1.00	-0.00074	-0.00783	0.10

Derive an airfoil with thickness ratio equal to 13% and having the same camber.

3.2 For the airfoil of Prob. 3.1, calculate and plot the pressure distribution at $M_\infty = 0.60$ and $M_\infty = 0.0$ through the Prandtl-Glauert transformation.

3.3 For the airfoil of Prob. 3.1, find the critical Mach number.

3.4 An airfoil has a lift-curve slope of 6.3 per radian and angle of zero lift of -2°. At what angle of attack will the airfoil develop a lift of 140 lb/ft at 100 mph under standard sea-level conditions? Assume c = 8 ft.

3.5 The test results of a NACA 23012 airfoil model at $R_N = 3 \times 10^6$ show the following:

$\alpha°$	c_ℓ	
0	0.15	$c_{d_{min}} = 0.0065$
9	1.2	

Determine the lift curve slope per degree and per radian.

3.6 For the airfoil of Prob. 3.5, determine $c_{d_{min}}$ if $R_N = 20 \times 10^6$.

3.7 For the airfoil of Prob. 3.1, determine the pressure coefficient at x/c = 0.10 when the airspeed is 450 mph under standard sea-level conditions. Use the Prandtl-Glauert and Kármán-Tsien formulas.

3.8 The pressure at a point on an airplane flying at 250 mph at sea level is 8 psi absolute. Find the pressure coefficient at this point.

3.9 Prove that Eqn. (3.9) is correct.

References for Chapter 3

3.1 Abbott, I. A. and von Doenhoff, A. E., "Theory of Wing Sections," Dover 1959.

3.2 Vernard, J. K., Elementary Fluid Mechanics, J. Wiley and Sons, 1957.

3.3 Buckingham, E., "Model Experiments and the Focus of Empirical Equations," Trans. ASME, vol. 37, p. 263, 1915.

3.4 Braslow, A. and Knox, E., "Simplified Method for Determination of Critical Height of Distributed Roughness Particles for Boundary-Layer Transition at Mach Numbers from 0.0 to 5.0," NACA TN 4363, September, 1958.

3.5 Braslow, A. L., Hicks, R. M. and Harris, R. V., Jr., "Use of Grit-Type Boundary-Layer-Transition Trips on Wind-Tunnel Models," NASA TN D-3579, September, 1966.

3.6 Hoerner, S. F., "Fluid-Dynamic Drag," published by he author, 1965.

3.7 Jacobs, E. N. and Sherman, A., "Airfoil Section Characteristics as Affected by Variations of the Reynolds Number," NACA Report 586, 1937.

3.8 Hoerner, S. F. and Borst, H. V., "Fluid-Dynamic Lift," published by L. A. Hoerner, 1975.

3.9 McGhee, R. J. and Beasley, W. D., "Low-Speed Aerodynamic Characteristics of a 17-Percent-Thick Airfoil Section Designed for General Aviation Applications," NASA TN D-7428, December, 1973.

3.10 McGhee, R. J., Beasley, W. D. and Somers, D. M., "Low-Speed Aerodynamic Characteristics of a 13-Percent-Thick Airfoil Section Designed for General Aviation Applications," NASA TMX-72697, May, 1975.

3.11 Nonweiler, T., "Maximum Lift Data for Symmetrical Wings," Aircraft Engineering, vol. 27, no. 311, January 1955, p. 3-8.

3.12 Ph. Poisson Quinton and Lepage, L., "Survey of French Research on the Control of Boundary Layer and Circulation," in "Boundary Layer and Flow Control," edited by G. V. Lachmann, vol. 1, Pergamon Press, 1961.

3.13 Kohlman, D.L., "Introduction to STOL Airplanes," Department of Aerospace Engineering, The University of Kansas, Lawrence, Kansas, 66045, 1979.

3.14 McCormick, Jr., Barnes, W., "Aerodynamics of V/STOL Flight," Academic Press, 1967.

3.15 Bauer, F., Garabedian, P. and Korn, D., "A Theory of Supercritical Wing Sections, with Computer Programs and Examples," Lecture Notes in Economics and Mathematical Systems, Vol. 66, 1972, Springer Verlag.

3.16 Freuler, R.J., and Gregorek, G.M., "An Evaluation of Four Single Element Airfoil Analytic Methods," Proceedings of Advanced Technology Airfoil Research Conference, NASA Publication 2045, March, 1978.

3.17 Stevens, W.A., Goradia, S.H. and Braden, J.A., "Mathematical Model for Two-Dimensional Multi-Component Airfoils in Viscous Flows, NASA CR-1843, July, 1971.

3.18 Bauer, F., Garabedian, P., Korn, D., and Jameson, A., "Supercritical Wing Sections II, A Handbook," Lecture Notes in Economics and Mathematical Systems, Vol. 108, Springer Verlag, New York, 1975.

3.19 DeCamp, R. W. and Hardy, R., "Mission Adaptive Wing Research Programme," Aircraft Engineering, January 1981, pp. 10-11.

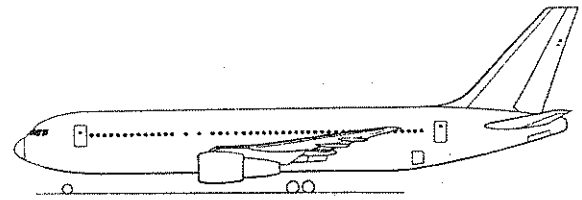

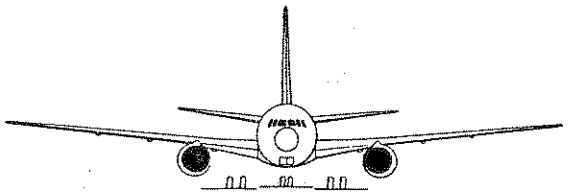

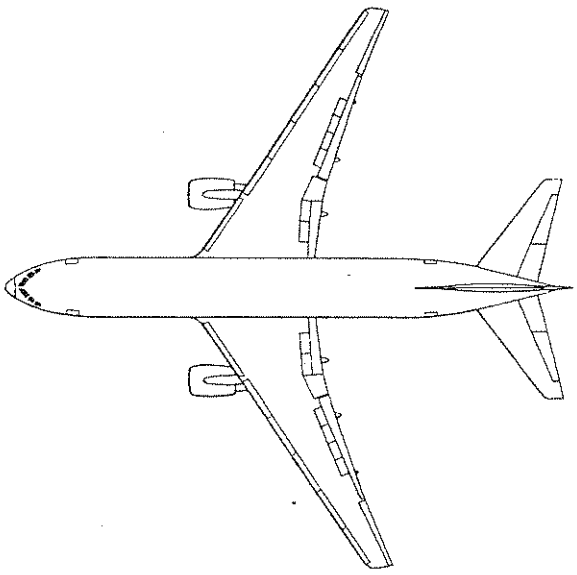

4. WING THEORY

The purpose of this chapter is to familiarize the reader with a number of key aspects of wing (or planform) theory and applications thereof.

After a definition of basic planform geometric parameters in Section 4.1, a discussion of circulation, downwash, lift and induced drag is presented in Section 4.2.

From a design viewpoint, span efficiency, aerodynamic center location, stall behavior, high speed characteristics and flaps are of utmost importance. Section 4.3 through 4.7 present introductions to these subject areas.

It should be evident to the reader that the following discussions of wing theory apply to any lifting surface. They are therefore also applicable to tails, canards and other types of surfaces which may be used on airplanes.

4.1 DEFINITION OF WING PROPERTIES

Fig. 4.1 shows a typical wing planform. Geometric wingspan, b, is the distance between tip to tip of the wing, measured perpendicular to the airplane or wing centerline, regardless of the geometric shape of the wing. The area of a wing, S, is the projection of the planform on a plane of reference which is usually the chord plane. The wing is considered to extend without interruption through the fuselage and/or nacelles. The wing aspect ratio is defined as:

$$A \text{ (or AR)} = \frac{b^2}{S} \tag{4.1}$$

The taper ratio, λ, is defined as the ratio of the tip chord c_t to the root chord c_r. Thus:

$$\lambda = \frac{c_t}{c_r} \tag{4.2}$$

The mean aerodynamic chord (MAC)* is frequently used to define the pitching moment coefficient (see Eqn. 4.7). It is here defined as:

$$\text{MAC} = \bar{c} = \frac{2}{S} \int_0^{b/2} c^2 dy \tag{4.3}$$

*Strictly speaking, this chord should be called mean geometric chord (m.g.c.).

95

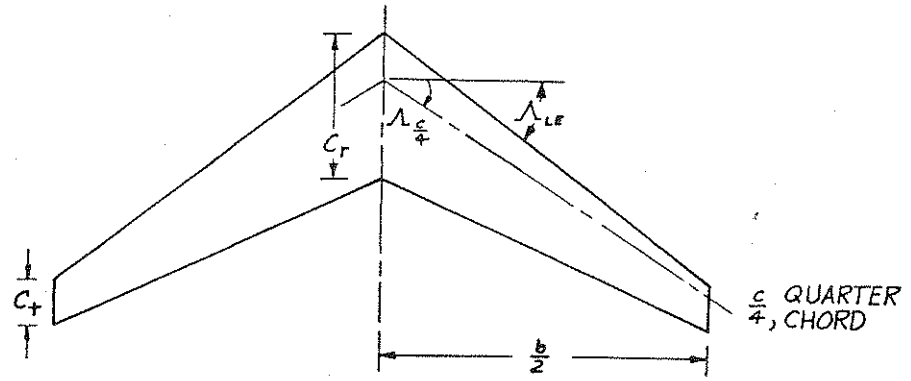

Figure 4.1 Example of a Wing Planform

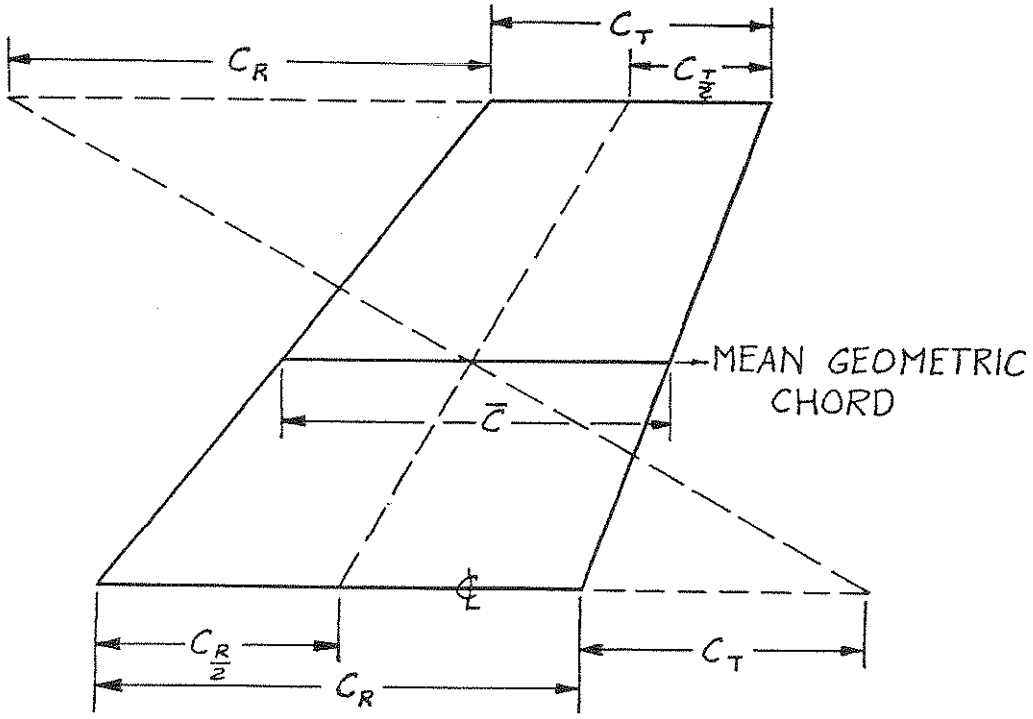

Figure 4.2 Example of MAC Construction

For straight tapered wings, Eqn. 4.3 can be evaluated to give:

$$\bar{c} = \frac{2}{3} c_r \left(\frac{\lambda^2 + \lambda + 1}{\lambda + 1}\right) \tag{4.4}$$

A simple construction to find the $\bar{c}$ on an arbitrary straight tapered planform is illustrated in Fig. 4.2.

The sweep angle, Λ, is the angle between a line perpendicular to the centerline and the leading edge or the quarter chord line. It is denoted as Λ_{LE} or $\Lambda_{c/4}$.

Following the expressions of force and moment equations for airfoils (Eqn. 3.15 through 3.17) the wing aerodynamic forces and moment are written as:

$$L = C_L \bar{q} S \tag{4.5}$$

$$D = C_D \bar{q} S \tag{4.6}$$

$$M = C_m \bar{q} S \bar{c} \tag{4.7}$$

4.2 CIRCULATION, DOWNWASH, LIFT AND INDUCED DRAG

Circulation about a wing is produced by the difference in pressure between the upper and lower surfaces of a wing, which induces a flow from the lower surface toward the upper surface around the leading edge and tips. The strength of this flow is measured in terms of circulation. This effect can be represented by means of a bound vortex distribution on the wing and its associated trailing vortices. Fig. 4.3 illustrates these ideas. The net effect of the trailing vortices is to produce a downwash velocity distribution, w on the wing. From Fig. 4.4, it follows that:

$$\tan\alpha_i \simeq \alpha_i = \frac{w}{V} \tag{4.8}$$

The total force on the wing is given by:

$$F = \int_{-b/2}^{b/2} \rho V \Gamma dy \tag{4.9}$$

according to Eqn. (2.78). Since α_i is small, $F \simeq L$ and therefore:

$$D_i = L \tan\alpha_i \simeq L \frac{w}{V} \approx L\alpha_i \tag{4.10}$$

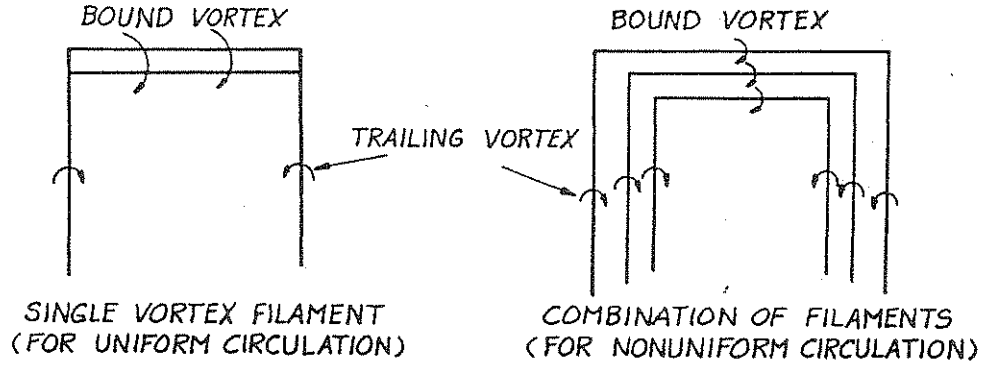

Figure 4.3 Geometry of Circulation and Vortices

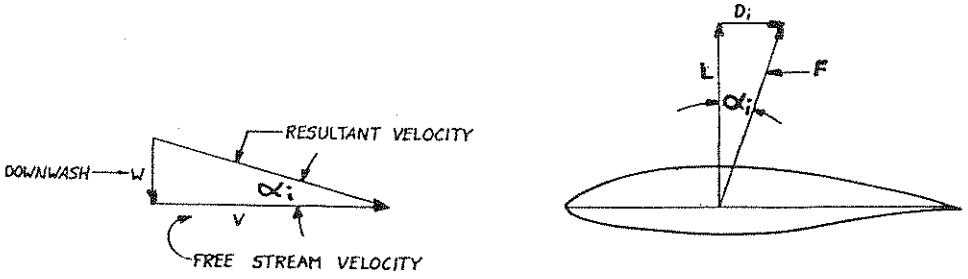

Figure 4.4 Relation Between Downwash, Lift and Induced Drag

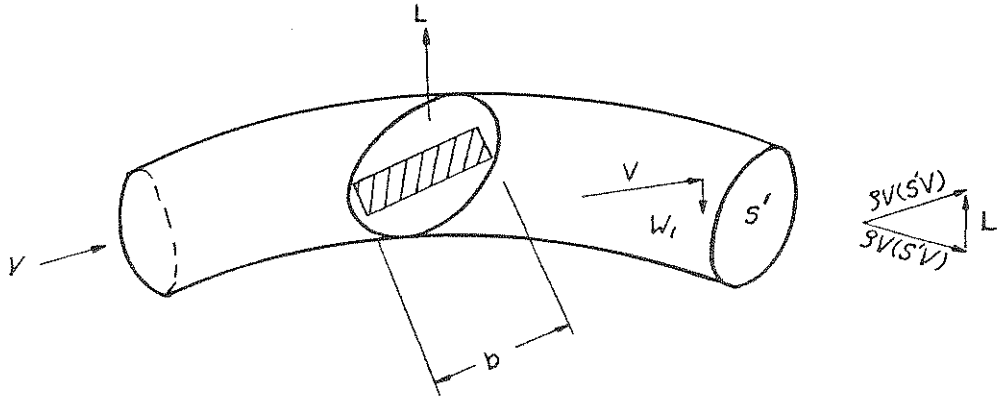

Figure 4.5 Relationship Between Wing and Streamtube

Let w_1 be the downwash far behind the wing. Consider a stream tube of cross-sectional area S' behind the wing. Fig. 4.5 illustrates the wing and the streamtube. Two methods for calculating lift will now be considered:

- Momentum Method
- Energy Method

Momentum Method

According to the linear momentum principle, assuming uniform downwash over S',

$$L = \rho V(S'V)\frac{w_1}{V} = \rho w_1(S'V) \tag{4.11}$$

Energy Method

The work done on the air mass per unit time equals the kinetic energy increase per unit time. Therefore:

$$D_i V = \rho S' V \frac{w_1^2}{2} \tag{4.12}$$

or:

$$D_i = \rho S' \frac{w_1^2}{2} \tag{4.13}$$

Recalling Eqn. (4.10):

$$L = \frac{D_i}{\alpha_i} = \frac{\rho S' \frac{w_1^2}{2}}{w/V} = \rho S' \frac{Vw_1^2}{2w} \tag{4.14}$$

And from this:

$$\rho w_1(S'V) = \rho S' \frac{Vw_1^2}{2w} \tag{4.15}$$

or:

$$2w = w_1 \tag{4.16}$$

Thus, the induced downwash far behind the wing is twice that on the wing. With S' taken to be $\frac{\pi b^2}{4}$, it follows from (4.14) that:

$$L = \rho(2w)\frac{\pi b^2}{4} V \tag{4.17}$$

Solving for w:

$$w = \frac{2L}{\rho\pi b^2 V} = \frac{C_L \bar{q} SV}{\pi b^2 \bar{q}} = \frac{C_L SV}{\pi b^2} = \frac{C_L V}{\pi A} \tag{4.18}$$

Therefore, the angle α_i is now found from:

$$\alpha_i = \frac{w}{V} = \frac{C_L}{\pi A} \tag{4.19}$$

Similarly, from Eqn. (4.10):

$$D_i = L\alpha_i = C_L \bar{q} S \frac{C_L}{\pi A} \tag{4.20}$$

And therefore it follows for the induced drag coefficient that:

$$C_{D_i} = \frac{D_i}{\bar{q}S} = \frac{C_L^2}{\pi A} \tag{4.21}$$

The above equations are valid for wings with elliptical loading (i.e., uniform downwash distribution). The induced drag coefficient for this case has been shown to be minimum. This condition can be achieved by using an elliptical planform (Ref. 4.1, p. 142). When the downwash distribution is not uniform, a factor 'e' is introduced as follows:

$$C_{D_i} = \frac{C_L^2}{\pi e A} \tag{4.22}$$

Therefore the induced angle is:

$$\alpha_i = \frac{C_L}{\pi e A} \tag{4.23}$$

where e = span efficiency factor*. Experimentally it is found that e = 0.85 ~ 0.95 for the wing alone.

The factor eA is often referred to as the effective aspect ratio, A_{eff}. The total drag coefficient for a wing can therefore be written as:

*The factor, e, is also known as Oswald's efficiency factor.

$$C_D = C_{D_o} + \frac{C_L^2}{\pi e A} = C_{D_o} + \frac{C_L^2}{\pi A_{eff}} \tag{4.24}$$

where C_{D_o} is the (lift independent) sum of skin friction and pressure drag.

Assume that two wings have high but different aspect ratios. Also assume that they have the same airfoil. In that case, according to Prandtl's Lifting Line Theory (Ref. 4.1, p.137) if these wings are placed at the same effective angle of attack $\alpha_a - \alpha_i$, their lift coefficient C_L must be the same where $\alpha_a = \alpha - \alpha_o$ is the absolute angle of attack and α_o is the angle of zero lift. Therefore:

$$\alpha_{a_1} - \frac{C_L}{\pi (e\ A)_1} = \alpha_{a_2} - \frac{C_L}{\pi (e\ A)_2} \tag{4.25}$$

or:

$$\alpha_{a_1} = \alpha_{a_2} + \frac{C_L}{\pi} \left[\frac{1}{(e\ A)_1} - \frac{1}{(e\ A)_2}\right] \tag{4.26}$$

Since:

$$C_L = a\alpha_a \quad (\alpha_a \text{ in rad.}) \tag{4.27}$$

it follows that :

$$\frac{C_L}{a_1} = \frac{C_L}{a_2} + \frac{C_L}{\pi} \left[\frac{1}{(e\ A)_1} - \frac{1}{(e\ A)_2}\right] \tag{4.28}$$

or:

$$a_1 = \frac{a_2}{1 + \frac{a_2}{\pi} \left[\frac{1}{(e\ A)_1} - \frac{1}{(e\ A)_2}\right]} \tag{4.29}$$

This equation allows an estimate of the lift-curve-slope a_1 of a wing with effective aspect ratio $(eA)_1$ if the corresponding but different properties of a second wing are known.

The reader is cautioned to use this Eqn. (4.29) only for aspect ratios above roughly 5.

The effect of aspect ratio on the lift curve of a wing is shown in Fig. 4.6. Wings of various aspect ratios are seen to have about the same angle of zero lift, but the slope of the lift curve increases progressively with an increase of aspect ratio. This effect can be deduced also from Eqn. (4.29).

For the same wing area and the same airfoils, the wing zero lift drag is essentially independent of aspect ratio. Eqn. (4.24) suggests this. Applying Eqn. (4.22) to two wings of different effective aspect ratios yields:

$$C_{D_1} = C_{D_2} + \frac{C_L^2}{\pi}\left[\frac{1}{(eA)_1} - \frac{1}{(eA)_2}\right] \tag{4.30}$$

From the drag curves in Fig. 4.6, it is seen that although the drag coefficients for all wings of various aspect ratios are substantially equal at zero lift, marked reductions in C_D occur at higher C_L as the aspect ratio is increased. If Eqns. (4.26) and (4.30) are used to reduce the data of Fig. 4.6 to an aspect ratio of 5, the results will be as shown in Fig. 4.7. All data points are seen to collapse into one curve, except those for aspect ratios of 1 and 2. It follows that the characteristics of a wing of one aspect ratio may be predicted with considerable accuracy from data obtained from tests of a wing of considerably different aspect ratio.

Eqn. (4.29) is used to determine the lift curve slope of wing 1 if the characteristics of wing 2 with the same airfoil section are known. If wing 2 is of infinite aspect ratio (i.e., two-dimensional airfoil section), Eqn. (4.29) can be reduced to:

$$a_1 = \frac{a_\infty}{1 + \frac{a_\infty}{\pi e A}} \tag{4.31}$$

Note that Eqn. (4.31) is accurate only if $A > 5$ and the sweep angle is small, such as less than 15 degrees. It has been improved by Lowry and Polhamus (Ref. 4.3) for arbitrary aspect-ratio and swept wings as follows:

$$a = \frac{2\pi A}{2 + \sqrt{\frac{A^2\beta^2}{\kappa^2}\left(1 + \frac{\tan^2 \Lambda_{c/2}}{\beta^2}\right) + 4}} \tag{4.32}$$

where,

$$\beta^2 = 1 - M_\infty^2 \tag{4.33}$$

and:

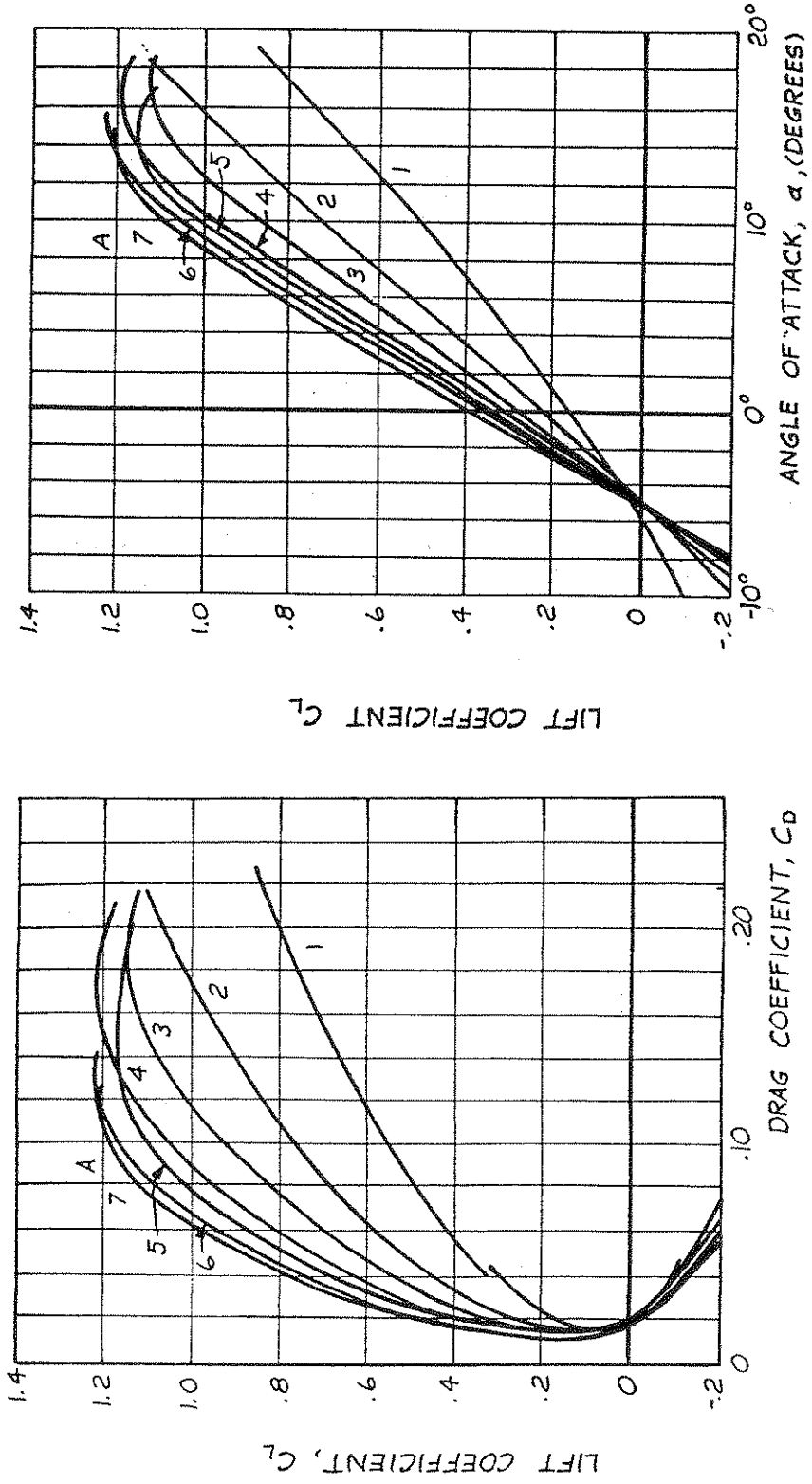

Figure 4.6 Examples of Lift Curve and Drag Behavior of Unswept, Untapered Wings at Low Speed (Data from Ref. 4.2, pp. 4-5)

Figure 4.7 Example of Lift and Drag Curves of a Family of Wings Reduced To Aspect Ratio of 5 (Data from Ref. 4.2, pp. 6-7)

$$\kappa = a_\infty / 2\pi/\beta \qquad (4.34)$$

In Eqn. (4.34), $2\pi/\beta$ is the theoretical sectional lift curve slope obtained by the Prandtl-Glauert transformation (see Eqn. (3.34)). It follows that κ is the ratio of experimental airfoil lift curve slope at subsonic Mach number to the theoretical value. It can be shown that if A is large and is taken as A_{eff}, $\Lambda_{c/2}$ is small, and $a_\infty = 2\pi$, Eqn. (4.32) can be reduced to Eqn. (4.31) for $M_\infty = 0$.

More accurate results can be obtained through the so-called lifting surface theories (see, for example, Refs. 4.4 to 4.6). Lifting-surface theories can calculate not only the lift curve slope of any arbitrary wings, but also the induced drag, pitching moment and load distribution.

4.3 EVALUATION OF THE SPAN EFFICIENCY FACTOR e

To expedite performance calculations and to simplify reduction of flight data, it is convenient to represent the lift-drag curve by the following equation:

$$C_D = C_o + C_1 C_L + C_2 C_L^2 + \ldots \qquad (4.35)$$

For wings of $A \geq 3$ and $\Lambda < 30^o$ and not incorporating airfoils displaying low drag buckets, the following parabolic drag polar equation provides a reasonable curve fit for C_L values from zero to one:

$$C_D = C_{D_o} + \frac{C_L^2}{\pi e A} \qquad (4.36)$$

In Eqn. (4.36) the so-called Oswald-efficiency factor 'e' can be increased by the use of tip tanks, winglets and proper wing-fuselage blending. The basic form of Eqn. (4.36) has been shown to be valid at supersonic and subsonic Mach numbers. However, at high Mach numbers, e has been shown to be Mach number-dependent. This is illustrated in Fig. 4.8 and Fig. 4.9 for wing-body combinations and for a supersonic fighter for:

$$\frac{dC_D}{dC_L^2} = \frac{1}{\pi e A} \qquad (4.37)$$

At supersonic speeds, C_{D_o} will increase with M because of the addition of wave drag: this is also illustrated in Fig. 4.9.

If Eqn. (4.36) is plotted as C_D versus C_L^2, the results should be a straight line with the slope being $1/\pi eA$. This has been shown

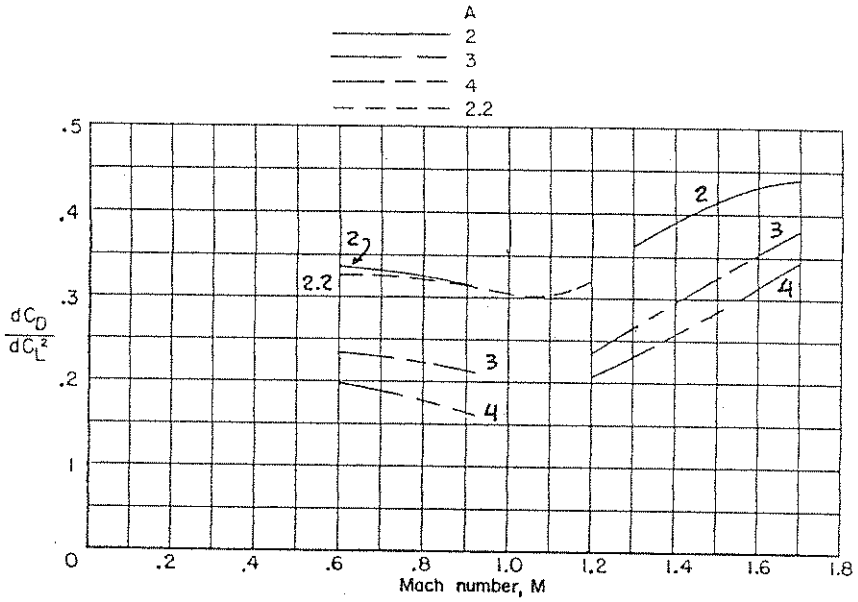

Figure 4.8 Variation of Drag-Due-to-Lift Factor $\frac{dC_D}{dC_L^2}$ with Mach Number for Wing-Body Combination Having Delta Wings with Aspect Ratios From 2 to 4. $R_c \approx 5 \times 10^6$; $t/c \approx 0.03$; $\frac{dC_D}{dC_L^2}$ averaged to $C_L = 0.3$ (Taken from Ref. 4.7)

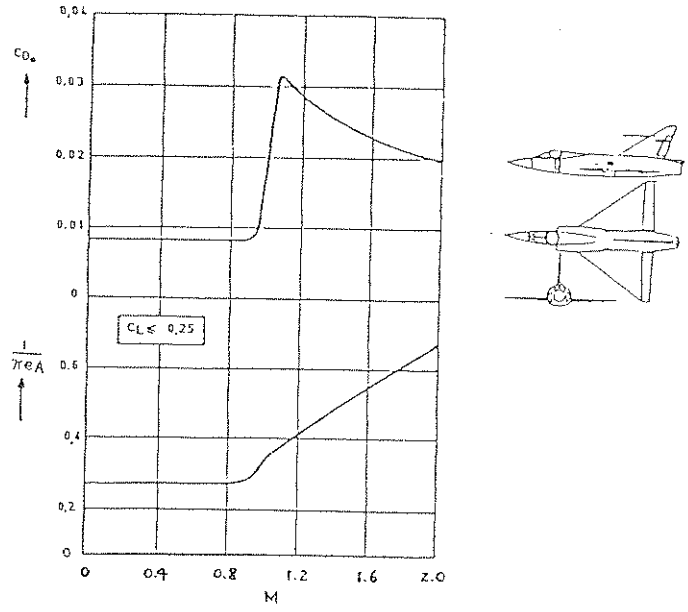

Figure 4.9 Example of Variation of C_D, and e with Mach Number for a Supersonic Fighter Airplane

to be true only if $R_N > 5 \times 10^6$. Fig. 4.10 indicates this situation with test data. Table 4.1 shows that actual flight Reynolds Numbers are usually much higher than 5×10^6.

4.4 AERODYNAMIC CENTER

The aerodynamic center (A.C.) of a wing is defined in the same way as that of an airfoil section. (See Chapter 3.) It is defined as a point about which the pitching moment is independent of α. This should be compared with the center of pressure (C.P.) about which the pitching moment is zero. Thus, the location of C.P. varies with α.

To determine the A.C. from experimental data, assume that the moment center for the data is at a distance x from the leading edge. Taking moments about the A.C., (See Fig. 4.11) it follows that:

$$C_{m_{ac}} \bar{q}\bar{c}S = C_{m_x} \bar{q}\bar{c}S + C_L \bar{q}S(x_{ac} - x)\cos\alpha + C_D \bar{q}S(x_{ac} - x)\sin\alpha \quad (4.38)$$

Solving for x_{ac}, it is obtained that:

$$\frac{x_{ac}}{\bar{c}} = \frac{x}{\bar{c}} - \frac{C_{m_x} - C_{m_{ac}}}{C_L\cos\alpha + C_D\sin\alpha} \quad (4.39)$$

If α is small, Eqn.(4.39) can be simplified:

$$\frac{x_{ac}}{\bar{c}} \cong \frac{x}{\bar{c}} - \frac{C_{m_x} - C_{m_{ac}}}{C_L} \quad (4.40)$$

If $C_{m_{ac}}$ is known (from experimental data or from pressure distribution calculations) the A.C. location can be computed. At zero lift, the forces on the wing appear as a pure moment. Since a pure moment may be transferred to any location without changing its magnitude and since $C_{m_{ac}}$ is independent of α, the zero-lift moment, $\bar{C}_{m_o}$ must be equal to $C_{m_{ac}}$:

$$\bar{C}_{m_o} = C_{m_{ac}} \quad (4.41)$$

Fig. 4.12 presents some experimental data indicating typical A.C. locations for several wings. Empirical methods for determining these quantities may be found in Refs. 4.9 and 4.10.

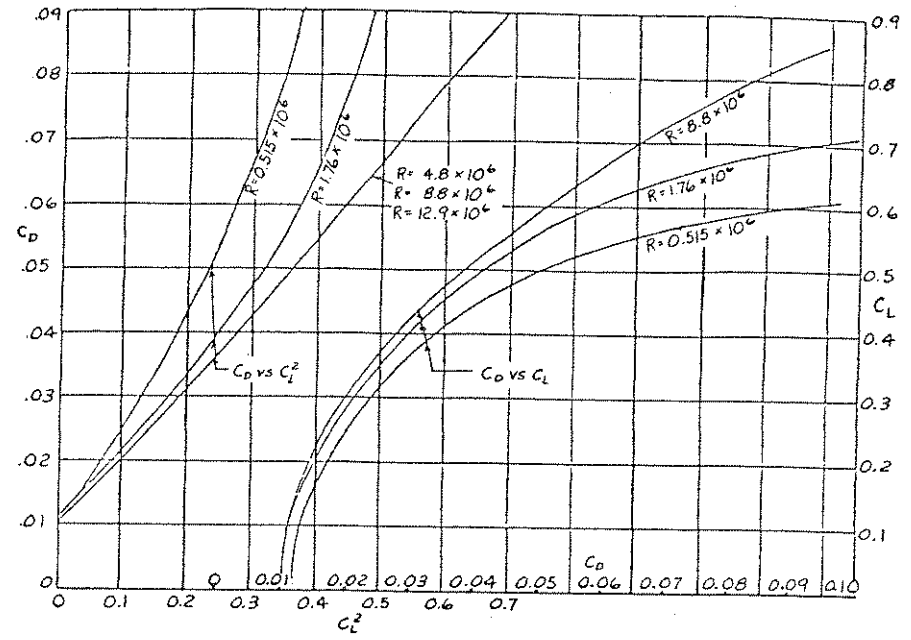

Figure 4.10 Example of Dependence of $\frac{dC_D}{dC_L^2}$ on Reynolds Number (Ref. 4.8)

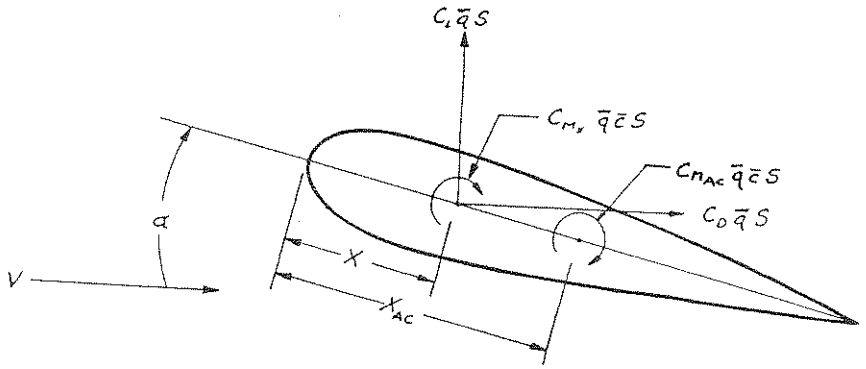

Figure 4.11 Geometry Used with Eqns. (4.38-4.40)

Table 4.1 Example of Typical Flight Reynolds Numbers of Airplanes

Airplane	Flight Condition	Reynolds' Number			
		All Dimensions in Feet			
		Wing	H.T.	V.T.	Fuse
Cessna Stationair 7		$\bar{c}_w = 5.2$	$\bar{c}_H = 3.7$	$\bar{c}_V = 3.3$	$\ell_{FUS} = 28.3$
	Max. Cruise Speed at 10,000 ft. $V_{CR} = 170$ mph	6.4×10^6	4.6×10^6	4.1×10^6	34.8×10^6
	Stall Speed (flaps down) at Sealevel $V_s = 67$ mph	3.2×10^6	2.3×10^6	2.1×10^6	17.4×10^6
Learjet M 36		$\bar{c}_w = 7$	$\bar{c}_H = 4.1$	$\bar{c}_V = 7.9$	$\ell_{FUS} = 45.9$
	Max. Cruise Speed at 35,000 ft. $V_{CR} = 534$ mph	13.5×10^6	7.9×10^6	15.2×10^6	88.5×10^6
	Stall Speed (flaps down) at Sealevel $V_s = 106$ mph	6.9×10^6	4.0×10^6	7.8×10^6	45.2×10^6
Boeing 727 - 200		$\bar{c}_w = 16.8$	$\bar{c}_H = 12.8$	$\bar{c}_V = 22.2$	$\ell_{FUS} = 130.4$
	Max. Cruise Speed at 25,000 ft. $V_{CR} = 599$ mph	49.0×10^6	57.3×10^6	54.7×10^6	380.0×10^6
	Stall Speed (flaps down) at Sealevel $V_s = 122$ mph	19.1×10^6	14.6×10^6	25.2×10^6	148.0×10^6
Boeing 747 - 200B		$\bar{c}_w = 30.8$	$\bar{c}_H = 84.8$	$\bar{c}_V = 26.6$	$\ell_{FUS} = 22.5$
	Max. Cruise Speed at 30,000 ft. $V_{CR} = 608$ mph	77.8×10^6	62.1×10^6	68.3×10^6	578.0×10^6
	Stall Speed (flaps down) at Sealevel $V_s = 116$ mph	32.8×10^6	26.2×10^6	28.8×10^6	244.0×10^6

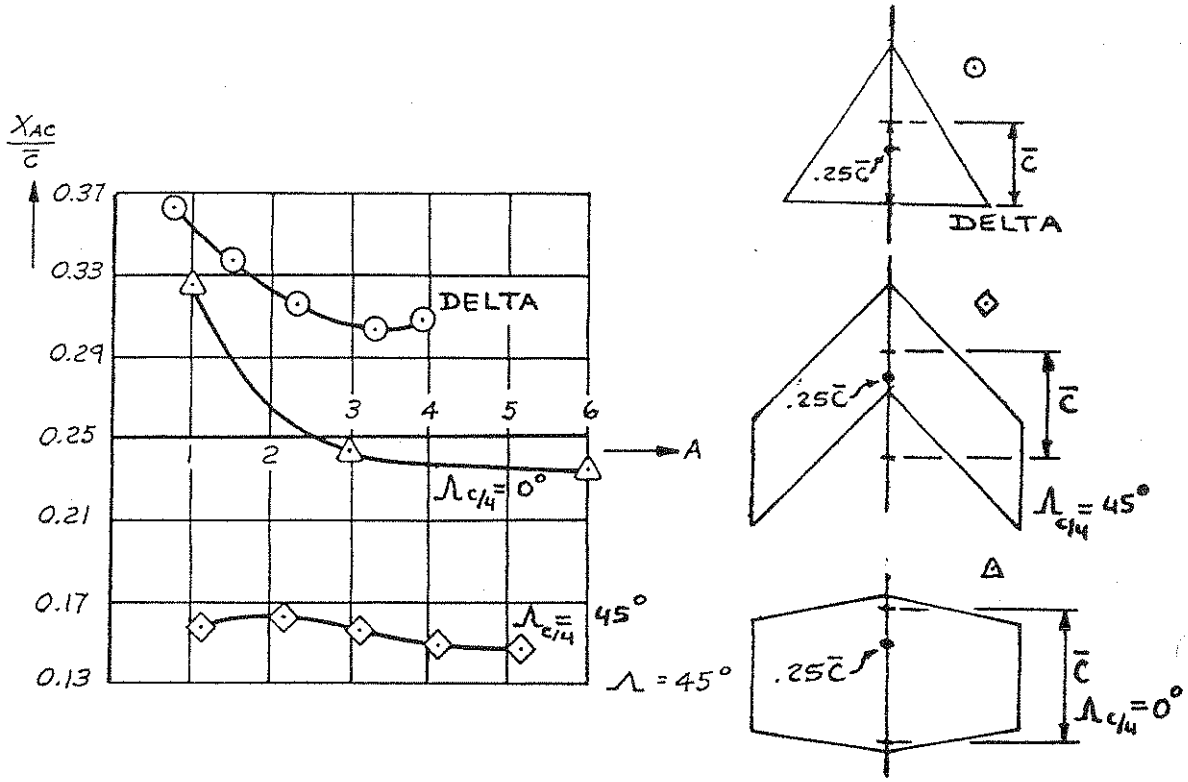

Figure 4.12 Examples of Variation of Aerodynamic Center Locations with Aspect Ratio for Some Wings (Refs. 4.11 and 4.12)

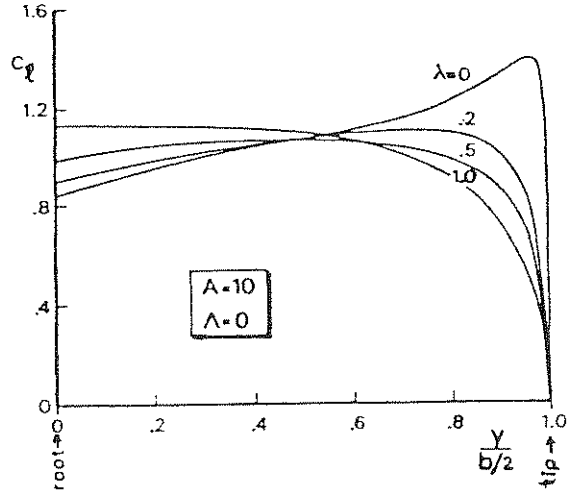

Figure 4.13 Lift Distribution at C_L = 1 for Straight Wings with Various Taper Ratios (Ref. 4.13)

4.5 WING STALL

Wing stall is due to flow separation. How the flow separation progresses chordwise and spanwise on a wing depends on the following items:

4.5.1 Airfoil Stall Characteristics

4.5.2 Planform Geometry and Twist

4.5.3 Stall Control Devices

Wing (or more generally lifting surface) stall behavior is important for the following reasons:

1. In FAR* 23 airplanes the stall speed at maximum weight cannot be more than 61 knots (for $W \leq 6{,}000$ lbs) and the bank angle, ϕ must not exceed 15° between onset of a stall with the wing level and completion of the recovery.

2. In FAR 25 airplanes an airplane must not reach more than $\phi = 20°$ between onset of a stall with the wing level and completion of the recovery.

3. It is generally of great interest for either performance or for stability and control reasons to achieve the highest possible $C_{L_{max}}$ on a wing (consistent with other mission oriented or manufacturing cost oriented constraints).

For these reasons the stall behavior of a wing are of great importance in airplane design.

4.5.1 AIRFOIL STALL CHARACTERISTICS

Airfoil stall behavior and the factors which affect it were discussed in Chapter 3. Sudden basic airfoil stall behavior does not necessarily mean sudden overall wing stall behavior. The effects of planform and thrust to be discussed in Subsection 4.5.2 can significantly alter the stall behavior of a wing as compared to the stall behavior of its airfoil(s).

4.5.2 EFFECT OF PLANFORM AND TWIST

The following planform effects are important in determining stall behavior.

4.5.2.1 Taper Ratio
4.5.2.2 Aspect Ratio

*Federal Aviation Regulation

4.5.2.3 Sweep Angle
4.5.2.4 Twist and Camber

4.5.2.1 Taper Ratio

A rectangular wing has a larger downwash angle at the tip than at the root. The effective angle of attack at the tip is thus reduced, and therefore, it will stall last. However, as shown in Section 4.2 it is aerodynamically inefficient, because the planform is far from elliptical so that it produces more induced drag. To reduce the induced drag, planform tapering to approximate the ideal elliptical planform is often used. With the tip chord reduced, the local Reynolds number and the induced angle of attack are decreased in the tip region. Therefore, the tip section will tend to stall first for a tapered wing. This is undesirable from a standpoint of lateral stability in stall entries and stall recovery.

Fig. 4.13 illustrates the effect of taper ratio on tip stall. It is seen that as the taper ratio is decreased, the tip loading tends to increase, thereby promoting tip-stall.

4.5.2.2 Aspect Ratio

With increasing aspect ratio a wing tends to behave more like an airfoil section (2-dimensional flow is being approximated except at the wing tip). For that reason it can be expected that $C_{L_{max}}$ increases with aspect ratio. However, experimental data indicate that the increase is slight (Ref. 4.14, p. 4-1). The effect can also be seen in Fig. 4.14a.

4.5.2.3 Sweep Angle

For swept aft wings since the wing tips are usually situated aft of the center of gravity, loss of lift at the tips causes the nose to come up. If the angle of attack is high originally, this will increase the angle of attack further. This may result in loss of pitch control. This phenomenon is known as pitch-up.

The reader will note that a swept forward wing would tend to exhibit pitch down.

In addition, because of the tendency toward spanwise flow, a swept-aft wing tends toward tip stall because of boundary layer thickening. A swept-forward wing, for the same reason, will tend toward root-stall.

The trend is for $C_{L_{max}}$ to decrease with sweep angle (fore and aft!) according to the so-called cosine scale (Ref. 4.15, p. 339):

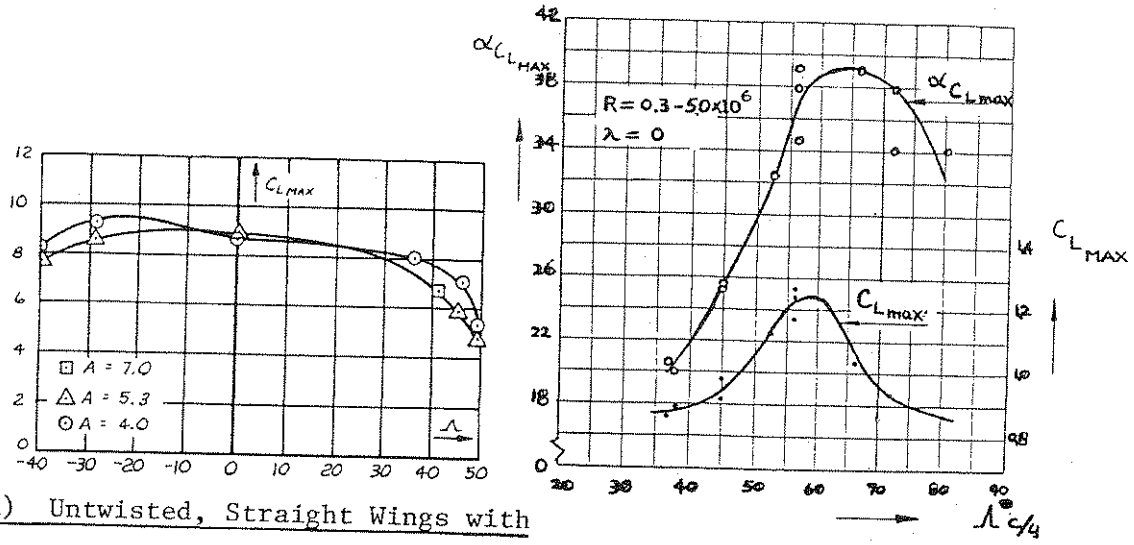

a) Untwisted, Straight Wings with Moderate Taper (Ref. 4.14, p. 16-6)

b) Delta Wings (Ref. 4.16)

Figure 4.14 Effect of Sweep Angle on $C_{L_{max}}$

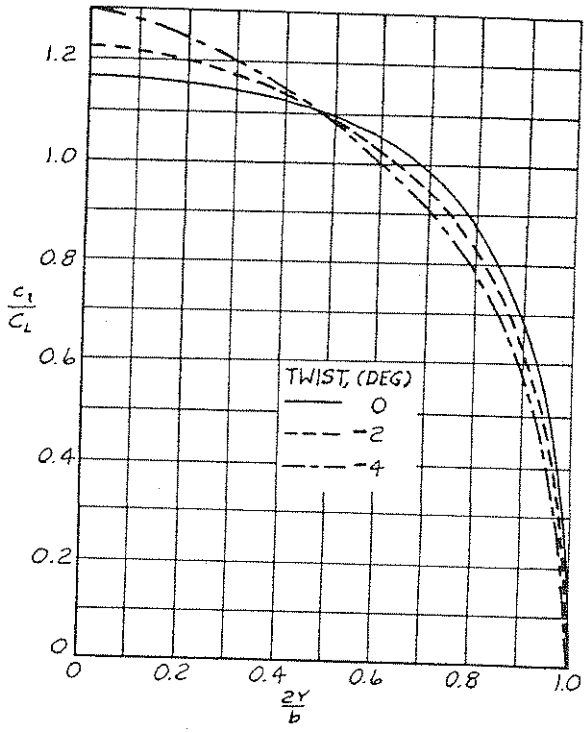

Figure 4.15 Effect of Spanwise Twist on Tip Stall. Unswept Rectangular Wing of A = 8.

$$C_{L_{max}}(\Lambda) = C_{L_{max}}(\Lambda = 0)\cos\Lambda \qquad (4.42)$$

Fig. 4.14 illustrates this trend (Ref. 4.14, p. 16-6).

4.5.2.4 Twist (or Wash-out)

If the angles of attack at various spanwise stations are not equal, the wing is said to have twist. If the angle of attack at the wing tip is less than that of the root, the wing is said to have washout. With washout, the tips will be at a lower α than the root, and thus the tip stall may be delayed until after the stall has occurred at the root.

Fig. 4.15 illustrates how tip stall is affected by a linear spanwise twist distribution.

4.5.3 STALL CONTROL DEVICES

Various devices may be used to delay tip stall. Some examples are listed below:

4.5.3.1 Wash-out

This was already discussed in Section 4.5.2. Table 4.2 illustrates the magnitude of washout used in several airplanes.

4.5.3.2 Variations in Section Shape

Different amounts of camber may be used at different spanwise positions.

4.5.3.3 Leading-edge Slats or Slots Near the Tip

It was already seen in Chapter 3 that leading edge slats or slots can significantly enhance $c_{\ell_{max}}$ of an airfoil. Such devices can and have been used over part of out-board span of wings to delay tip stall.

Examples of slatted wings are the F86 and the Sabre Liner. An example of a wing with a fixed slot is the Globe Swift. Movable slats are used on the DC9 and on the 727.

4.5.3.4 Stall Fences and Snags

Stall fences are used to prevent the boundary layer from drifting outward toward the tips due to the spanwise pressure gradient on a swept wing. An example is shown in Fig. 4.16a. Similar results can be attained with a leading edge snag as shown in Fig. 4.16b.

Table 4.2 Examples of Washout in Current Airplanes

Airplane Type	Wing Incidence At Root	At Tip	Washout
Cessna Stationair 6	1.5°	- 1.5°	3.0°
Cessna 310	2.5°	- .5°	3.0°
Cessna Titan	2.0°	- 1.0°	3.0°
Cessna Citation	2.5°	- .5°	3.0°
Beechcraft T-34C	4.0°	1.0°	3.0°
Beechcraft Baron	4.0°	0.0°	4.0°
Beechcraft Queenair	3.9°	0.0°	3.9°
Beechcraft King Air	4.8°	0.0°	4.8°
Piper Warrior II	2.0°	- 1.0°	3.0°
Piper Cheyenne	1.5°	- 1.0°	2.5°
Piper Tomahawk	2.0°	0.0°	2.0°

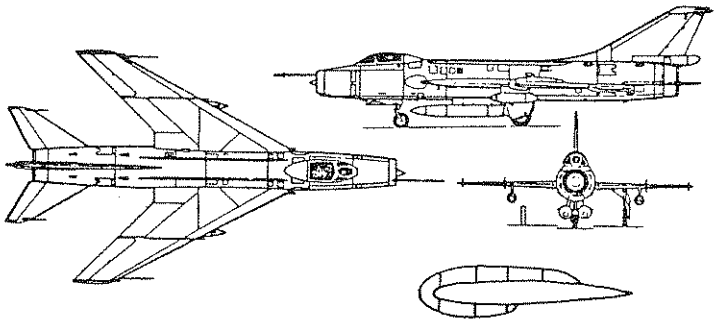

Figure 4.16 a) Example of a Stall Fence

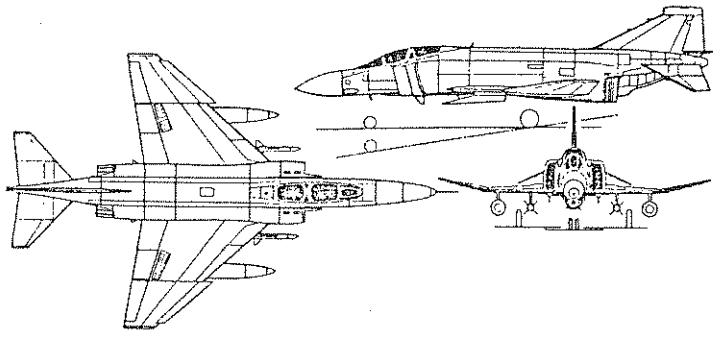

Figure 4.16 b) Example of a Leading Edge (Snag)

4.5.3.5 Stall Strips

Stall strips are usually small angular devices installed at the leading edge to induce stall at some angle of attack. They are often used as afterthoughts if the stall behavior of an airplane in flight is not satisfactory. Fig. 4.17 shows an example.

4.5.3.6 Vortex Generators

These are very small low aspect-ratio 'wings' placed vertically at some angle of attack on the wing surface. The generators will produce lift under these conditions and will also have associated tip vortices near the edge of the boundary layer. These vortices will mix the high energy fluid from the external stream with the shear layer near the surface. The result is a net increase in energy near the surface which allows the flow to advance farther into an adverse pressure gradient before separation. The size and location of the generators must be such as to penetrate through the boundary layer. The number of generators and the orientation on the wing has largely depended on flight test investigation. The use of vortex generators, while beneficial in delaying wing stall, will obviously produce additional drag. Fig. 4.18 illustrates a set of vortex generators and their effect on the GA(W)-1 airfoil.

Vortex generators are commonly found as 'aerodynamic afterthoughts' on airplanes. Virtually all jet transports exhibit rows of vortex generators on wings or on tails.

4.6 COMPRESSIBILITY EFFECTS

As already discussed in Section 3.5 compressibility effects can have serious adverse effects on drag, lift and pitching moment of airfoil sections. The same is true for wings.

Compressibility effects on airfoils can be delayed by thickness and camber tailoring (Section 3.7). On wings it is possible to delay compressibility effects by application of sweep. Fig. 4.19 shows two examples.

The freestream velocity vector can be resolved into components normal and parallel to the leading edge. The normal component is responsible for the aerodynamic characteristics, and its associated Mach number is $M_\infty \cos \Lambda$. It follows that if the critical Mach number for the same wing, but unswept is denoted by M^*, then the critical Mach number for the swept wing would be given by the relation:

$$M_{cr} \cos\Lambda = M^*$$

or,

$$M_{cr} = \frac{M^*}{\cos\Lambda} \qquad (4.43)$$

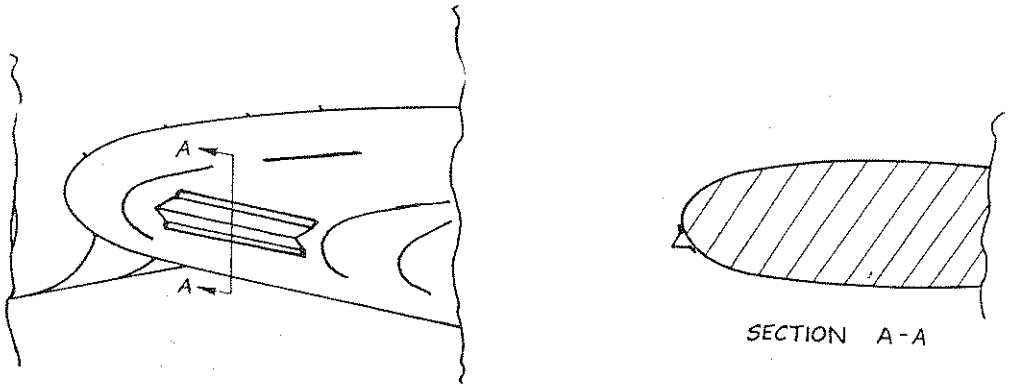

Figure 4.17 Example of a Stall Strip

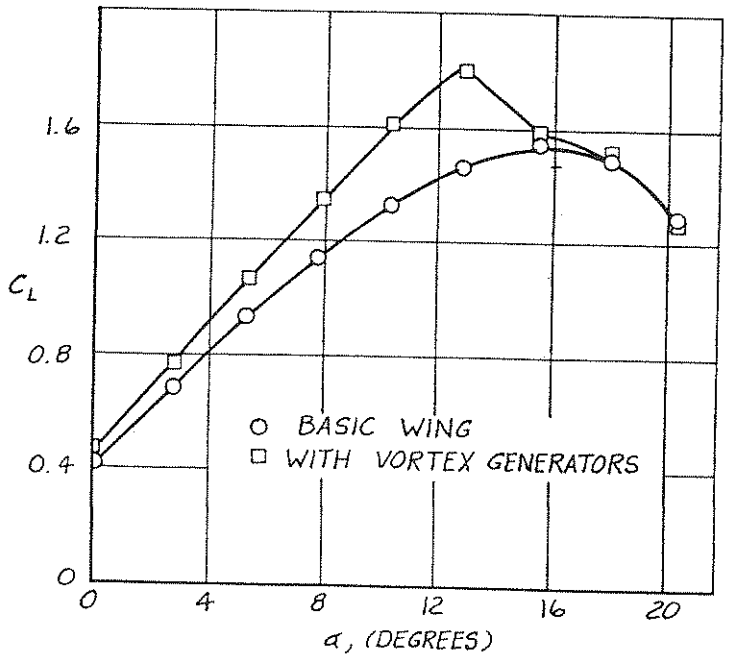

Figure 4.18 Effect of Vortex Generators on Lift (Ref. 4.17)

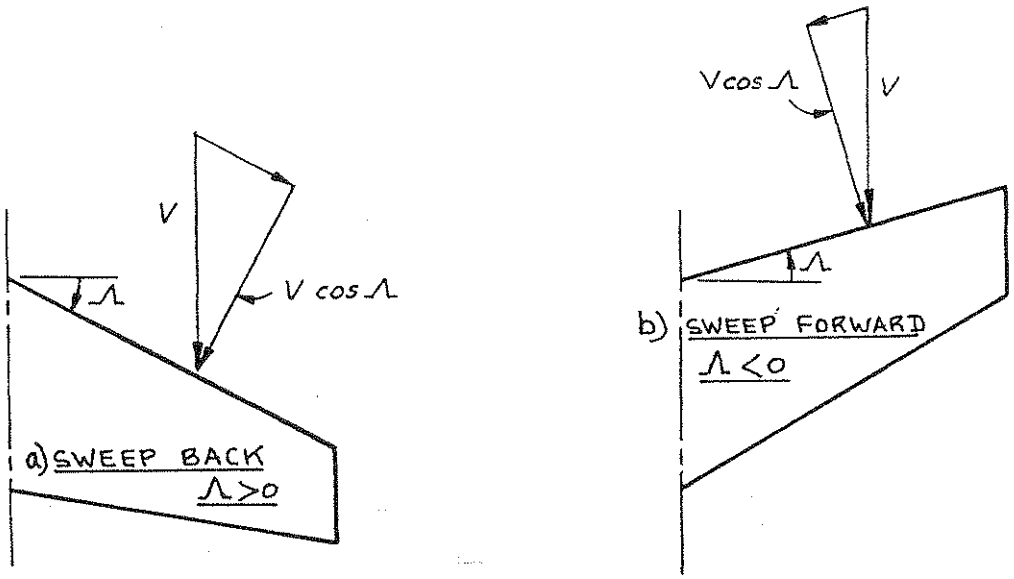

Figure 4.19 Example of Sweepback and Sweepforward

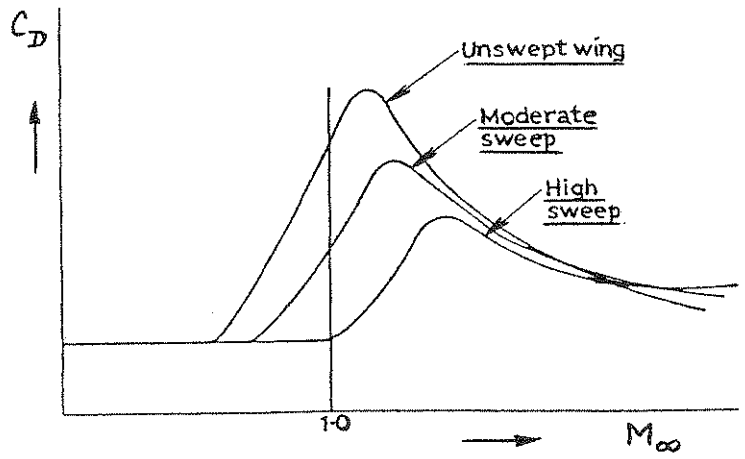

Figure 4.20 Effect of Wing Sweep on Delay of Drag Rise

The above result can also be interpreted in the following way. In a flow with M_∞, the sectional characteristics would correspond to an effective Mach number given by $M_{eff.} = M_\infty \cos\Lambda$. For example, if $M_\infty = 0.9$ which may exceed the drag divergence Mach number for an unswept wing, the effective Mach number for a swept wing with $\Lambda = 30°$ is:

$$M_{eff} = 0.9 \cos 30° = 0.779$$

which may be below the M_{dd}. Thus, it is possible with a highly swept wing to delay to high M_∞ the troublesome aerodynamic characteristics associated with transonic flow. The above argument is exactly valid only in two-dimensional flow. The 3-D effects near the tips and the root will make such a simple relationship too optimistic. A useful empirical formula for an approximate value of M_{cr} is (Ref. 4.18, p. 103):

$$M_{cr} = M^* \sqrt{\sec\Lambda} \tag{4.44}$$

Experiment shows that the use of sweepback not only increases M_{dd}, but also reduces the rate at which the drag coefficient rises in the transonic region. This is illustrated in Fig. 4.20.

Experiment also shows that, other things being equal, a reduction in aspect ratio gives a rise in M_{dd}, and so helps to reduce transonic drag (Ref. 4.19, p. 15-16). This reduction would more than compensate for the associated increase in induced drag.

For low aspect-ratio wings, edge vortex separation becomes important. Leading-edge vortex separation is illustrated in Fig. 4.21. The vortex creates low pressure on the upper surface, and thus produces vortex lift. The vortex separation can also occur along the tip chord and along wing or body mounted strakes. In transonic flow, the interaction of vortex flow with shock waves can create quite a complex flow field.

4.7 HIGH LIFT DEVICES, SPOILERS, DIVE BRAKES, SPEED BRAKES

From the definition of lift coefficient, the speed in level flight is given by:

$$V = \sqrt{\frac{2L}{\rho C_L S}} = \sqrt{\frac{2}{\rho C_L}\frac{W}{S}} \tag{4.45}$$

If $C_{L_{max}}$ is used in Eqn. (4.45), the stall speed is obtained as:

$$V_s = \sqrt{\frac{2}{\rho C_{L_{max}}}\frac{W}{S}} \tag{4.46}$$

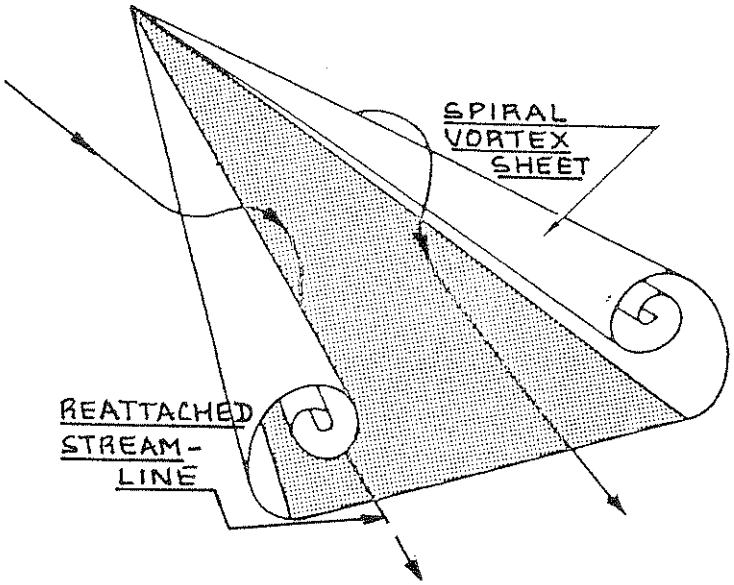

Figure 4.21 Example of Leading Edge Vortex Flow Separation

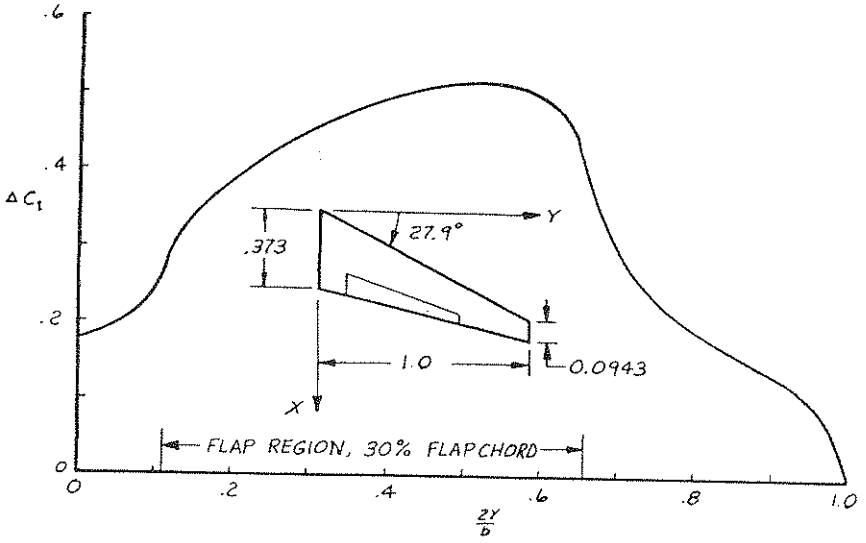

Figure 4.22 Incremental Lift Coefficient Due to Flap Deflection at α = 10 deg. and δ = 10 deg.

The ratio, W/S, is defined as the wing loading. Since take-off and landing speeds depend on V_s, it is necessary to reduce V_s wherever short runways are to be used. From Eqn. (4.46) it is seen that V_s can be reduced if $C_{L_{max}}$ and/or S can be increased. Devices which increase the lift can be classified into two categories: change in airfoil geometry and boundary layer control (BLC). In practical applications, they may be grouped into trailing-edge flaps, leading-edge devices and BLC devices. Sectional characteristics of these high lift devices have been discussed in Section 3.8. In the following, some three-dimensional effects will be discussed.

Although progress has been made in the past toward theoretical prediction of $C_{L_{max}}$, the current state-of-art methods are still not satisfactory. Therefore, only semi-empirical methods will be discussed. In all these methods, knowledge of sectional characteristics, $c_{\ell_{max}}$ is in general the starting point for any three-dimensional calculation. The latter is made by applying corrections for partial span effect, fuselage interference, etc. A method for estimating incremental lift due to trailing edge flaps below the stall angle will be discussed first.

4.7.1 LIFT INDUCED BY PARTIAL-SPAN FLAPS BELOW STALL

Fig. 4.22 shows calculated results for a swept wing with a partial span flap deflected by 10 degrees at α = 10 degrees (Ref. 4.6). It is seen that the incremental sectional lift coefficient due to the flap varies considerably inside the flap region and Δc_ℓ is still quite significant outside the flap region. This is due to the three-dimensional induction effect (carry-over effect). Although theoretical methods are accurate enough to calculate the carry-over effect at low flap angle and at low angle of attack, at high angles experimental results should be used. When sectional data are available, the method of Lowry and Polhamus (Ref. 4.3) is applicable for estimating the total incremental lift coefficient ΔC_L. This is summarized below.

Let:

$$\Delta C_L = \frac{\partial C_L}{\partial \delta} \delta K_b = C_{L_\delta} \delta K_b \qquad (4.47)$$

where δ is the flap angle and K_b is the flap span factor defined as the ratio of partial-span-flap lift coefficient to full-span lift coefficient. The three-dimensional induction effect noted above is accounted for through K_b. By proper multiplication and division by the same parameters, Eqn. (4.47) can be rewritten as:

$$\Delta C_L = \frac{C_{L_\delta}}{c_{\ell_\delta}} (c_{\ell_\delta} \delta) K_b = \frac{C_{L_\delta}/C_{L_\alpha}}{c_{\ell_\delta}/c_{\ell_\alpha}} \frac{C_{L_\alpha}}{c_{\ell_\alpha}} \Delta c_{\ell_f} K_b \tag{4.48}$$

where Δc_{ℓ_f} is the sectional lift coefficient increment due to flap.

Let:

$$K_c = \frac{C_{L_\delta}/C_{L_\alpha}}{c_{\ell_\delta}/c_{\ell_\alpha}} \tag{4.49}$$

be the so-called flap-chord factor. It follows that Eqn. (4.48) becomes:

$$\Delta C_L = \Delta c_{\ell_f} \left(\frac{C_{L_\alpha}}{c_{\ell_\alpha}}\right) K_c K_b \tag{4.50}$$

The ratio of lift-curve slopes in three-dimensional and two-dimensional flow can be estimated with Eqn. (4.32):

$$\frac{C_{L_\alpha}}{c_{\ell_\alpha}} = \frac{A}{\frac{a_\infty}{\pi} + \sqrt{A^2\left(1 + \frac{\tan^2 \Lambda_{c/2}}{\beta^2}\right) + \left(\frac{a_\infty}{\pi}\right)^2}} \tag{4.51}$$

The flap-chord factor has been calculated theoretically and is shown in Fig. 4.23. The flap-span factor can also be calculated theoretically. However, the empirical results given in Fig. 4.24 are known to be more accurate. Note that K_b obtained at a given b_f from Fig. 4.24 is for a flap span starting at the root chord and extending to station b_f. If an outboard partial-span flap is involved, the K_b-value to be used in Eqn. (4.50) should be the difference in K_b-values for the outboard and inboard stations of the flap span. This is illustrated in Fig. 4.25.

Example: For the wing in Fig. 4.22 with a partial span flap deflected at 10 degrees, find ΔC_L at M = 0.2. This wing is of A = 8.5, $\Lambda_{c/2}$ = 21.3 degrees. The inboard and outboard stations of the flap are at 0.110 and 0.655 of the semispan, respectively.

Solution: For a taper ratio of 0.253, K_b are found from Fig. 4.24 to be 0.8 and 0.16 for $b_f/b/2$ = 0.655 and 0.110, respectively.

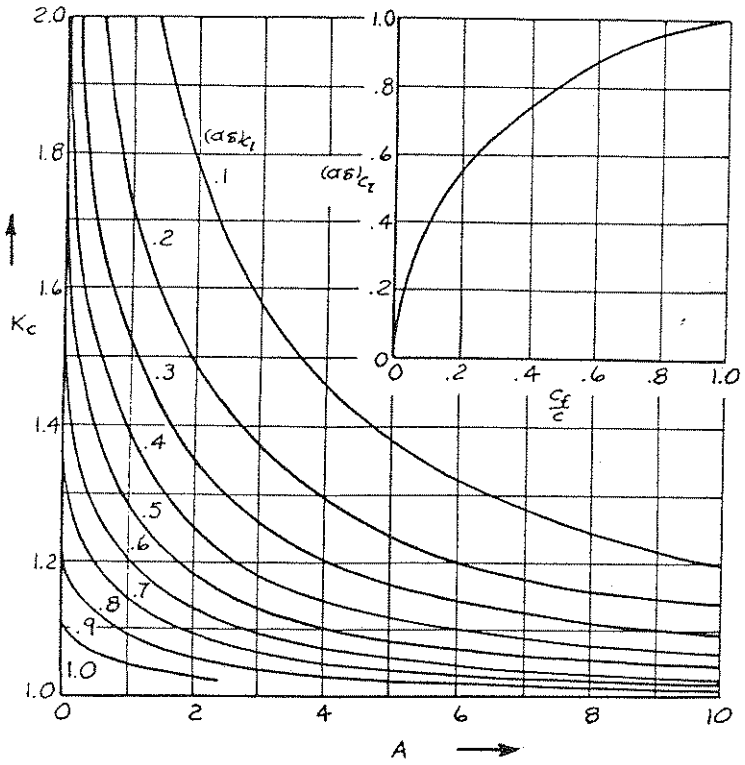

Figure 4.23 Variation of Flap-Chord Factor with $(a_\delta)_{c_\ell}$ and Aspect Ratio (Data From Ref. 4.3)

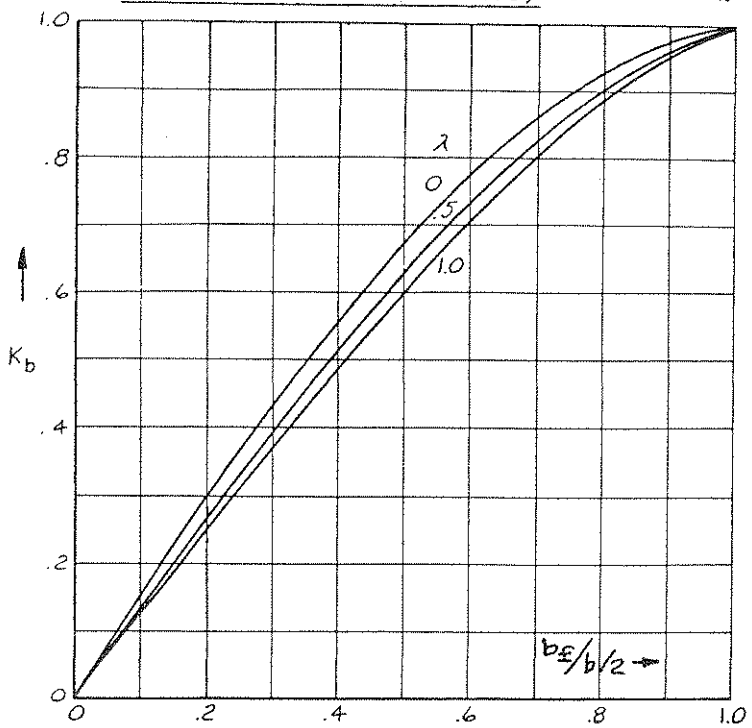

Figure 4.24 Variation of Span Factor K_b with Flap Span for Inboard Flaps. (Data From Ref. 4.3)

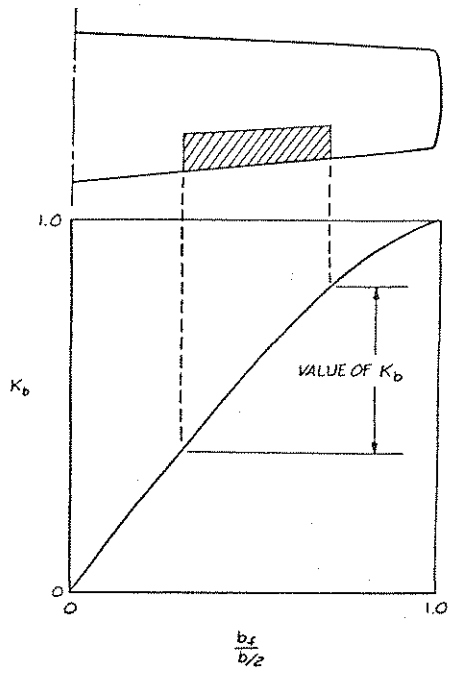

Figure 4.25 Span Factor for Flaps Other Than Inboard Flaps

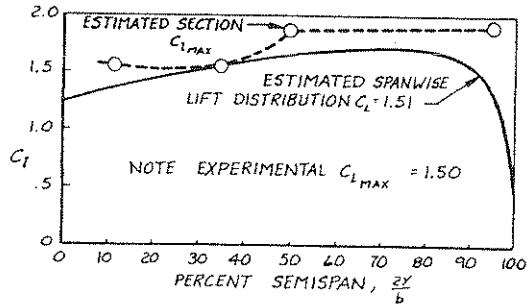

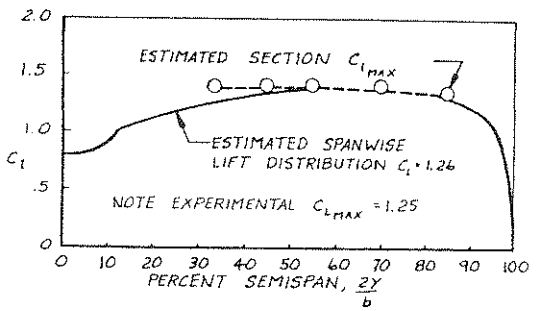

Figure 4.26 Determination of Clean Wing Maximum Lift Coefficient

At $c_f/c = 0.3$, from Fig. 4.23, $(\alpha_\delta)_{c_\ell}$ is found to be 0.66.

Hence, $K_c = 1.025$ for A = 8.5. Now Eqn. (4.51) shows that, assuming $a_\infty = 2\pi$,

$$\frac{C_{L_\alpha}}{c_{\ell_\alpha}} = \frac{8.5}{2 + \sqrt{8.5^2\left(1 + \frac{\tan^2 21.3°}{(1-0.2^2)}\right) + 4}} = 0.748$$

If experimental sectional data are available for Δc_{ℓ_f}, Eqn. (4.50) can then be used to calculate ΔC_L. For the present purpose, the following theoretical results (Ref. 4.6) will be used:

$$\Delta c_{\ell_f} = 2\delta(\tau + \sin\tau) \tag{4.52}$$

$$\tau = \cos^{-1}(2x_f - 1) \tag{4.53}$$

$$x_f = 1 - c_f/c \tag{4.54}$$

It follows that:

$$\tau = \cos^{-1}(2 \times 0.7 - 1) = 66.42° = 1.1592 \text{ rad}$$

$$\Delta c_{\ell_f} = 2 \times \frac{10 \times \pi}{180}(1.1592 + \sin 66.42°) = 0.725$$

$$\Delta C_L = 0.725 \times 0.748 \times 1.025 \times (0.8 - 0.16) = 0.356$$

This is comparable to 0.333 found by the lifting-surface method of Ref. 4.6.

4.7.2 MAXIMUM LIFT COEFFICIENT WITH HIGH LIFT DEVICES (REF. 4.20)

A popular method of estimating wing maximum lift coefficient with high lift devices is to add increments of maximum lift due to the leading and trailing-edge high lift devices to the maximum lift for the clean wing. The clean wing maximum lift will be discussed first.

4.7.2.1 Clean Wing Maximum Lift

For high aspect-ratio wings with moderate sweep angles, the maximum lift is, to a large extent, determined by the sectional maximum lift. A practical assumption in estimating the wing $C_{L_{max}}$ in this case is that the complete wing attains the maximum lift when

any section reaches its $c_{\ell_{max}}$. This is because once a section is stalled, the flow separation spreads quickly to neighboring sections as the angle of attack is increased. As a result, the wing will lose part of its lifting ability.

For this type of wings, $C_{L_{max}}$ can be estimated as follows. Assume that the sectional maximum lift coefficient, $c_{\ell_{max}}$, is known at all spanwise stations. The $c_{\ell_{max}}$ distribution is then plotted, as illustrated by the dashed line in Fig. 4.26. Next, a lifting-surface loading program* is used to produce the spanwise lift distribution over a range of angles of attack. The wing maximum lift coefficient is that calculated value at which the local lift coefficient at any station first reaches $c_{\ell_{max}}$ at that station. This approach is illustrated in Fig. 4.26. For the 24-deg swept wing, the estimated $C_{L_{max}}$ is 1.51. This compares with tunnel data of 1.5. For the 35-deg swept wing, the estimated value is 1.26. The measured $C_{L_{max}}$ for this configuration is 1.25. As it can be seen, the accuracy is quite good for both cases.

It should be noted that as the sweep is increased and the aspect ratio is reduced, the three-dimensional induction effect becomes more pronounced, with a resulting departure from two-dimensional characteristics. When edge-separated vortex flow is present (see Section 4.6), wing stall can be delayed to a larger angle of attack. In all these cases, the flow characteristics are quite three-dimensional. Ref. (4.9) presents a method for estimating $C_{L_{max}}$ for this type of configurations with constant-section untwisted wings.

4.7.2.2 Maximum Lift Increment Due to High Lift Devices

For efficient trailing-edge flaps, the sectional value of flap maximum lift increment can be used to calculate the three-dimensional value by the following empirical relation:

$$(\Delta C_{L_{max}})_{flap} = (\Delta c_{\ell_{max}})\left(\frac{S_{wf}}{S_w}\right)K_\Lambda \qquad (4.55)$$

where S_{wf}/S_w is the ratio of the wing area affected by the trailing edge flap to the total wing area. The factor K_Λ is empirically

*Such as that of Ref. 4.6.

derived to account for the effects of wing sweep and is given by Ref. 4.20 as:

$$K_\Lambda = (1 - 0.08 \cos^2 \Lambda_{c/4}) \cos^{3/4} \Lambda_{c/4} \tag{4.56}$$

Other methods are available, see for example, Ref. 4.13.

For leading-edge devices, the sweep effect is more pronounced. The incremental $C_{L_{max}}$ can be written according to (Ref. 4.13, p. 549) as:

$$(\Delta C_{L_{max}})_{\text{L.E. Devices}} = (\Delta c_{\ell_{max}}) \left(\frac{S_{wf}}{S_w}\right) \cos^2 \Lambda_{c/4} \tag{4.57}$$

It should be noted that the estimated $C_{L_{max}}$ may be reduced by flow around flap tracks and supports, interference with engine nacelles, aeroelastic deformation, unforseen leakage paths, etc.

4.7.2.3 Examples of Maximum Lift Coefficient

Some typical attainable maximum lift coefficients on various configurations are presented in Table 4.3. The first twelve configurations represent earlier technology (before 1957) and the data were compiled in Ref. 4.22. More recent technology typified by the last three configurations in Table 4.3 indicates that much higher maximum lift coefficients can be obtained with improved airfoil sections and high lift devices.

4.7.3 EFFECT OF TAIL ON MAXIMUM LIFT

Application of high-lift devices results in a significant change in pitching moment. Trailing-edge flaps usually generate a more nose-down (negative) moment, while leading-edge devices produce a more nose-up (positive) moment. These pitching moments must be balanced (trimmed) by a horizontal stabilizer, such as a tail. Since the trailing-edge flap is more effective in producing high lift, the use of it requires a larger down-load on the tail to trim. It follows that the tail will decrease the usable wing maximum lift.

To see the tail effect quantitatively, refer to Fig. 4.27. Let the total lift coefficient be C_L. Then:

$$C_L = C_{L_W} + C_{L_T} \tag{4.58}$$

Taking the moment about the c.g. and setting the resulting pitching moment to zero for trim, it is obtained that:

$$-C_{L_W} \bar{q}S (x_{ac} - x_{cg}) + C_{m_{ac}} \bar{q}S\bar{c} - C_{L_T} \bar{q}S\ell_T = 0$$

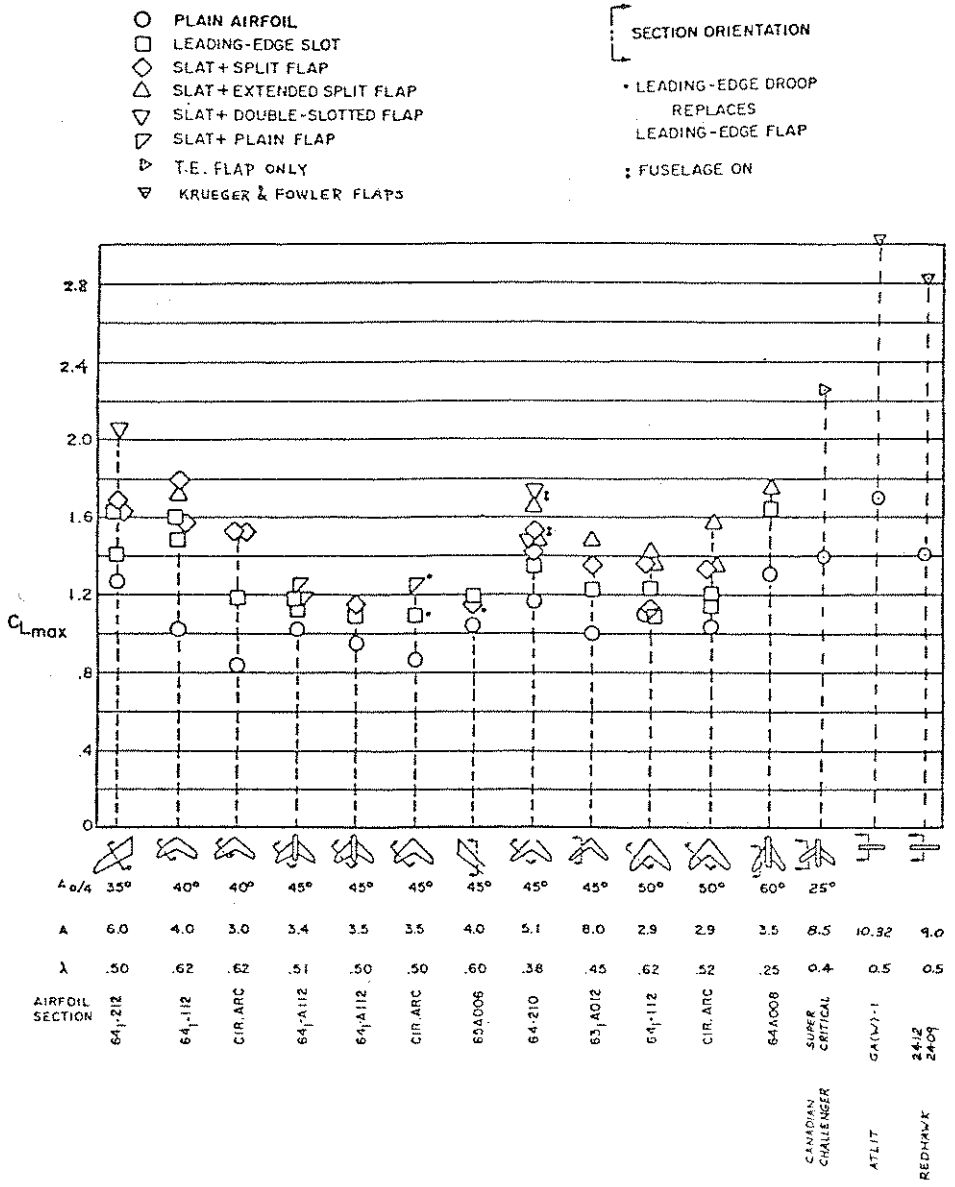

Table 4.3 Summary Chart of Maximum Lift Coefficient Obtained With Various Types of High Lift Devices (Ref. 4.21)

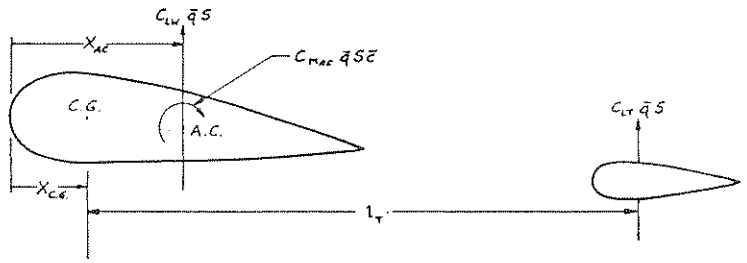

Figure 4.27 Geometry to Illustrate the Tail Effect

which can be solved for the tail lift C_{L_T}:

$$C_{L_T} = -C_{L_W} \frac{x_{ac} - x_{cg}}{\ell_T} + C_{m_{ac}} \frac{\bar{c}}{\ell_T} \tag{4.59}$$

From Eqns. (4.58) and (4.59), it follows that:

$$C_L = C_{L_W} \left(1 - \frac{x_{ac} - x_{cg}}{\ell_T}\right) + C_{m_{ac}} \frac{\bar{c}}{\ell_T} \tag{4.60}$$

In most cases, $x_{ac} > x_{cg}$ so that the term in the parentheses of Eqn. (4.60) is less than one. The wing lift contribution is therefore reduced. In the meantime, $C_{m_{ac}}$ becomes more negative by the deflection of trailing-edge flaps. Hence, the usable airplane maximum lift is further decreased by the second term of Eqn. (4.60).

It should be noted that a forward mounted tail plane (canard) will produce more favorable overall $C_{L_{max}}$ values.

4.7.4 SPOILERS, DIVE BRAKES AND SPEED BRAKES

These devices are either to destroy lift, or add drag to the airplane. See Fig. 4.28.

It is often advantageous to employ spoilers on the wing, not only for direct lift control (DLC) but also to provide additional roll control. This will free the trailing edge for full-span high lift devices. An example of this technology is the Advanced Technology Light Twin-Engine Airplane (ATLIT) (Ref. 4.23). Other recent applications of this approach are several Robertson STOL Conversions (Ref. 4.24), the new Mooney 321 and the Mitsubishi Diamond I.

To prevent airplanes from exceeding the speed and Mach number for which they are designed, or to increase the glide angle, dive flaps or speed brakes are used.

4.8 SUMMARY

In this chapter, the reader has been given an insight into the lift, drag and pitching moment behavior of lifting surfaces. The section characteristics discussed in Chapter 3 form a necessary basis for predicting these characteristics. Methods used were both theoretical and empirical.

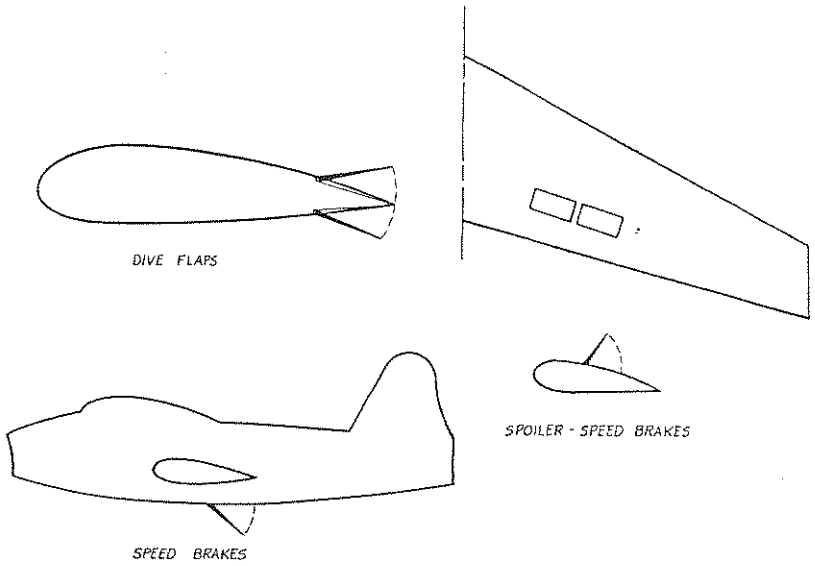

Figure 4.28 Typical Configurations of Spoilers, Dive Brakes and Speed Brakes

Problems for Chapter 4

4.1 A straight, tapered wing of 30 ft. span has leading-edge and trailing-edge sweep angles of 45° and 15°, respectively. Its total area is 280 sq. ft. Find the magnitudes of root chord, tip chord and the mean aerodynamic chord.

4.2 The test results of the NACA 23012 airfoil show the following:

α°	c_ℓ
0	0.15
9	1.2

If this airfoil is used to construct an elliptical wing of A = 7.0, determine the wing lift curve slope.

4.3 A rectangular wing model of 40 in. by 5 in. has the following characteristics determined from a wind tunnel test: e = 0.87, C_{L_α} = a = 0.09 per deg. and α_o = -3°. If a full-scale rectangular wing of 42 ft. by 6 ft. is constructed with the same airfoil section, what lift will it develop at α = 5° and 120 mph under standard sea-level conditions? Assume e = 0.87 for the full-scale wing.

4.4 The following data are obtained from a wind tunnel test of a wing (A = 10.32) for an advanced light twin airplane:

α°	C_L	C_D
-2	0.0634	0.0060
0	0.2598	0.0083
2	0.4545	0.01413
4	0.6483	0.0231
6	0.8412	0.0349
8	1.0327	0.0495
10	1.2217	0.0668
12	1.4059	0.0865

Determine the drag polar equation if Eqn. (4.36) is assumed applicable.

4.5 The following data are obtained from a wind tunnel test of a wing:

At $C_L = 0$, $C_{m(\bar{c}/4)} = -0.126$

At $C_L = 0.6$, $C_{m(\bar{c}/5)} = -0.15$

Find the a.c. location and $C_{m_{ac}}$. Assume small angles of attack.

4.6 An airplane weighing 5000 lb. has a wing area of 250 ft^2. If the lift-curve slope is 6.0 per radian and the angle of zero lift is -2 deg., calculate the angle of attack (in degrees) of this airplane at a level flight speed of 200 mph under standard sea-level conditions.

4.7 How fast must the wing of Prob. 4.4 travel at α = 4° to produce a lift of 1.87 KN at 9,000 ft. altitude? Assume standard atmospheric conditions. S = 155 sq. ft.

4.8 A low-speed airplane has the following characteristics:

Airfoil: NACA 23012, with a_∞ as shown in Prob. 4.2. $\alpha_o = -1.8°$.

Aspect ratio = 9 and $\lambda = 0.5$

$\Lambda_{c/2} = 0.$ $b = 31.4$ ft.

It is equipped with a partial span flap as shown in the following sketch. During take-off, the angle of attack is set at 8 degrees. Determine the flap angle to generate a total lift coefficient of 1.34. (Hint: Use Eqns. 4.32 and 4.52).

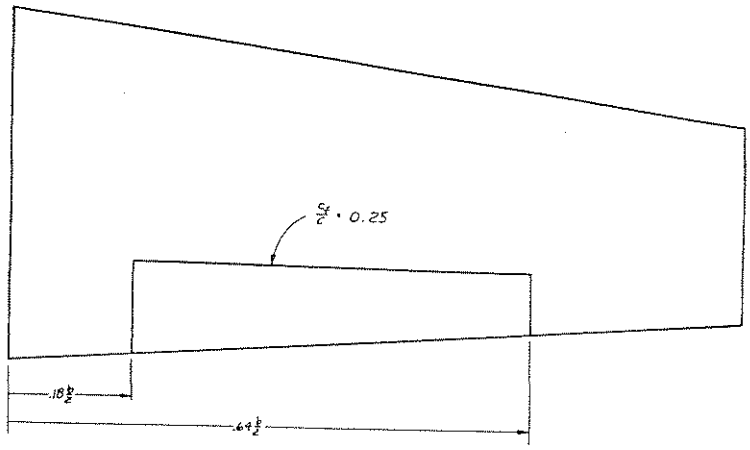

References for Chapter 4

4.1 Glauert, H., "The Elements of Aerofoil and Airscrew Theory," Cambridge University Press, 1959.

4.2 Abbott, I. A. & von Doenhoff, A. E., "Theory of Wing Sections," Dover, 1959.

4.3 Lowry, J. G. & Polhamus, E. C., "A Method for Predicting Lift Increments due to Flap Deflection at Low Angles of Attack in Incompressible Flow," NACA TN 3911, 1957.

4.4 Giesing, J. P., "Lifting Surface Theory for Wing-Fuselage Combinations," Report DAC-67212 Vol. 1, McDonnell Douglas Aircraft Co., August 1, 1968.

4.5 Margason, R. J. & Lamar, J. E., "Vortex-Lattice Fortran Program for Estimating Subsonic Aerodynamic Characteristics of Complex Planforms," NASA TN D-6142, February, 1971.

4.6 Lan, C. E., "A Quasi-Vortex-Lattice Method in Thin Wing Theory," Journal of Aircraft, Vol. 11, September 1974, pp. 518-527.

4.7 Osborne, R. S. & Kelly, T. C., "A Note on the Drag Due to Lift of Delta Wings at Mach Numbers up to 2.0," NASA TN D-545, 1960.

4.8 Relf, E. F., "Note on the Lift Slope and Some Other Properties, of Delta and Swept-Back Wings," Aeronautical Research Council of Great Britain, R & M, No. 3111, 1959.

4.9 Hoak, D. E., et al., USAF Stability and Control Datcom, Air Force Flight Dynamics Laboratory, Wright-Patterson Air Force Base, Ohio, Revised April 1978.

4.10 Roskam, J., "Airplane Flight Dynamics and Automatic Flight Controls," Part I, Roskam Aviation and Engineering Corporation, Rt. 4, Ottawa, KS, 66067, 1979.

4.11 Truckenbrodt, E., "Experimentelle Und Theoretische Untersuchungen An Symmetrisch Angeströmten Pfeil-Und Deltaflügeln," Zeitschrift Für Flugwissenschaften, Band 2; 1953, p. 185/201.

4.12 Shortal, J. A. and Maggin, B., "Effect of Sweepback and Aspect Ratio on Longitudinal Stability Characteristics of Wings at Low Speeds," NACA TN 1093, July 1946.

4.13 Torenbeek, E., "Synthesis of Subsonic Airplane Design," Delft University Press 1976.

4.14 Hoerner, S. F. and Borst, H. V., "Fluid-Dynamic Lift," Published by L. A. Hoerner, 1975.

4.15 Wimpenny, J. C., "The Design and Application of High Lift Devices," in "International Congress on Subsonic Aeronautics," Annals of the New York Academy of Sciences, Vol. 154, Art. 2, November 1968.

4.16 Rose, R. G., "A note on the estimation of some low speed characteristics of delta wings," Cranfield College of Aeronautics Report No. 68, 1953.

4.17 Wentz, W. H., Jr. and Seetharam, H. C., "Development of a Fowler Flap System for a High Performance General Aviation Airfoil," NASA CR-2443, December 1974.

4.18 Perkins, C. D. and Hage, R. E., "Airplane Performance, Stability and Control," John Wiley, New York 1949.

4.19 Hoerner, S. F., "Fluid-Dynamic Drag," Published by the author, 1965.

4.20 Callaghan, J. G., "Aerodynamic Prediction Methods for Aircraft at Low Speeds with Mechanical High Lift Devices," Paper No. 2 in "Prediction Methods for Aircraft Aerodynamic Characteristics," AGARD-LS-67, 1974.

4.21 Nicolai, L. M., "Fundamentals of Aircraft Design," University of Dayton, 1975.

4.22 Furlong, G. C. and McHugh, J. G., "A Summary and Analysis of the Low Speed Longitudinal Characteristics of Swept Wings at High R_e," NACA Report 1339, 1957.

4.23 Holmes, B J., "Flight Evaluation of an Advanced Technology Light Twin-Engine Airplane (ATLIT)," NASA CR-2832, July 1977.

4.24 Taylor, J. W. R., "Jane's All the World's Aircraft," 1980-1981 Jane's Publishing Company, London, England.

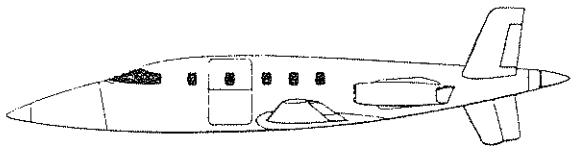

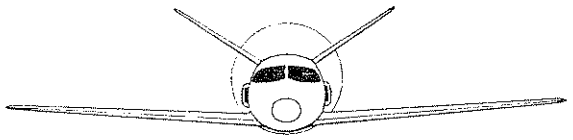

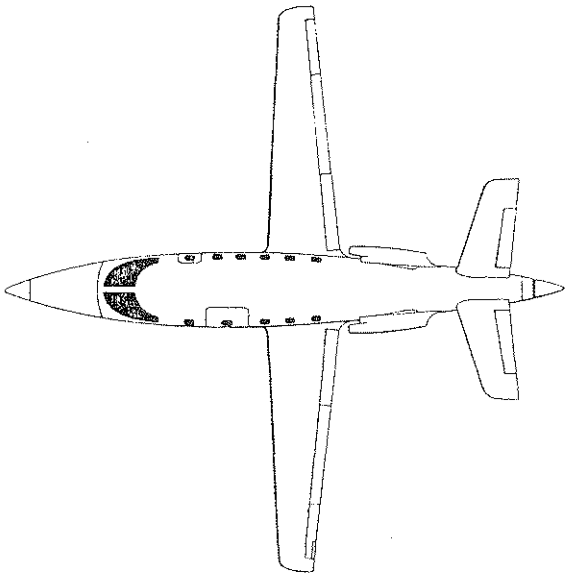

5. AIRPLANE DRAG

The purpose of this chapter is to familiarize the reader with the basic principles of airplane drag. The most important drag sources will be pointed out and explained. Mathematical and experimental techniques used in representing and predicting drag are presented.

Section 5.1 presents a discussion of complete airplane drag behavior. To understand where the contributions to drag originate, a more detailed discussion is given in Section 5.2.

A discussion of windtunnel testing procedures is presented in Section 5.3.

A simple method for estimating airplane drag polars is given in Section 5.4. For more detailed methods, the reader is referred to Refs. 5.1 and 5.2.

5.1 COMPLETE AIRPLANE POLARS

5.1.1 CLEAN AIRPLANE

A clean airplane is defined as an airplane in its cruise configuration.

For conventional airplanes it is often possible to represent the relationship between clean airplane drag- and lift-coefficients by the following parabolic form:

$$C_D = C_{D_o} + \frac{C_L^2}{\pi A e} \tag{5.1}$$

where: C_{D_o} is the so-called zero lift drag coefficient

and: e is Oswald's efficiency factor. A value of e=1 would indicate an elliptical lift distribution.

Magnitudes for C_{D_o} and e in a practical situation are found from experimental, theoretical and/or empirical methods.

Fig. 5.1 shows an example of a theoretical drag polar in accordance with Eqn. 5.1. Point A indicates the point of maximum lift-to-drag ratio. The reader is asked to verify that at Point A:

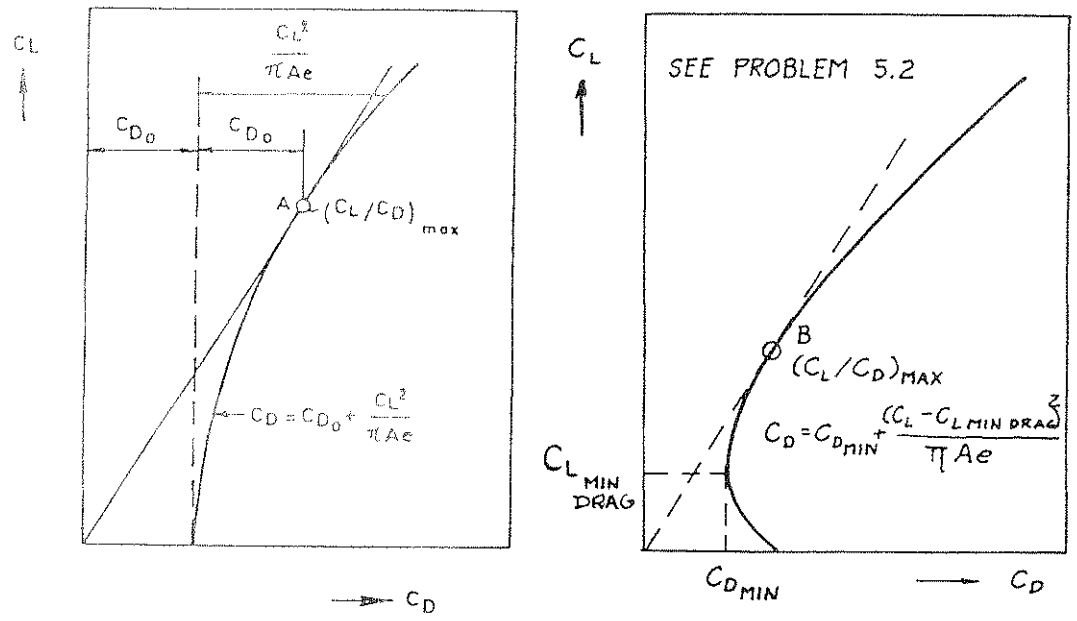

Figure 5.1 Example Drag Polar According to Eqn. (5.1) and Eqn. (5.3)

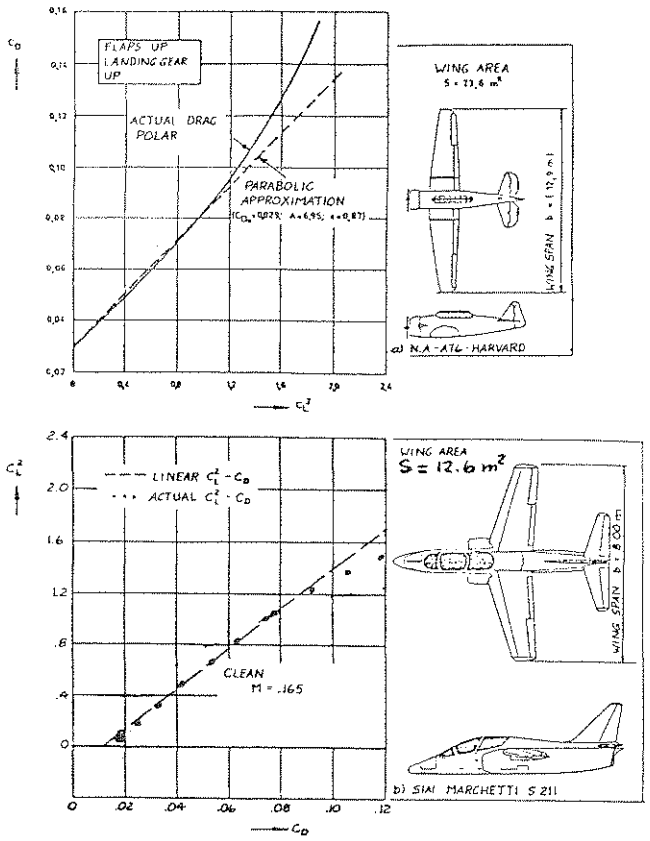

Figure 5.2 Actual Drag Polars of Trainer Airplanes Compared With Their Parabolic Approximation of Eqn. (5.1)

$$C_D = 2C_{D_o} \text{ at } C_L \text{ for } C_L/C_D\Big|_{max}$$

and

$$C_L \text{ for } C_L/C_D\Big|_{max} = \sqrt{\pi A e C_{D_o}} \qquad \} \qquad (5.2)$$

Fig. 5.2 presents two comparisons of actual drag polars with their theoretical form according to Eqn. (5.1). It is seen that the parabolic approximation is reasonable only for a limited range of C_L-values. One reason is that at high C_L-values the flow will start to separate. This creates extra drag.

The two airplanes of Fig. 5.2 differ widely in drag levels. This is due in part to the propulsion system differences (jets are 'cleaner' than props) and in part due to better aerodynamic design.

In general it is found that Eqn. (5.1) represents airplane drag reasonably well only for low subsonic airplanes with wings without a significant amount of camber and twist. The S-211 of Fig. 5.2 does have highly cambered airfoils which is one reason why $C_{D_o} \neq C_{D_{min}}$.

For airplanes such as the S211, with significantly cambered and twisted wings a better drag-polar representation is obtained with Eqn. (5.3):

$$C_D = C_{D_{min}} + \frac{(C_L - C_{L_{\substack{min \\ drag}}})^2}{\pi A e} \qquad (5.3)$$

where $C_{D_{min}}$ is the minimum drag coefficient and $C_{L_{\substack{min \\ drag}}}$ is the corresponding value for C_L.

At high subsonic speeds, whenever shock waves occur and/or where shock induced boundary layer separation occurs, it is found that actual airplane drag rises considerably more rapidly than indicated by the parabolic representations of Eqn. (5.1) or (5.3).

Figure 5.3 illustrates the drag rise behavior of a high subsonic jet trainer and a jet transport airplane. A cross plot of C_D versus Mach Number for constant C_L-values is often used to illustrate the drag-rise behavior of an airplane. For the airplanes of Figure 5.3 this is illustrated in Figure 5.4.

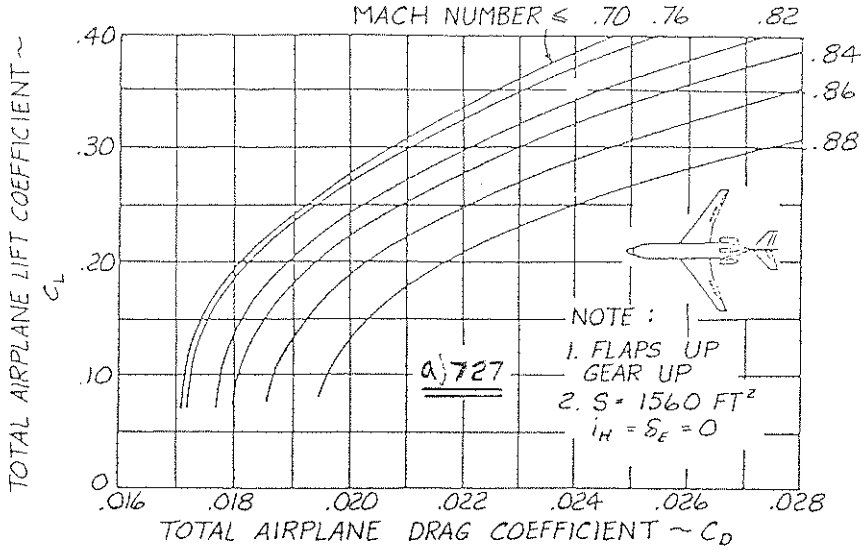

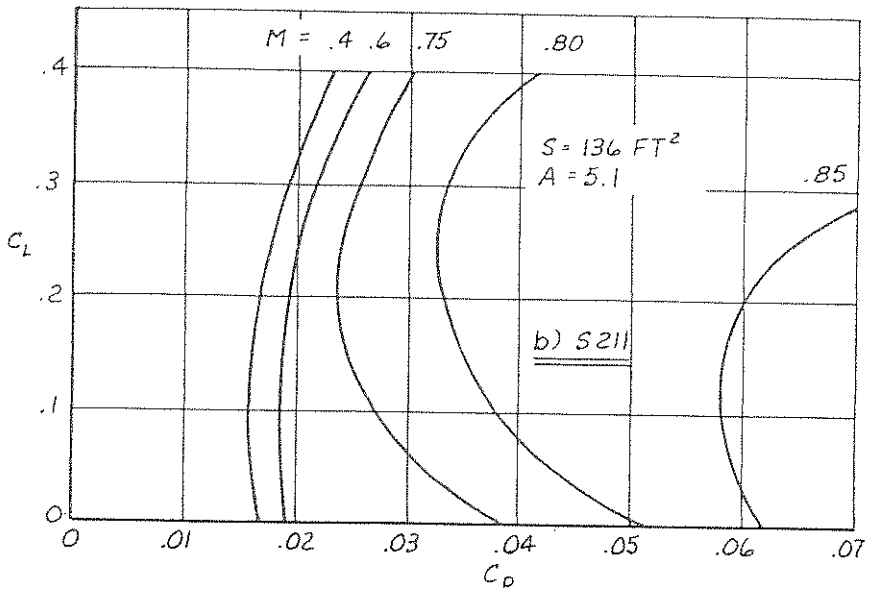

Figure 5.3 Examples of Drag Rise Due to Compressibility Effects

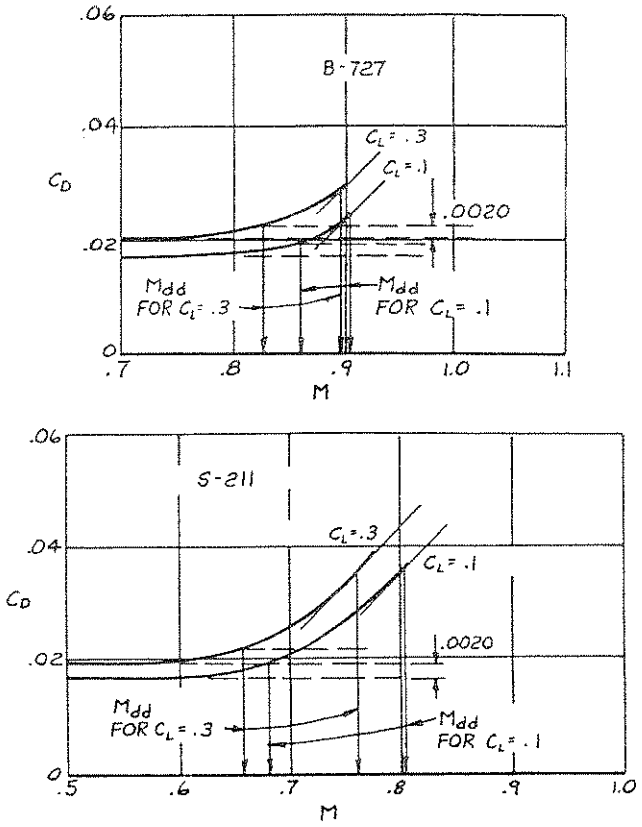

Figure 5.4 Illustration of Drag Rise with Mach Number and Definition of Drag Divergence

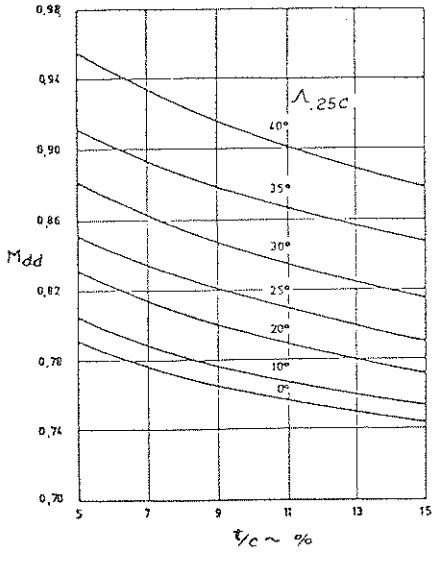

Figure 5.5 Effect of Wing Sweep and Wing Thickness on M_{dd} for $C_L = .3$ (Valid for $A \geq 8.3$)

In Chapter 3 the so-called Critical Mach Number (M_{crit}) was defined as that free stream Mach number for which sonic velocity (M=1) first occurs somewhere on a wing or on a body. Of more interest in airplane performance calculations is the so-called Drag Divergence Mach Number (M_{dd}). There are two definitions in use in industry to define M_{dd} for an airplane, similar to the definitions used for an airfoil:

a) Boeing Definition
M_{dd} is that Mach number for which the drag due to compressibility first is 20 drag counts ($\Delta C_D = .0020$) above the incompressible drag level.

b) Douglas Definition
M_{dd} is that Mach number for which the slope $\partial C_D/\partial M$ first reaches the value .10.

Fig. 5.4 illustrates both definitions. In practice these definitions result in M_{dd}-values which are very close to each other.

As may be seen from Fig. 5.4, the value of M_{dd} depends on the lift-coefficient. As was already pointed out in Chapter 4, M_{crit} (and therefore also M_{dd}) depends also on wing sweep angle and wing thickness. Fig. 5.5 illustrates the sensitivity of M_{dd} to both parameters.

It has also been pointed out in Chapter 4 that at high Mach numbers the occurrence of shock waves and shock induced separation will cause changes in lift-behavior. In fact, if M gets too high, the phenomenon of buffet occurs. At the buffet boundary, lift behaves in an oscillatory manner. This can cause severe stability and control problems. The reader may appreciate therefore that there will be an important inter-relationship between drag, lift and Mach Number. A good illustration of this important relationship is given in Fig. 5.6.

For airplanes at supersonic speeds, the drag behavior is also strongly dependent on Mach number and on the lift coefficient. Fig. 5.7 illustrates the drag characteristics of an early supersonic fighter airplane. For such airplanes, the drag polar is sometimes represented by:

$$C_D = C_{D_o} + kC_L^2 \qquad (5.4)$$

Fig. 5.8 illustrates C_{D_o}, k and C_{L_α} for the airplane of Fig. 5.7.

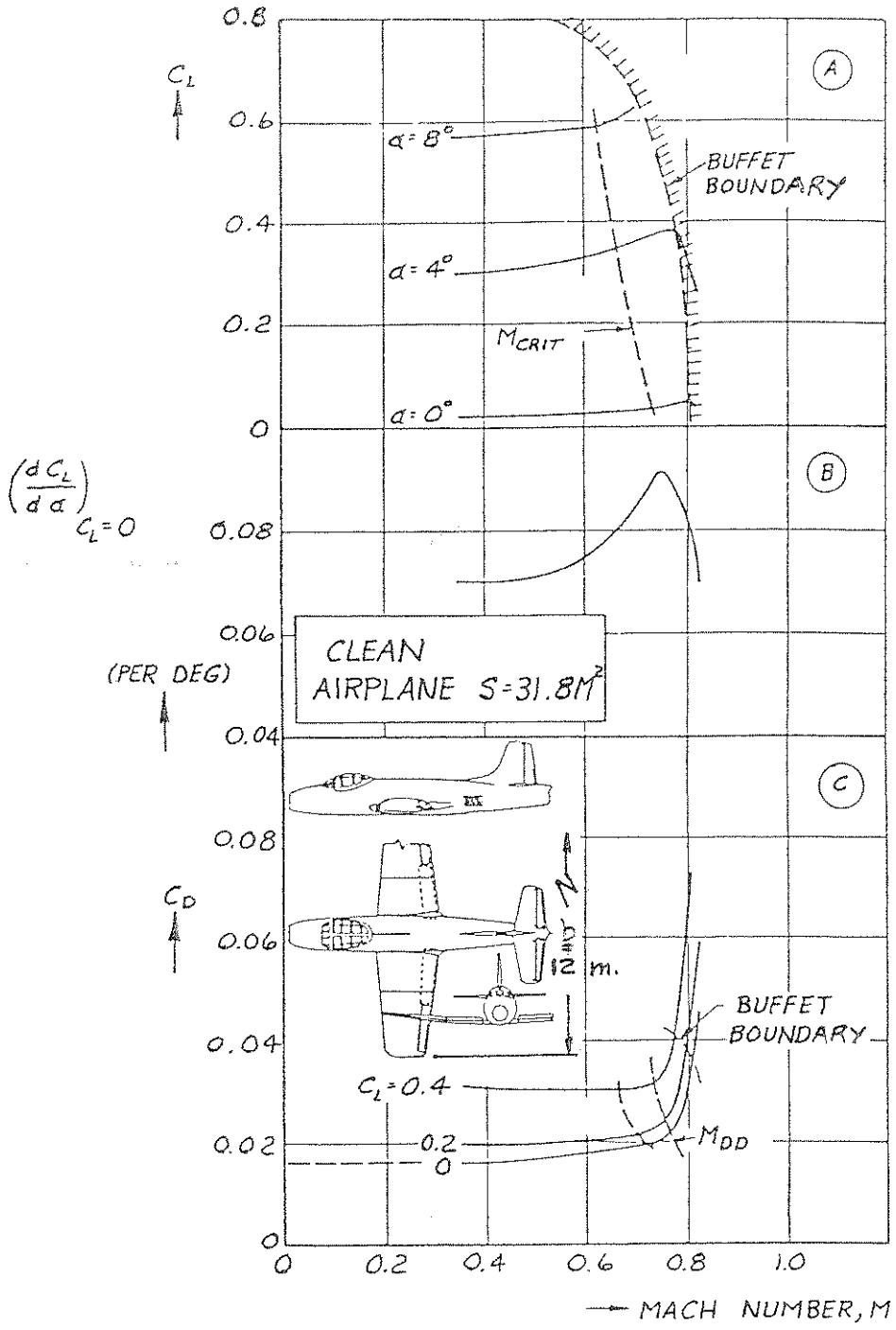

Figure 5.6 Relation Between Lift, Drag and Mach Number for a Jet Trainer (Fokker S14)

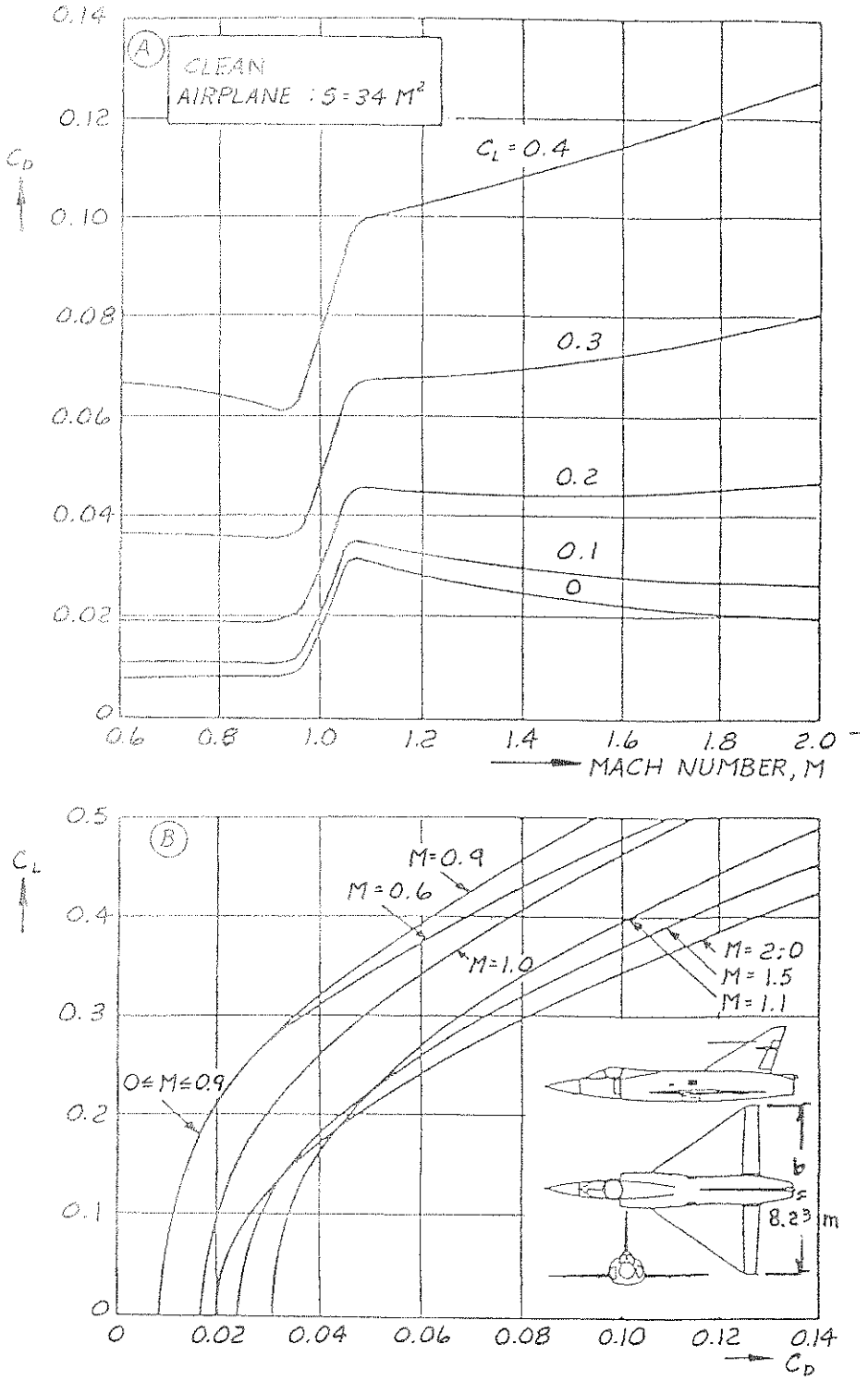

Figure 5.7 Drag Characteristics of an Early Supersonic Fighter Airplane

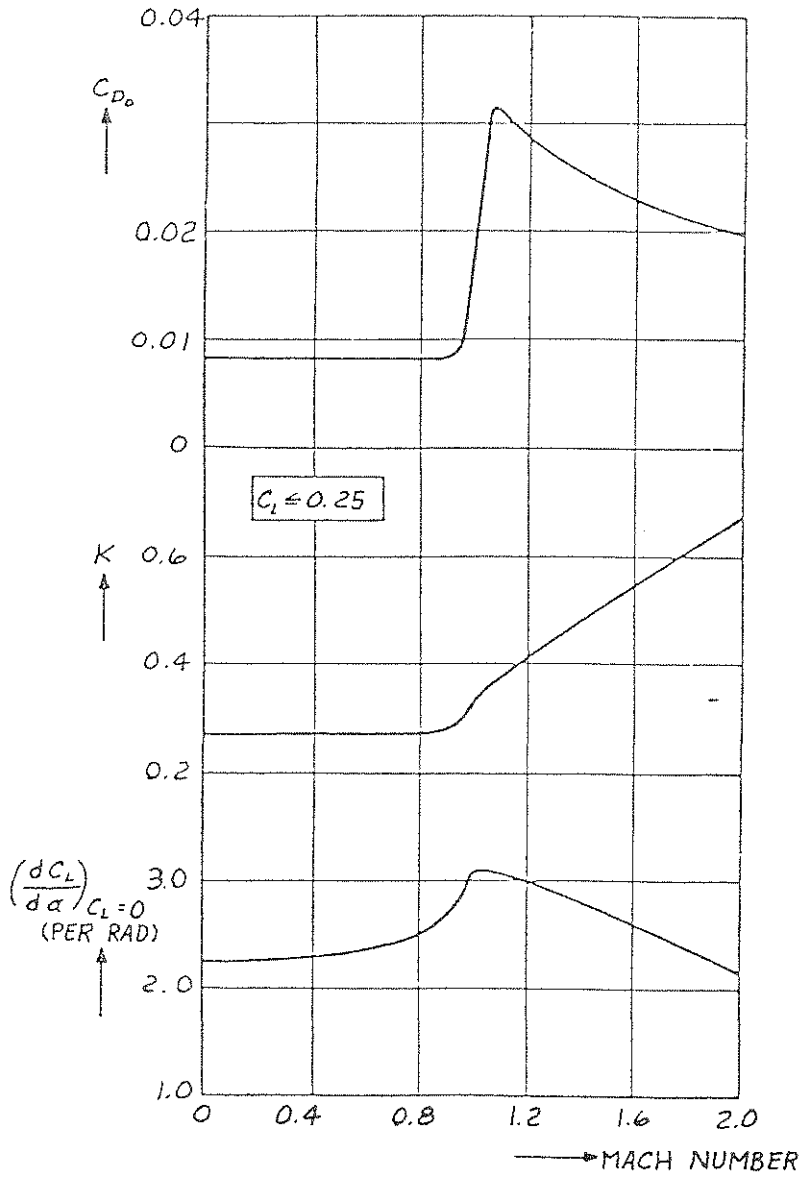

Figure 5.8 Values of C_{D_o}, k and $\left(\frac{dC_L}{d\alpha}\right)_{C_L=0}$ for the Airplane of Fig. 5.7

5.1.2 EFFECT OF FLAPS, SPEEDBRAKES AND LANDING GEAR

Whenever the airplane configuration is changed by extending flaps, speedbrakes or landing gear, the drag characteristics can change drastically. An example is shown in Fig. 5.9.

5.2 DISCUSSION OF IMPORTANT DRAG CONTRIBUTIONS

For purposes of understanding the origins and build-up of drag of airplanes, the drag polar is sometimes split into the following components:

- parasite drag (i.e. all drag which is not dependent on the production of lift)
- induced drag (i.e. all drag which is directly dependent on the production of lift.

In the case of Eqns. (5.1) and (5.3) it would follow that C_{D_o} and $C_{D_{min}}$ are in fact parasite drag coefficients while the remaining terms are induced drag. In reality, it is difficult to achieve a 'pure' split of drag into these simple categories. The reason is that in many airplanes the parasite drag can become dependent on lift also.

The reader should realize that any drag build-up method is somehow arbitrary and constitutes only a (hopefully) consistent method of bookkeeping of drag contributions. Most airplane manufacturers have developed their own (usually proprietary) methods of bookkeeping.

To help the reader understand the basics of drag component and source build-up, the following equation will be used.

$$C_D = (C_{D_{o\ W}}) + (C_{D_{o\ B/N/T}}) + (C_{D_{o\ V}}) + (C_{D_{o\ H}}) + (C_{D_{i\ WB}}) + \Delta C_{D_{misc}} + \Delta C_{D_M} + \Delta C_{D_{trim}} \qquad (5.5)$$

where: $(C_{D_{o\ W}})$ = zero lift drag coefficient of a wing

$(C_{D_{o\ B/N/T}})$ = zero lift drag coefficient of a body (fuselage, nacelle, tiptank)

$(C_{D_{o\ V}})$ = zero lift drag coefficient of (a) vertical tail(s).

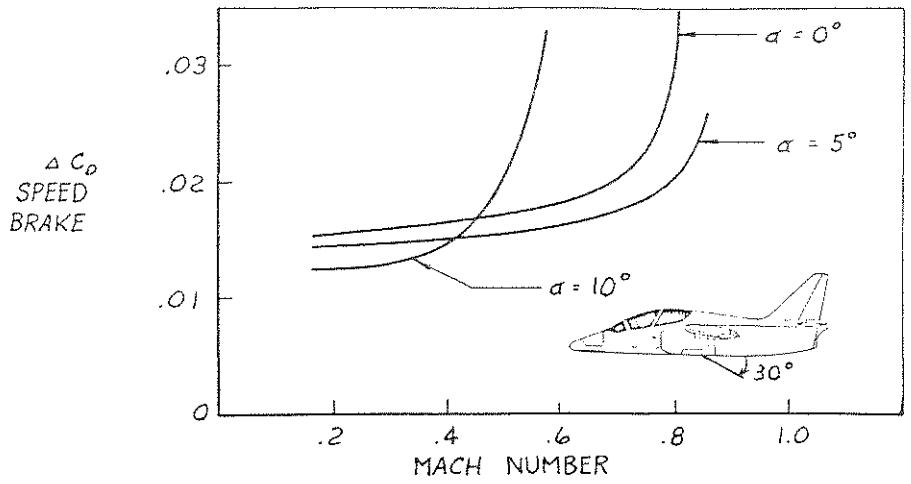

a) SPEED BRAKE DRAG INCREMENT

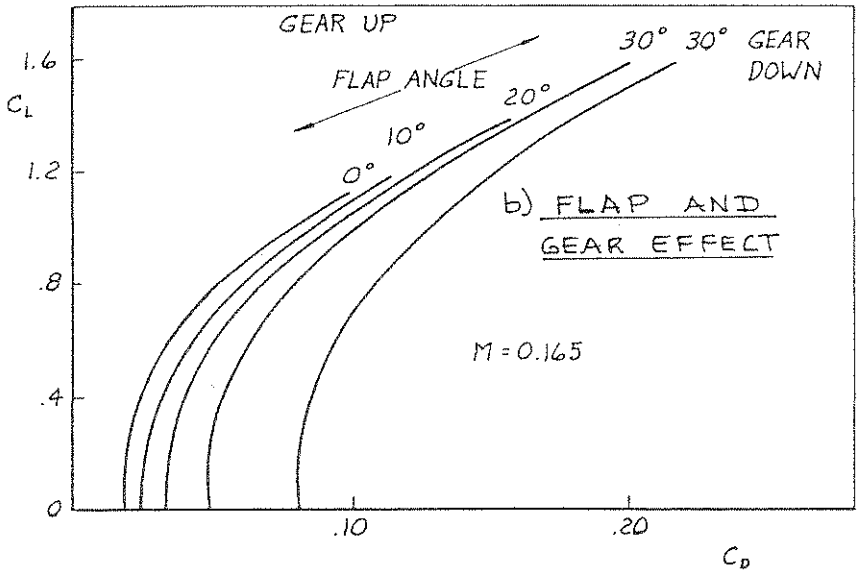

Figure 5.9 Effect of Flaps, Speedbrake and Landing Gear on the Drag Polar of a Small Jet Trainer

$(C_{D_{o\,H}})$ = zero lift drag coefficient of a horizontal tail

$(C_{D_{i\,WB}})$ = induced drag coefficient of a wing-body combination

$\Delta C_{D_{MISC}}$ = incremental drag coefficient due to miscellaneous causes. Typical contributors are:

- flaps
- landing gear
- windshield
- cooling drag
- interference drag
- speed brakes
- antennas and other protuberances
- miscellaneous roughnesses and holes

ΔC_{D_M} = incremental drag coefficient due to compressibility

$\Delta C_{D_{TRIM}}$ = incremental drag coefficient due to trim requirements

It should be obvious that if an airplane also has other surfaces (such as for example a canard surface) their drag contribution is added to Eqn. (5.5).

Fig. 5.10 illustrates a typical drag breakdown for a number of airplanes. The figure suggests that currently used drag prediction methods fall short of their mark in the case of light propeller driven airplanes. In the case of business jets the methods do a lot better. It is also well known that the major jet transport manufacturers manage to predict drag very accurately.

5.2.1 WING AND TAIL DRAG, $(C_{D_o})_W$, $(C_{D_o})_V$, $(C_{D_o})_H$

The drag contributions $(C_{D_{o\,W}})$, $(C_{D_{o\,V}})$ and $(C_{D_{o\,H}})$ are generally caused by two effects:

- profile or thickness drag
- friction drag

The wing profile or pressure drag depends on the pressure distribution along the wing surface and the amount of flow separation near the trailing edge. On the other hand, the pressure distribution depends on camber, on airfoil thickness ratio and on the location of maximum thickness. In general, the profile drag will be increased if the maximum thickness is located closer to the leading edge. This is

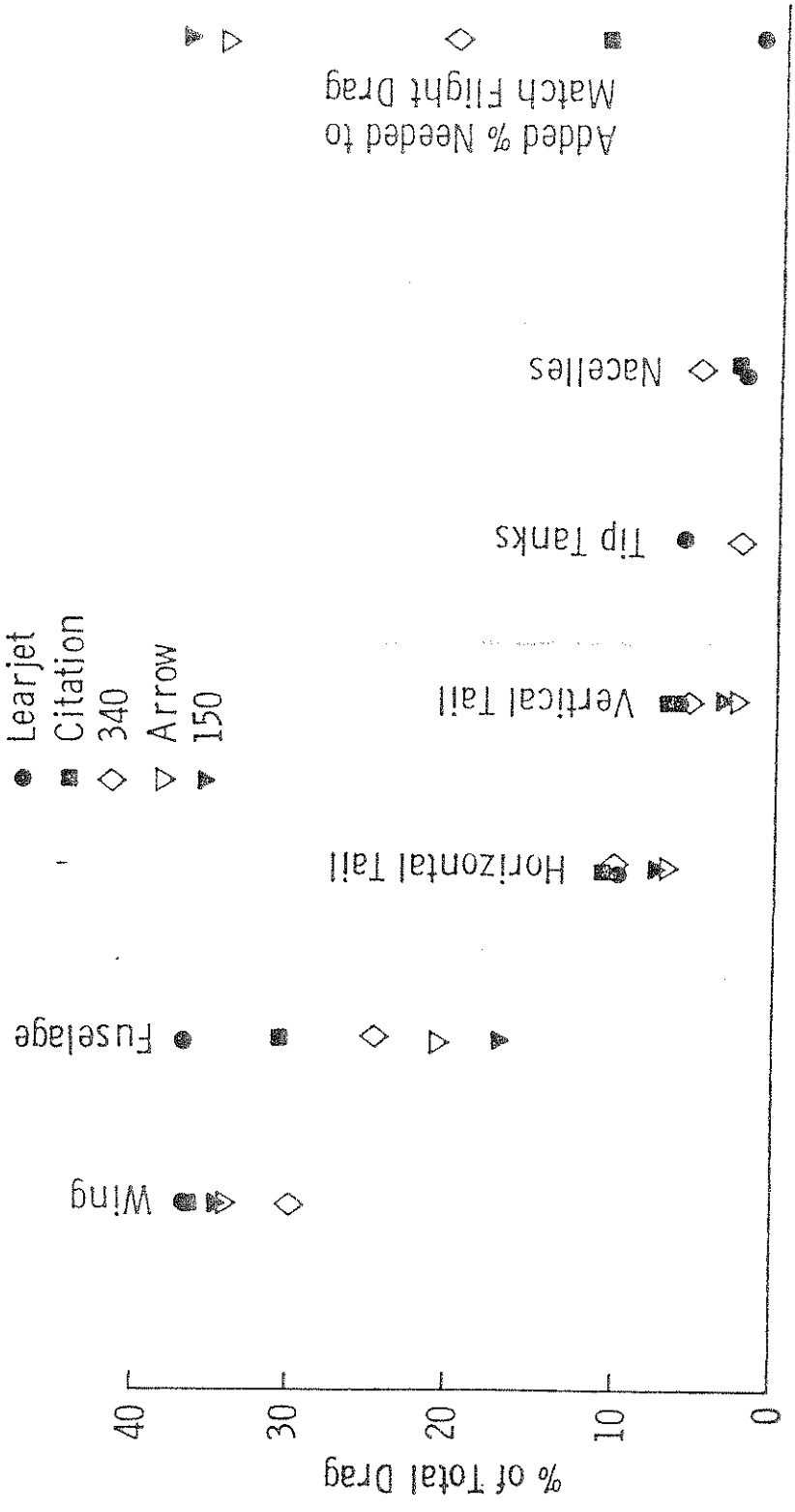

Figure 5.10 Examples of Predicted Drag Breakdown (Taken From Ref. 5.3)

because a larger portion of the airfoil surface will be covered with a turbulent boundary layer and will be subject to an adverse pressure gradient.

The wing friction drag depends on the wing 'wetted area' (= area directly exposed to airflow) and on the boundary layer (the latter can be laminar and/or turbulent according to Chapter 3 depending on Reynolds number). The friction drag coefficient of a wing is often taken to be that for turbulent flow and is referred to that of an equivalent flat plate using Fig. 5.11. It is seen that Mach number also has an effect on skin friction drag.*

Skin friction drag of a wing can be calculated as follows:

$$(C_{D_o})_W = C_{f_w} \frac{S_{wet}}{S_{ref}} \qquad (5.6)$$

Friction only

where C_{f_w} follows from Fig. 5.11** and S_{wet} depends on planform area and on airfoil thickness. Note that Fig. 5.11 is for smooth surfaces only. For rough surfaces, the Reynolds number to be used in Fig. 5.11 may be different from the calculated value. For more detail, see Ref. 5.1.

- The following empirical equation is often used to calculate total wing zero-lift drag (profile and friction):

$$(C_{D_o})_W = C_{f_w} \left[1 + L\left(\frac{t}{c}\right) + 100\left(\frac{t}{c}\right)^4\right] R_{LS} \frac{S_{wet}}{S_{ref}} \qquad (5.7)$$

where: $L = 1.2$ for $\left(\frac{t}{c}\right)_{max}$ located at $x_t > .30c$, where x_t is the maximum thickness location.

$L = 2.0$ for $\left(\frac{t}{c}\right)_{max}$ located at $x_t < .30$

R_{LS} is defined in Fig. 5.12 and accounts for the increased Reynolds number length due to spanwise flow on a lifting surface.

---

* It is noted that Fig. 5.11 was prepared by converting incompressible results into compressible values through Eckert's method (Ref. 5.4). The necessary physical quantities, such as density and viscosity, are evaluated at a chosen reference temperature given by Eckert.

** To find the wing Reynolds number it is generally assumed that the characteristic length of the wing is the mean aerodynamic chord of the exposed wing.

$$c_f = \frac{0.455}{(\log_{10} {}^*R_N)^{2.58} * (1+0.144M^2)^{0.58}}$$

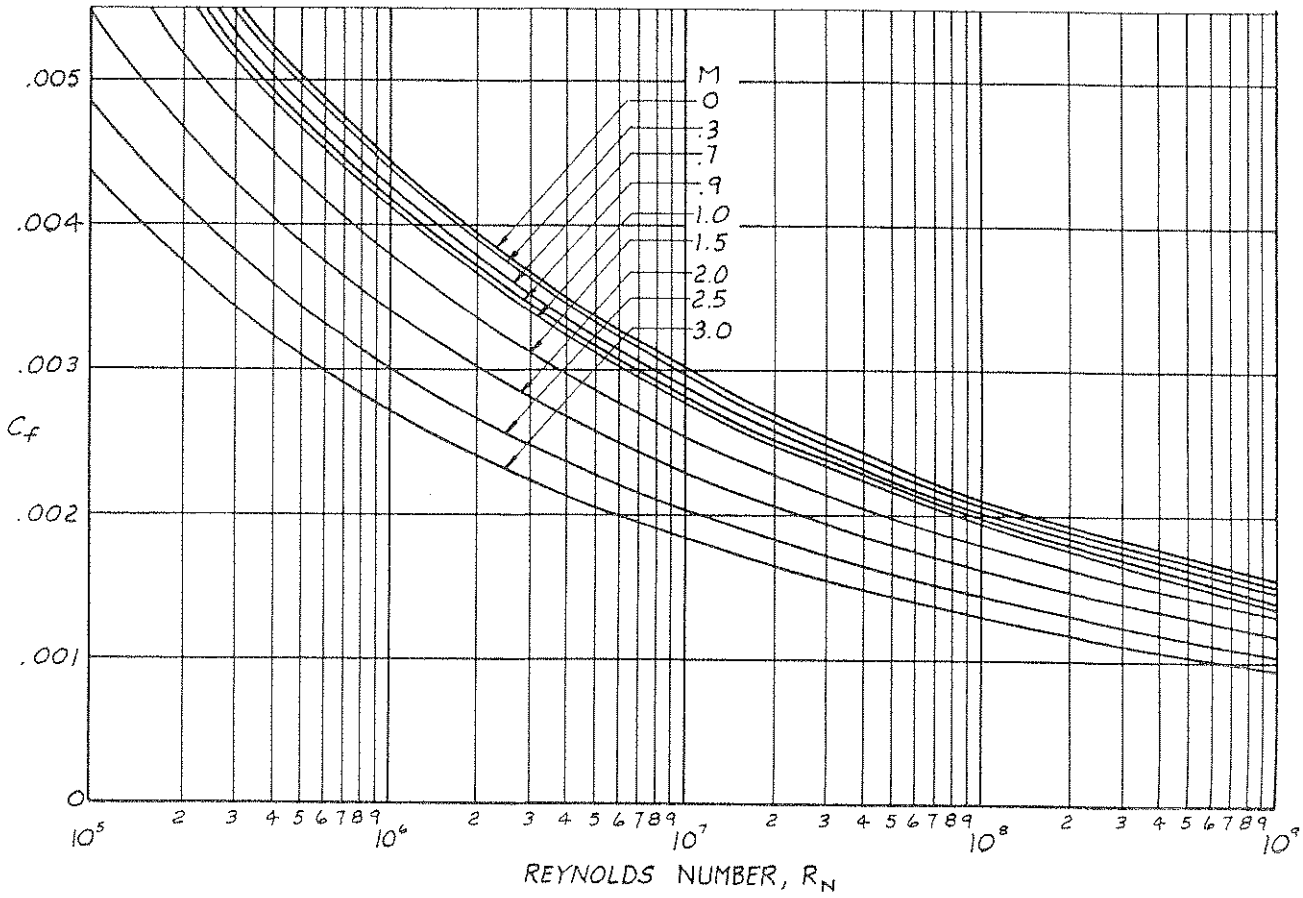

Figure 5.11 Turbulent Mean Skin-Friction Coefficient on an Insulated Flat Plate

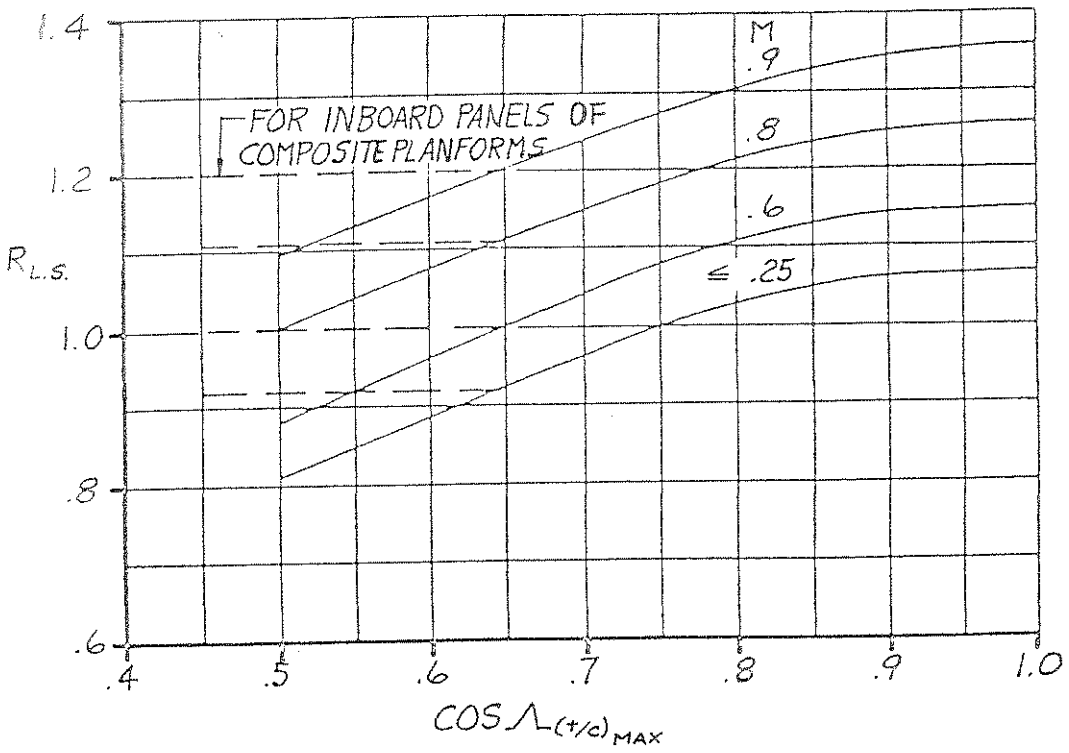

Figure 5.12 Lifting-Surface Correlation Factor (Taken From Ref. 5.1)

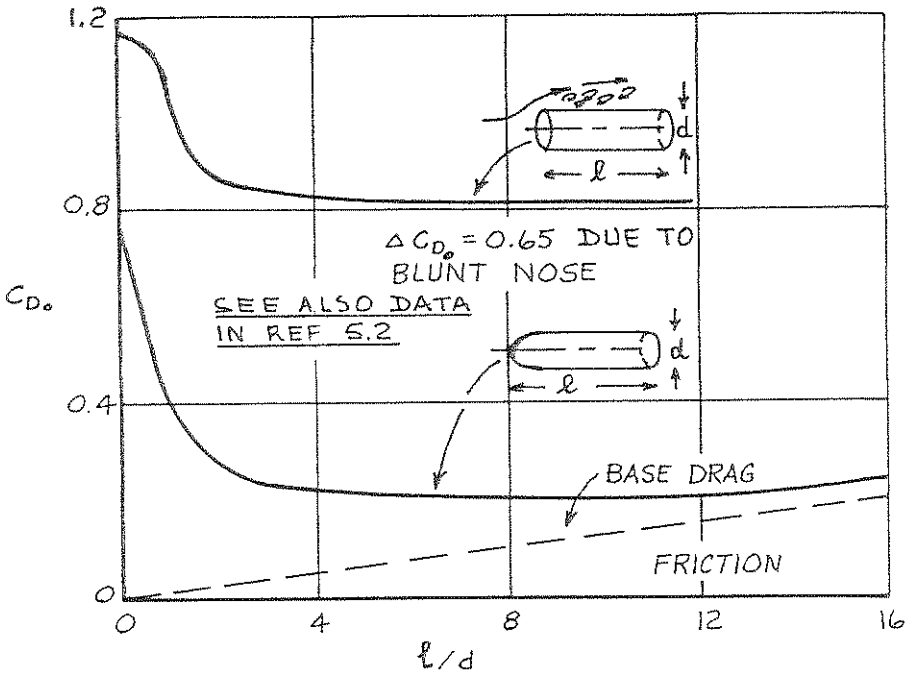

Figure 5.13 Example of Base Drag Coefficients

C_{f_w} is obtained from Figure 5.11.

For a wing with given planform area S_{plf}, the wetted area can be calculated by accounting for the effect of airfoil thickness. Corning (Ref. 5.5) presented a graphical relation for the airfoil surface area as a function of thickness ratio by examining NACA 65-series airfoils. This relation can be used to calculate the wetted area.

$$S_{wet} = K\, S_{plf} \tag{5.8}$$

where the so-called surface area factor (K) can be obtained as:

$$\begin{aligned} K &= 1.9767 + 0.5333\,(\tfrac{t}{c}), && \tfrac{t}{c} \geq 0.05 \\ &= 2.0 && , \tfrac{t}{c} < 0.05 \end{aligned} \tag{5.9}$$

Note that if t/c is not a constant for a wing, an average value may be used in Eqn. (5.9).

Values for $(C_{D_o})_H$ and $(C_{D_o})_V$ can also be computed with Eqn. (5.7).

As expected, wing and tail drag increase in proportion to the wetted area. Airplane cruise drag can thus be minimized by minimizing these areas.

5.2.2 BODY DRAG, $(C_{D_o})_B$

On a given body, such as a fuselage, the relative proportions of form drag and skin friction drag depend on the shape of the body.

Those bodies that have predominantly form drag are referred to as bluff bodies. A thin flat plate set normal to the freestream would have 'pure' form drag.

Those bodies that have predominantly skin friction drag are called streamlined bodies. A thin flat plate set parallel to the freestream would have 'pure' skin friction drag.

For a body of revolution, the main shape parameter is the ratio of length to maximum diameter -- called fineness ratio, ℓ/d. For large fineness ratios, the form drag is reduced, but the skin friction drag is increased because of the large exposed surface. The converse is true for small fineness ratios. The following empirical formula for calculating the zero lift drag of a body illustrates this point (Ref. 5.6):

$$C_{D_{o(B)}} = C_{f_B}\left[1 + \frac{60}{(\ell/d)^3} + 0.0025\,(\frac{\ell}{d})\right]\frac{S_{wet\ body}}{S_{ref}} \qquad (5.10)$$

where C_f is the skin-friction coefficient discussed in Section 5.2.1. Values for C_f can be determined from Fig. 5.11 for turbulent boundary layers. Typical fuselage fineness ratios for current general aviation airplanes are shown in Table 5.1. Note that S_{ref} is normally taken to be the wing planform area.

If a body or a fuselage is not properly streamlined, flow separation may occur. This can create the equivalent of a 'base' area which causes so-called 'base drag' in addition to the drag expressed by Eqn. (5.10). The base drag coefficient can be computed from Ref. 5.6 (p.34). Examples of base drag coefficients are shown in Figure 5.13.

In the design of a fuselage it is advisable not to exceed about 12° - 15° contour changes in the transition from center-fuselage to aft-fuselage. Some examples of fuselage configurations are shown in Fig. 5.14.

5.2.3 WING-BODY INDUCED DRAG, $(C_{D_{i\ WB}})$

The induced drag of an airplane is mainly contributed by the wing as discussed in Chapter 4. A small part is from the horizontal tail in the form of trim drag (see section 5.2.6). For a complete airplane configuration, several factors which affect the induced drag of a wing will be discussed below.

(a) Plan form shape. As indicated in Chapter 4, the minimum induced drag for a moderate or high aspect-ratio wing may be realized by using an elliptical planform. For a rectangular planform, the additional induced drag may be approximated by (Ref. 5.2, Chapter 7):

$$\Delta\left(\frac{dC_{D_i}}{dC_L^2}\right) \approx 0.003 \qquad (5.11)$$

Using Eqn. (4.24), Eqn. (5.11) implies that:

$$\Delta\left(\frac{1}{e}\right) \approx (0.003)\pi A \qquad (5.12)$$

For a tapered wing, the additional induced drag will be minimum for taper ratios in the range of 0.3 to 0.4 and can be estimated as 1 or 2% of the elliptical induced drag.

Table 5.1 Examples of Fuselage Fineness Ratios and Wetted Areas for General Aviation Aircraft

Type	$\frac{\ell_B}{d}$	S_{REF} (FT^2)	$S_{wet\ body}$ (FT^2)	$\frac{S_{wet\ body}}{S_{REF}}$
Cessna 210	5.02	175	319	1.82
Cessna 207	5.69	174	425	2.44
Beech Sierra	5.22	146	332	2.27
Cessna 185	5.15	176	292	1.66
Beech Bonanza ('58)	4.98	181	323	1.78
Beech Baron	5.69	199.2	362	1.82
Piper Navajo	5.97	229	502	2.19
Cessna 310	5.40	179	306	1.71
Piper Seneca	5.68	206.5	356	1.72
Beech Duke	5.59	212.9	586	2.28
Cessna 414	5.52	195.7	488	2.49
Beech King Air	6.06	294	652	2.22
Gates Learjet 24	8.8	232	502	2.16

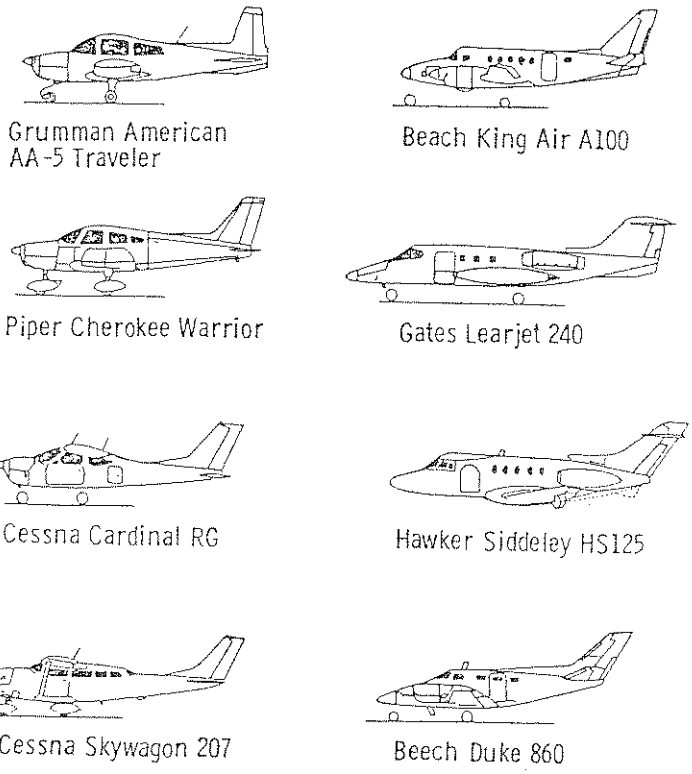

Figure 5.14 Typical General Aviation Fuselages

(b) Tip Shape. Tip vortices may roll up and get around the lateral edges of a wing to reduce the effective span of the wing. This is illustrated in Fig. 5.15. Experiments show that wings with square or sharp tips have the widest effective spans. When tip tanks are used, favorable effects can be derived from increased span and area of the wing and the endplate effects. However, the tip vortices will move slightly inboard to reduce the effective span. Hence, half of the tip tank diameter, at each wing tip, may be assumed ineffective with respect to the aerodynamic span.

(c) Twist. Washout of the wing changes the lift distribution, particularly at low C_L. The additional induced drag has been found to be proportional to the square of the amount of twist. (Ref. 5.2, p. 7-7)

(d) Sweep. For swept-back wings, lift is more concentrated near the wing tips. By decreasing the taper ratio, the lift concentration near the tip can be reduced. However, small taper-ratio wings are very susceptible to tip stalling. Therefore, swept-back wings with realistic taper ratios do not have a lift distribution of elliptical shape, so that the induced drag will be increased. Experiments indicate that:

$$\frac{dC_{D_i}}{dC_L^2} \approx \frac{1}{\cos\Lambda_{c/4}} \tag{5.13}$$

(e) Tandem configuration. Wing theory shows that the induced drag of a tandem configuration is equal to that of a single wing having the combined lift distribution. This follows from Munk's Stagger Theorem (Ref. 5.7). Depending on the longitudinal stability of the airplane, the tail or the canard may carry an upload or a download. The resulting additional induced drag may be appreciable, as discussed in Section 5.2.6.

(f) Winglets. Winglets are small, nearly vertical aerodynamic surfaces mounted rearward above the wing tips. Examples of their arrangement are shown in Figure 5.16 for a Boeing KC-135A, in Figure 5.17 for a Beech Bonanza, and in Figure 5.18 for a Learjet model 55.

Winglets are placed rearward to avoid the increased velocities over the inner surface of winglets being superimposed on the high velocities over the forward region of the wing upper surface. Therefore, increase in transonic compressibility effects can be minimized.

Furthermore, the winglets operate in the circulation flow field around the wing tip. This wing tip circulation flow tends to produce large sidewash (toward inboard) on the winglet even at low airplane

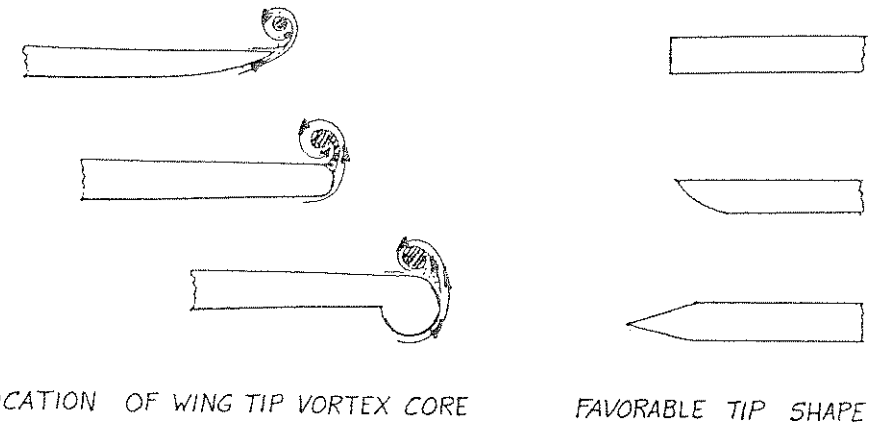

Figure 5.15 Various Tip Shapes and Their Effect on Location of Tip Vortex Core (Ref. 5.2)

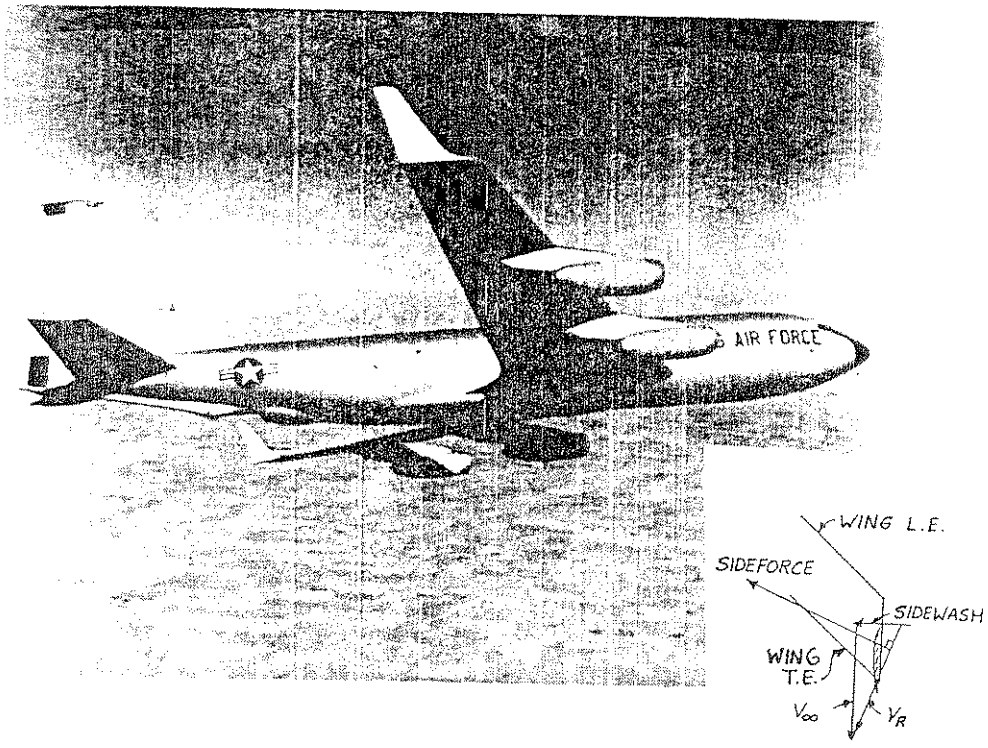

Figure 5.16 USAF KC-135A With NASA Winglets

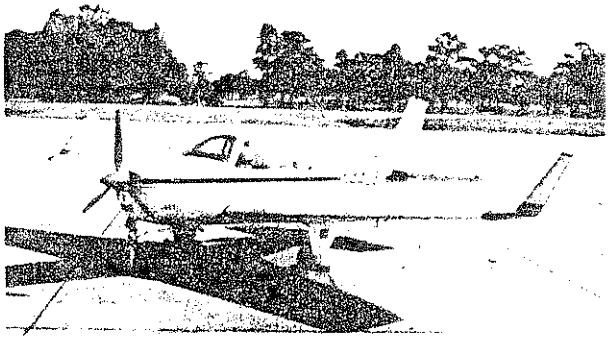

Figure 5.17 Beech Bonanza With Winglets

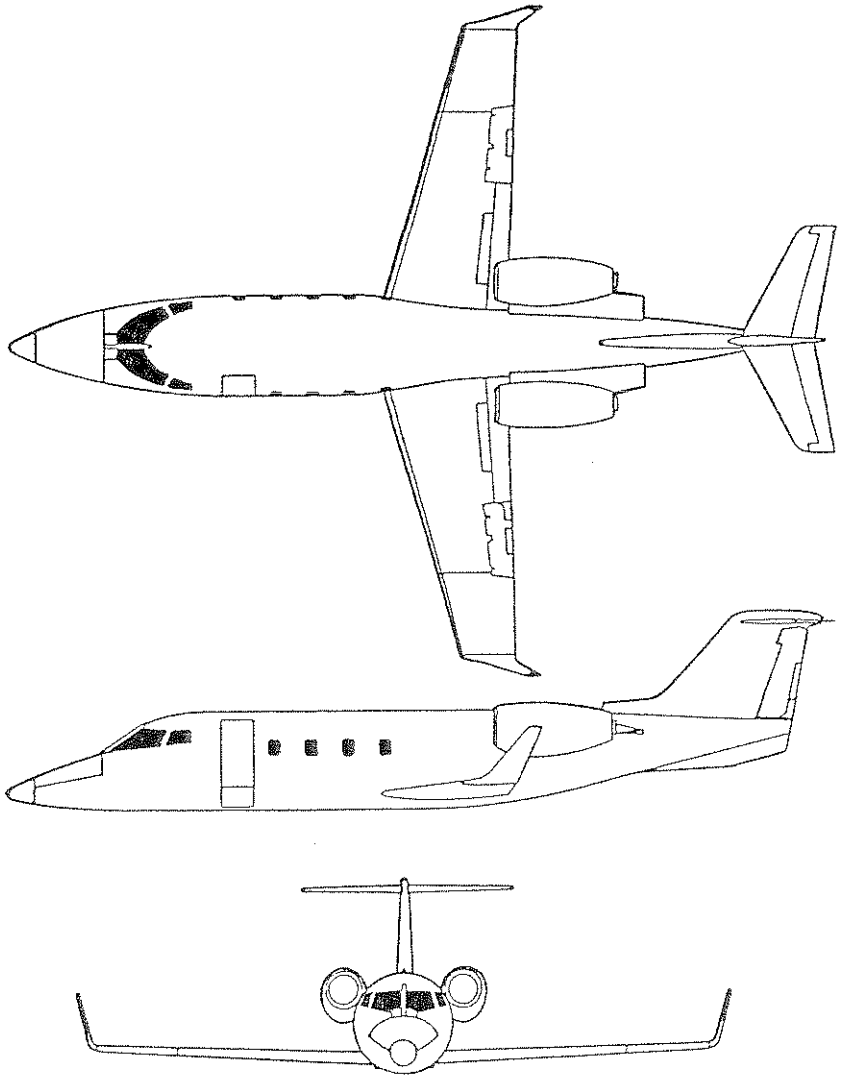

Figure 5.18 Learjet Model 55 With Winglets

angles of attack. Since the resultant side force is approximately perpendicular to the local flow, it produces a forward thrust component to reduce the airplane induced drag. This situation is indicated in Figure 5.16.* The magnitude of thrust produced depends on the strength of wing tip circulation which in turn is a function of the rate of change in wing tip loading.

Note that as indicated in Chapter 4, the induced drag can also be reduced by using high aspect-ratio wings which can be obtained by extending the wing tips. The aerodynamic gain in the percentage increase in lift-drag ratio for winglets and for wing tip extensions is illustrated in Figure 5.19 (Ref. 5.8). It is seen that at the cruise Mach numbers (indicated by tick marks), the winglets produce about an 8 percent improvement in L/D for the KC-135A, about a 4 percent improvement for both L-1011 and DC-10. About 6.5 percent improvement is realized for a proposed high aspect-ratio supercritical wing (A = 9.8) model. The wing tip extension is made to produce the same root bending moment at cruise C_L. It is seen that in these cases except the proposed high aspect-ratio supercritical wing, the performance gain by wing tip extension is less than that by winglets.

Figure 5.20 shows the benefit of winglets installed on a Beech Bonanza. Whether or not winglets are helpful depends apparently on the configuration and mission phase of an airplane.

Additional information about winglets can be found in Refs. 5.9 and 5.10.

5.2.4 MISCELLANEOUS DRAG, $(\Delta C_D)_{MISC}$

Several additional contributions to the total drag must also be considered. They include:

5.2.4.1 Drag Due to Flaps
5.2.4.2 Drag Due to Landing Gear
5.2.4.3 Drag Due to Windshields and Canopies
5.2.4.4 Drag Due to Nacelles
5.2.4.5 Drag Due to Speed Brakes
5.2.4.6 Cooling Drag
5.2.4.7 Drag Due to Miscellaneous Roughnesses and Protuberances
5.2.4.8 Interference Drag

Details are discussed below. General methods for calculating these components of drag can be found in Refs. 5.2, 5.6 and 5.11.

---

* The winglet works very much like a sailboat 'tacking' into the wind!

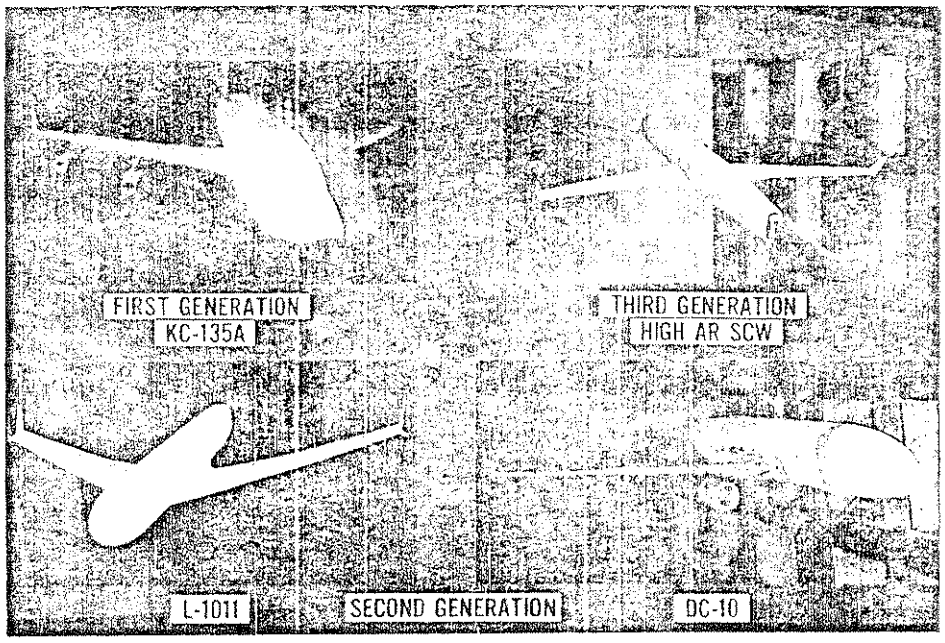

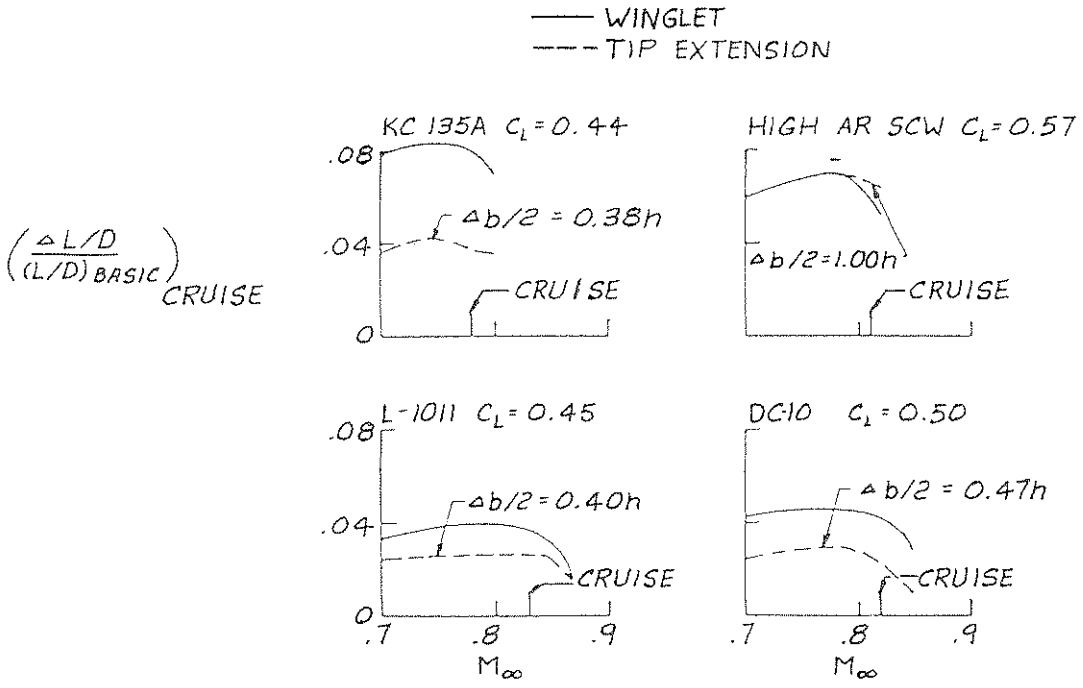

Note. h = Winglet span

Figure 5.19 Winglet and Tip Extension Performance (Ref. 5.8)

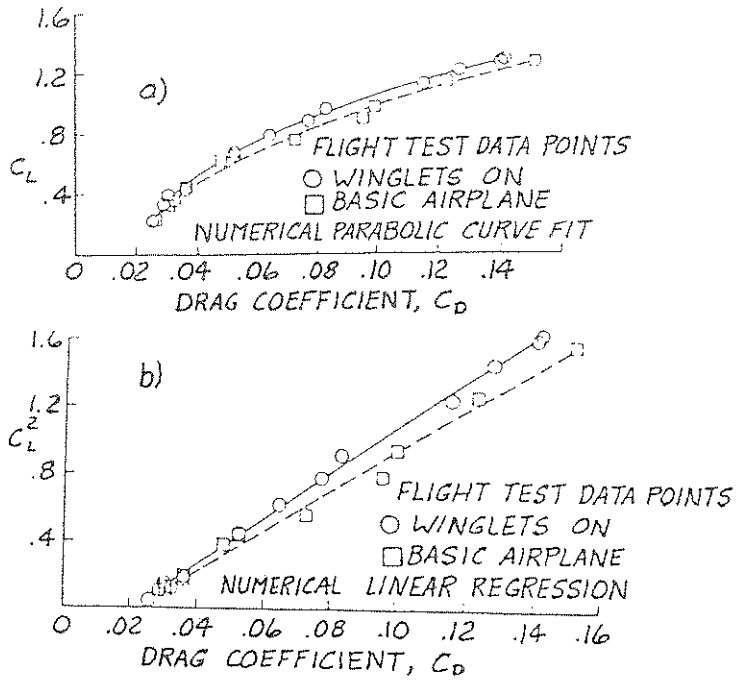

Figure 5.20 Benefit of Winglets on a Beech Bonanza (Ref. 5.10)

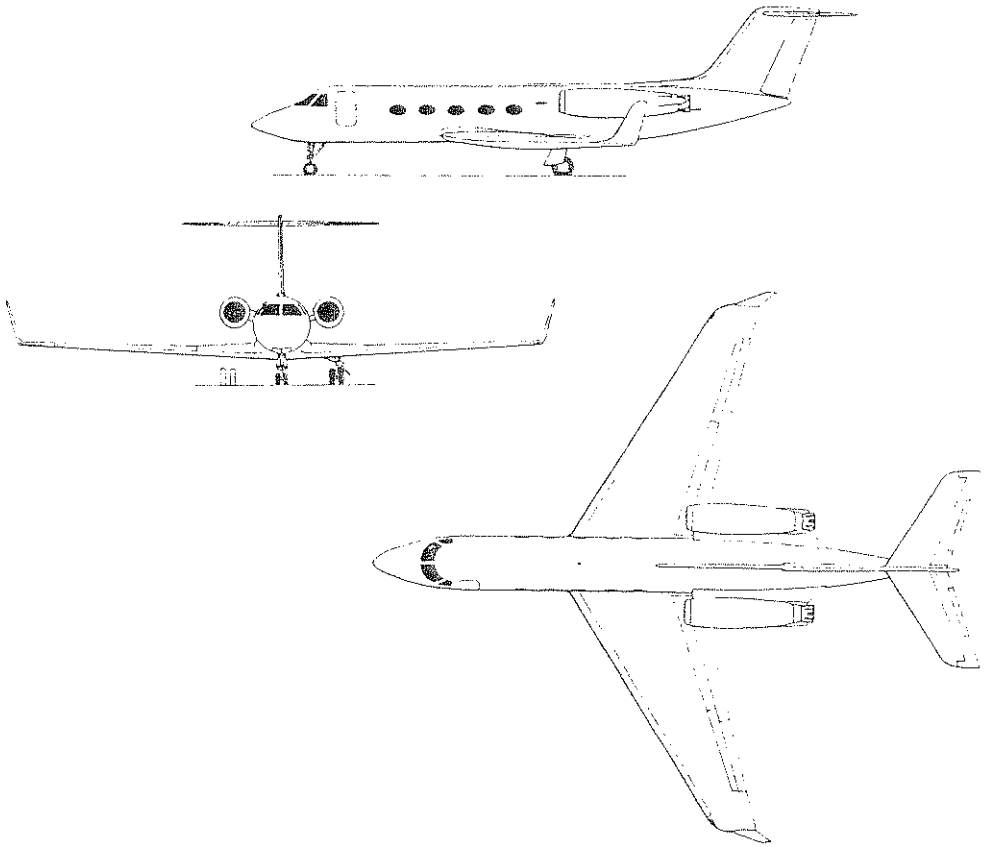

5.2.4.1 Drag Due to Flaps

This drag increment results from an increase in parasite drag (ΔC_{D_P}), induced drag (ΔC_{D_i}) and interference drag ($\Delta C_{D_{INT}}$). That is,

$$\Delta C_D(\text{flaps}) = \Delta C_{D_P} + \Delta C_{D_i} + \Delta C_{D_{INT}} \tag{5.14}$$

Calculation of ΔC_{D_P}:

The flow field associated with either trailing-edge or leading-edge high lift devices is difficult to calculate. If the two dimensional profile drag increment (Δc_{d_p}) due to flaps is known, the corresponding three-dimensional increment can be calculated as:

$$\Delta C_{D_P} = \Delta c_{d_p} \left(\frac{S_{w_f}}{S_{ref}}\right) \cos\Lambda_{c/4} \tag{5.15}$$

where S_{w_f} is the wing area affected by the flap. Data for estimating Δc_{d_p} due to flaps can be found in Ref. 5.1 and 5.2.

Calculation of ΔC_{D_i}:

Deflection of partial span flaps changes the shape of the span loading distribution. The additional induced drag is a function of the incremental lift coefficient or flap angle. In addition, the distribution of zero-lift angle would be changed due to flap deflection. Hence, the additional induced drag will have a component proportional to the square of incremental lift coefficient or flap angle, similar to the twist effect. It can be calculated by using the lifting-surface theories referred to in Chapter 4.

According to Ref. 5.6, ΔC_{D_i} can be calculated empirically as:

$$\Delta C_{D_i} = K^2(\Delta C_L)^2 \cos\Lambda_{c/4} \tag{5.16}$$

where K is an empirical factor given in Ref. 5.6 and ΔC_L is the incremental lift coefficient due to flaps at a given angle of attack.

Calculation of $\Delta C_{D_{INT}}$

The interference drag results from the complicated three-dimensional flow field due to flaps and its interference with neighboring lifting surfaces. It can be estimated as (Ref. 5.6, p. 3.35):

$$\Delta C_{D_{INT}} = -0.15\Delta C_{D_p} \quad \text{(split flaps)} \tag{5.17}$$

$$\Delta C_{D_{INT}} = +0.40\Delta C_{D_p} \quad \text{(slotted flaps)} \tag{5.18}$$

An example of the effect of flaps on drag is shown in Figures 5.9 and 9.11.

5.2.4.2 Drag Due to Landing Gears

Landing gears produce drag during take-off and landing for retractable gears and in all flight operations for nonretractable gears. Its magnitude is proportional to the frontal area (i.e. tire width times outer diameter), and also depends on the airplane lift coefficient. Refs. 5.2 and 5.6 can be used to estimate the parasite drag of wheels, struts, cavities, doors, etc.

It should be noted that the drag increment may vary with flap deflection, as a result from the downwash field induced by the flaps. Fig. 5.21 shows the trend for the DC-8 (ref. 5.12). Another example of landing gear drag is shown in Fig. 9.11.

5.2.4.3 Drag Due to Windshields and Canopies

The drag increment due to windshields and canopies depends on the streamwise shape, cross-sectional shape, fineness ratio (length divided by height for canopies), and Mach number. Reference 5.6 presents some design data for estimation and should be consulted.

The different windshield and canopy shapes of Fig. 5.14 suggest that there is no unanimity on the "best" shape for these items!

5.2.4.4 Drag Due to Nacelles

The incremental drag due to nacelle (jet or prop) is made up of three components:

1. friction drag
2. profile or pressure drag
3. interference drag

The first two types of drag can be satisfactorily estimated by using the same methods which were used for the fuselage. Note that the

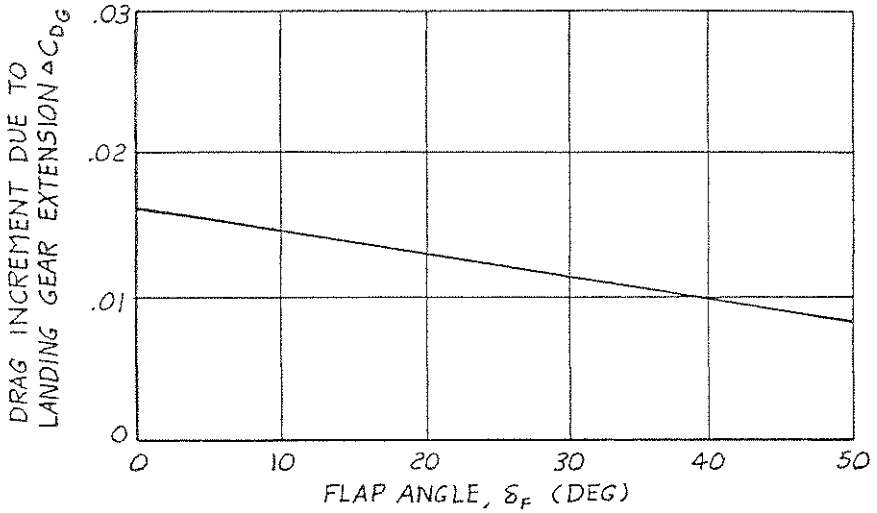

Figure 5.21 Flight Measured Landing Gear Drag Increment for DC8 Jet Transport

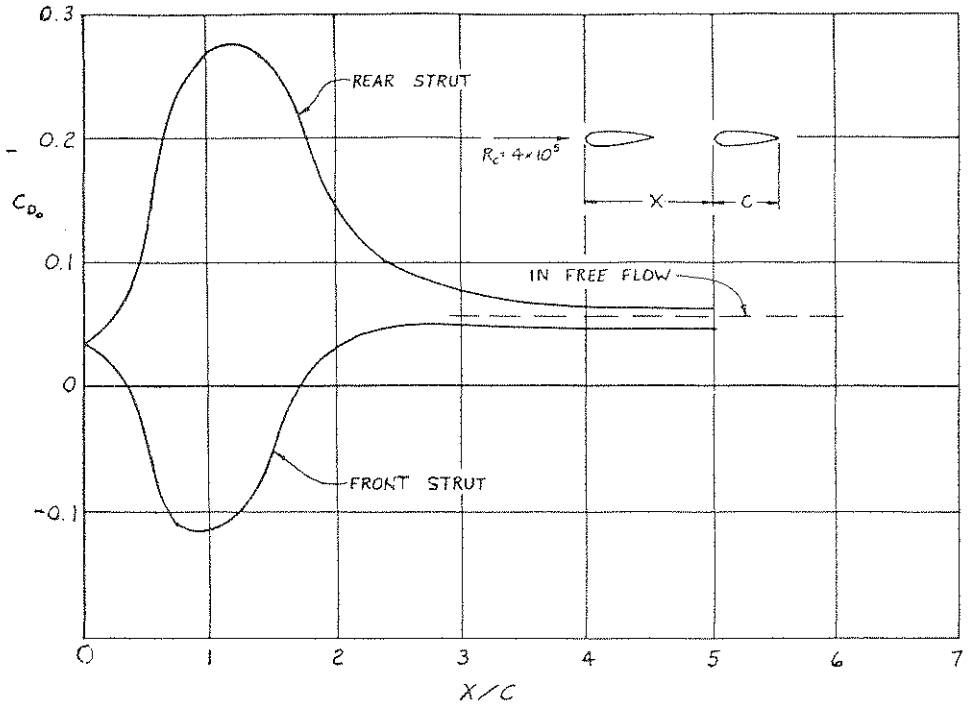

Figure 5.22 Drag of a Pair of Strut Sections in Tandem (Data from Ref. 5.2)

wetted area of the nacelle does not include the internal area, since any drag associated with the internal flow is accounted for in the so-called installed thrust of the engine.

The interference drag consists of two effects:

1. Viscous effects
2. Induced effects

Viscous effects arise from the change in total wetted area when the nacelle is installed. On the other hand, the induced component arises from the change in the flow field when a nacelle is placed close to other airplane components. This will be further explained in Section 5.2.4.7. Ref. 5.6 presents some data for estimating the induced component of the interference drag.

5.2.4.5 Drag Due to Speed Brakes

Speed brakes are used to separate the air flow so as to create drag to reduce airspeed. They are plate-like surfaces deflecting into the air stream from the upper and lower wing surfaces or the fuselage. A flat plate placed normal to the free flow can generate a drag coefficient of 1.2 to 2.0 (Ref. 5.2, pp. 3-16) based on the plate area, depending on the aspect ratio of the plate (higher values are obtained for more two-dimensional configurations). When a plate is attached to airplane components, the incremental drag coefficient depends on also the location of the plate. On the wing surface, the maximum drag coefficient can be produced by placing the brakes near the location of maximum thickness. Various magnitudes of incremental drag coefficient for different speed brake locations can be found in Ref. 5.2, pp. 13-11.

5.2.4.6 Cooling Drag

This incremental drag occurs primarily in air cooled reciprocating engines. It is caused by friction and by momentum losses associated with cooling air being ducted through the nacelle. Ref. 5.13 (p. 263) contains a good discussion of cooling drag. Cooling drag can amount to as much as 15% of the total zero-lift drag, if poor attention is paid to ducting of cooling air.

5.2.4.7 Drag Due to Roughness and Protuberances

This incremental drag depends on the condition of exterior surfaces of the airplane. Its accurate estimation in preliminary design is difficult. Frequently, a flat percentage on top of the overall zero lift drag of the airplane (such as 5% for light airplanes and 2% for jet airplanes) will suffice.

5.2.4.0 Interference Drag

Interference drag arises from changes in the flow pattern that accompanies the placing of two bodies in close proximity. Ref. 5.2 (Chapter 8) presents many examples of mutual interference between components of aircraft.

Basically, when two streamlined bodies are placed side-by-side, the average velocity near the body surface is always increased. The adverse pressure gradient associated with the decrease in velocity on the aft portion of bodies is responsible for a considerable increase in the drag coefficient. If the same streamlined bodies are placed in tandem, the drag of the rear body can be largely increased, because it is immersed in the low-energy wake from the front body, so that the flow will separate from the rear body. Thus, the total drag of the two bodies placed close together will be higher than the sum of the individual drags. An example is shown in Figure 5.22.

In airplane applications, there are occasions in which a small body is attached to a main body, such as fuselage. The small body may be a canopy, a fuel tank or an antenna, etc. In such cases, the interference drag can be reduced if the small body is placed in the region of favorable pressure gradients of the main body. The interference drag originating in wing-fuselage and engine-nacelle configurations consists of two types:

a parasitic type, corresponding to boundary layer and pressure losses, and
an induced type, caused by changes in the lift distribution.

The parasitic interference drag is small with the wing near the nose of the body and the drag reaches a maximum for locations somewhat aft of the maximum dimension of the fuselage. The interference drag is small again for arrangements near the rear end of the fuselage for tail surfaces. Increased thickness of the boundary layer, and hence reduced dynamic pressure, near the end of the fuselage is responsible for the result.

The parasitic (viscous) interference drag of engine nacelles can be explained in the same way. A rough but simple rule at nearly zero lift is that wing-nacelle interference drag is approximately equal to the section drag of a wing area twice as large as the wing portion covered by the nacelle.

Note that in wing-body and wing-nacelle combinations, the total wetted area of the wing is reduced!

The induced interference drag of wing-fuselage and wing-nacelle combinations occurs mainly because of the change in spanwise lift distribution. Because the resulting lift distribution becomes less elliptical, the induced drag is therefore increased.

To reduce the total drag, it is necessary for the designer to find the appropriate geometric layout of all airplane components which will result in minimum interference drag. In addition, the use of properly designed transition sections, known as fairings or fillets, can significantly reduce interference drag.

5.2.5 COMPRESSIBILITY DRAG, ΔC_{D_M}

This drag increment includes the variation of profile drag with Mach number, shock wave drag, and drag from shock-induced separation.

Within a boundary layer, the compressibility effect will increase the temperature. Hence, the density of the air in the boundary layer is reduced, so that the skin friction drag in compressible flow will be lower. However, because of a simultaneous increase in viscosity, the decrease in laminar skin friction drag is to a large degree eliminated. On the other hand, the turbulent skin friction drag has been found to decrease with Mach number in subsonic flow as(Ref. 5.2, pp. 15-9):

$$C_{f_{com}} = C_{f_{inc.}} (1 - 0.09M^2) \tag{5.19}$$

The interference drag of wing-fuselage-nacelle combinations is usually increased due to compressibility, and outweighs the decrease in skin friction drag. One example of compressibility drag variation with Mach number is presented in Figure 5.23.

Reducing the transonic drag due to compressibility effects is equivalent to increasing the drag-divergence Mach number. One possible way of doing this is to use transonic area ruling.

The wave drag in the transonic and supersonic range has been shown to be quite significant in magnitude. One simple method for predicting it is the area-rule concept.

> Area rule: The flow about a low aspect-ratio wing-body combination at transonic and supersonic speeds is similar to the flow about a body of revolution having the same distribution of cross-sectional area.

According to this rule, it can be assumed that at large distances from the body the disturbances are independent of the arrangement of the components and only a function of the cross-sectional area distribution. This means that the drag of a wing-body combination can be calculated as though the combination were a body of revolution with equivalent-area cross sections.

The area-ruled method also indicates the most desirable way to arrange the vehicle components for minimum wave drag at a particular value of M_∞.

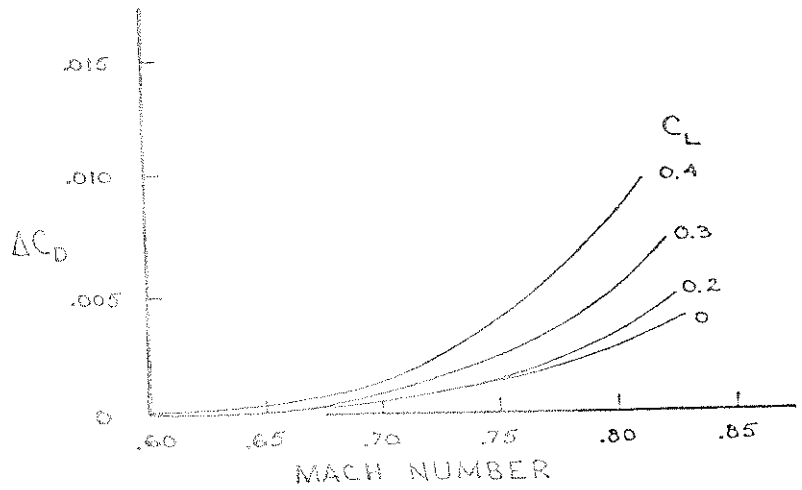

Figure 5.23 Learjet Model 25 Compressibility Drag (Taken from Ref. 5.14)

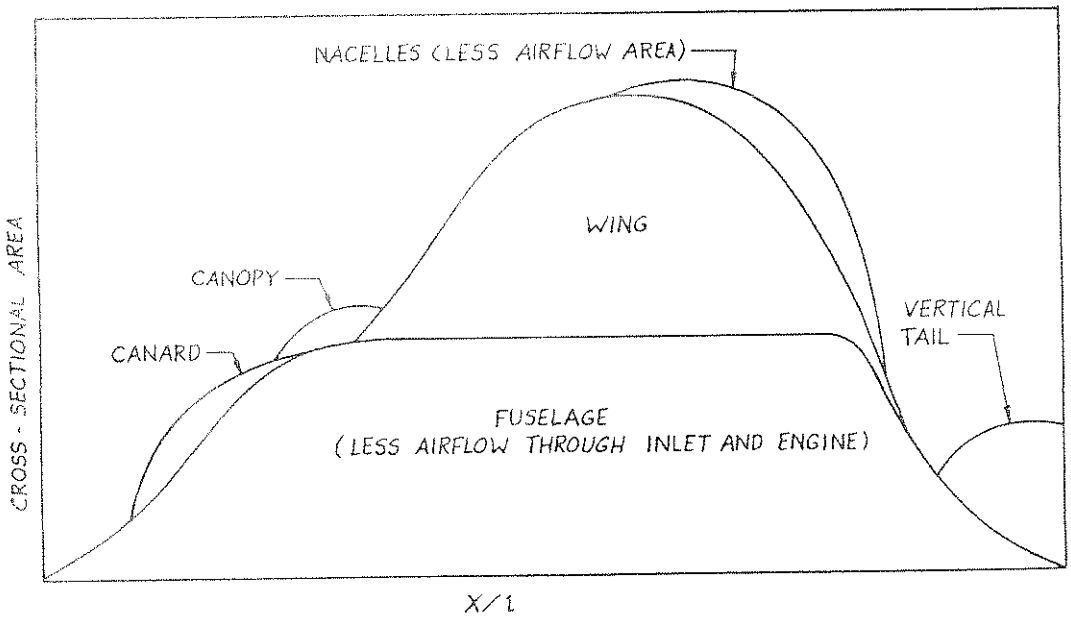

Figure 5.24 Typical Cross-Section Area Distribution for an Aircraft Before Area-Ruling

What is needed is a smooth equivalent body of revolution. The theoretical body of revolution with minimum wave drag is the Sears-Haack body described by(Ref. 5.15):

$$\left(\frac{r}{r_{max}}\right)^2 = \left[1 - \left(\frac{2x}{\ell}\right)^2\right]^{3/2}, \quad -\frac{\ell}{2} \leq x \leq \frac{\ell}{2} \tag{5.20}$$

The correponding volume and wave drag are given by:

$$\text{Volume} = \frac{3}{16}\pi \ell A_{max} \tag{5.21}$$

$$C_{D_{wave}} = \frac{9}{2}\frac{\pi}{\ell^2} A_{max} \tag{5.22}$$

where A_{max} is the maximum cross-sectional area. Following this idea, the cross-sectional area of the fuselage must be reduced in the region of other components, such as wing, tail, etc. A typical distribution of cross-sectional area of an airplane is shown in Figure 5.24.

The drag level for the complete airplane configuration is usually higher than that of the equivalent body of revolution. A typical comparison is presented in Figure 5.25 (Ref. 5.17).

When placing bodies on wings (i.e. a tiptank) or close to a fuselage (i.e. center engine nacelle on the DC10) a lot of attention needs to be paid to transonic effects on interference drag. Local area-ruling is then often applied. Examples are the NF5 tiptank and the DC10 center-engine!

5.2.6 TRIM DRAG, $(\Delta C_D)_{TRIM}$

Trim drag is defined as the drag induced by the horizontal tail to trim the airplane for $C_m = 0$. It does not include the tail profile drag which is accounted for in overall airplane zero lift drag. Typically, trim drag may vary from 0.5 to 5 percent of total airplane cruise drag, depending on airplane type and C.G. locations.

For conventional airplanes, the lift, drag and pitching moment coefficients can be written as:

$$C_L = C_{L_{WBV}} + C_{L_H}\frac{\bar{q}_H}{\bar{q}}\frac{S_H}{S_{ref}} \tag{5.23}$$

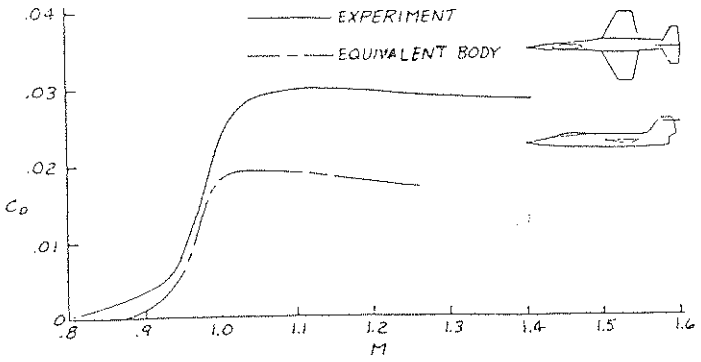

Figure 5.25 Comparison of Equivalent-Body Drag and Configuration Drag for an Airplane Configuration (Ref. 5.17)

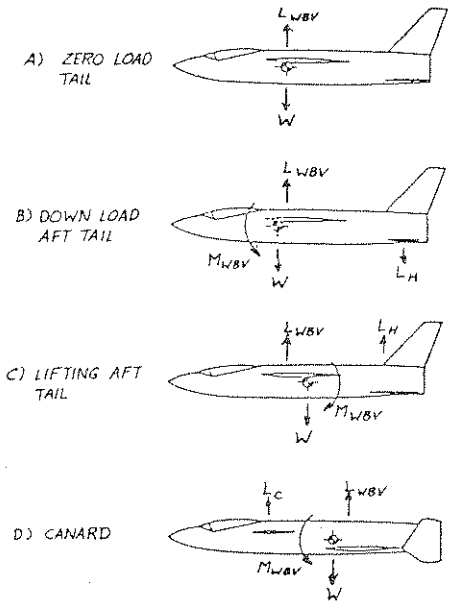

Figure 5.26 Effect of Center of Gravity and Wing-Body Aerodynamic Center Location on Lift Sharing $C_{M_o}=0$ (Taken from Ref. 5.18)

$$C_D = C_{D_o} + \frac{C_{L_{WBV}}^2}{\pi A_w e_w} + \frac{C_{L_H}^2}{\pi A_H e_H} \frac{\bar{q}_H}{\bar{q}} \frac{S_H}{S_{ref}} \tag{5.24}$$

$$C_m = \overline{C_{m_o}} (T_c) + C_m(T_c, \alpha, \delta_E, i_H) \tag{5.25}$$

where $\bar{q}_H$ is the dynamic pressure at the tail, T_c the thrust coefficient, δ_E the elevator deflection angle and i_H the tail incidence angle. In addition, all coefficients depend on the airplane geometry and on the C.G. location. Note that tail lift required to trim the airplane in pitching may be positive or negative. In either case, the drag coefficient is increased by it in accordance with Eqn. (5.24). However, the airplane lift coefficient is reduced by a negative C_{L_H}.

It follows that lift-drag ratio is decreased by a tail carrying negative lift.* Whether a tail is required to generate positive or negative lift depends on whether C_m about C.G. is positive or negative. The sign of C_m about C.G. in turn depends on:

1. C.G. location
2. Thrust coefficient and thrustline orientation
3. Airplane Shape (wing and fuselage camber)

5.2.6.1 C.G. Effect

The effect of C.G. location on tail lift is illustrated in Fig. 5.26. It is seen that with a forward C.G., the wing-body pitching moment is negative, thus requiring a negative tail lift to trim. In addition, a forward C.G. location increases the moment arm so that the pitching moment is more negatively large as compared with the aft C.G. case. This implies that the elevator deflection angle will be comparatively larger. On the other hand, as the C.G. is moved aft, the pitching moment about C.G. may become positive (usually with a small magnitude), so that a small positive tail lift is required to trim.

An example showing the magnitude of trim drag is presented in Fig. 5.27.

5.2.6.2 Thrust Effect

Fig. 5.28 shows the importance of thrust coefficient on C_m. As can be seen, increasing thrust coefficient is favorable.

*This is true unless the change in tail lift to trim results in a more favorable total wing and tail spanwise lift distribution according to Munk's staggerwing theorem. (Ref. 5.7)

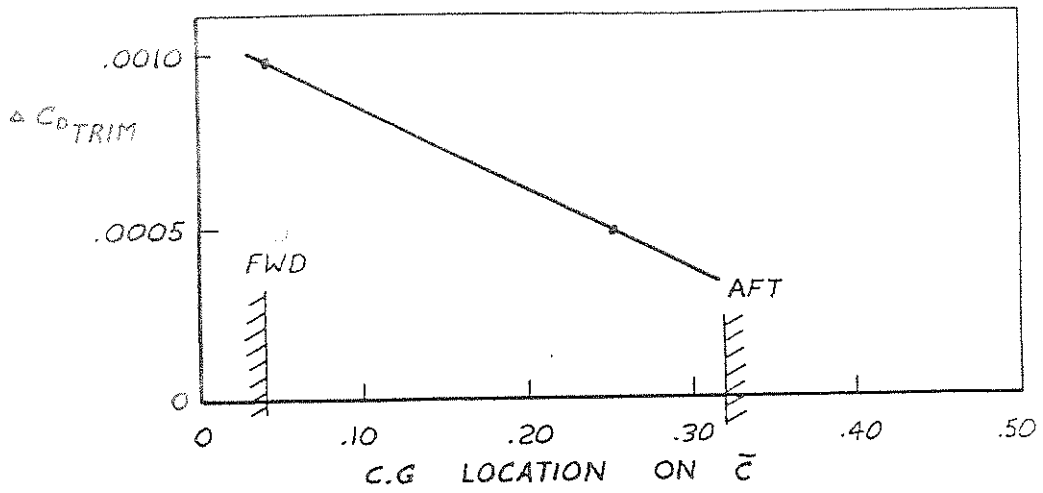

Figure 5.27 Example of Trim Drag Variation with Center of Gravity Location

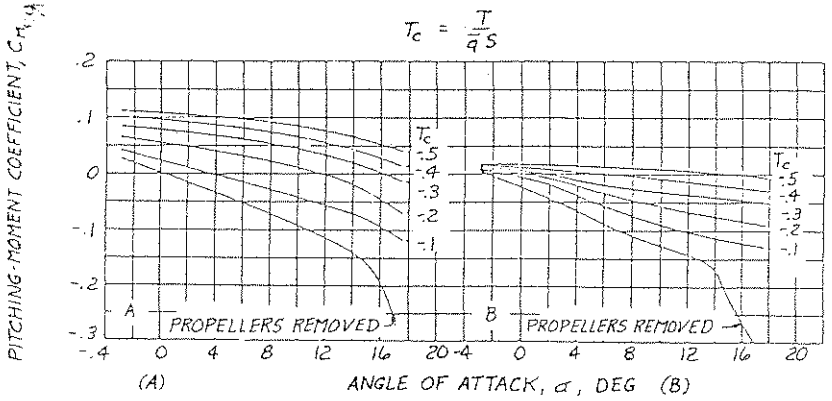

Figure 5.28 Effect of Propeller Operation on the Pitching-Moment Coefficient (Ref. 5.29)

The tilting of the thrustline mainly affects $\bar{C}_{m_o}$ in Eqn. (5.25).

Proper tilting of the thrustline to make $\overline{C_{m_o}}$ more positive depends on the vertical location of the thrustline relative to C.G.

5.2.6.3 Airplane Shape

The airplane shape (wing and fuselage camber) affects mainly $\overline{C_{m_o}}$. One possible way of making $\overline{C_{m_o}}$ as close as possible to being positive is to introduce fuselage camber. An example of an airplane with a significant amount of fuselage camber was the Lockheed Constellation shown in Fig. 5.29.

5.2.7 SUMMARY AND TYPICAL EXAMPLES

Fig. 5.30 shows two types of drag breakdown for a typical jet transport airplane:

a) component breakdown

b) causal breakdown

Table 5.2 presents the drag breakdown for a Learjet model 25. Fig. 5.31 shows some examples of what a drag "clean-up" program can achieve on a given airplane. It is seen that attention to detail can result in significant total drag reductions. Whether or not such drag reductions are 'cost-effective' can only be determined after combined cost-performance trade-offs have been made.

5.3 WIND-TUNNEL TESTING

The wind tunnel is an indispensable (and cost-effective) tool for predicting the full-scale aerodynamic characteristics and for configuration design optimization, particularly with regard to drag. Wind tunnels provide an excellent experimental way in which a systematic drag "build-up" can be realistically obtained.

Figs. 5.32, 5.33 and 5.34 provide the reader with some insight in the detailed construction of a modern wind tunnel model for a high subsonic jet trainer. With such detailed components a complete "component build-up" of drag and all other important aerodynamic characteristics of the airplane can be measured. Fig. 5.35 shows the assembled (clean) model installed in a windtunnel.

The installation of Fig. 5.35 is referred to as a "sting-type" installation. Another popular type of installation is the so-called "strut-type" installation. Fig. 5.36 illustrates a typical strut installation. Table 5.3 summarizes some advantages and disadvantages of each type of installation.

Figure 5.29 Example of Fuselage Camber on the Lockheed Constellation

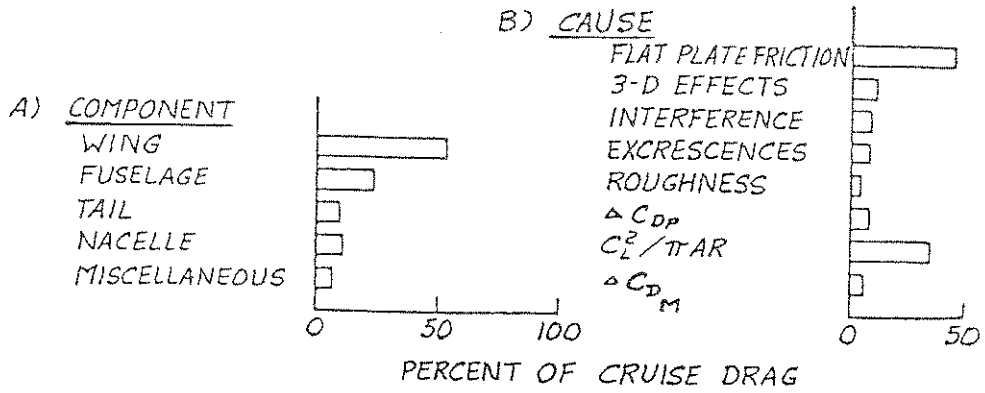

Figure 5.30 Typical Drag Build up for a Jet Transport Airplane

Table 5.2 Learjet Model 25 Drag Breakdown (Ref. 5.14)

(a) Cruise Drag Breakdown

M = 0.75 C_L = 0.336 C_D = 0.0338

Source	ΔC_D	% of Total
Profile drag (skin friction)	.0180	53.25
Profile drag variation with lift	.0007	2.07
Interference drag	.0031	9.17
Roughness and gap drag	.0015	4.44
Induced drag	.0072	21.30
Compressibility drag	.0028	8.28
Trim drag	.0005	1.48
Total	0.0338	100.00

(b) Profile Drag Breakdown

C_{D_P}, Profile Drag = 0.0180

Item	% of ΔC_{D_P}	ΔC_{D_P}
Wing	29.57	.0053
Fuselage	34.95	.0063
Tip Tanks	11.83	.0021
Tip Tank Fins	0.54	.0001
Nacelles	6.45	.0012
Pylons	1.61	.0003
Horizontal	9.14	.0016
Vertical	5.91	.0011
Total	100.00%	0.0180

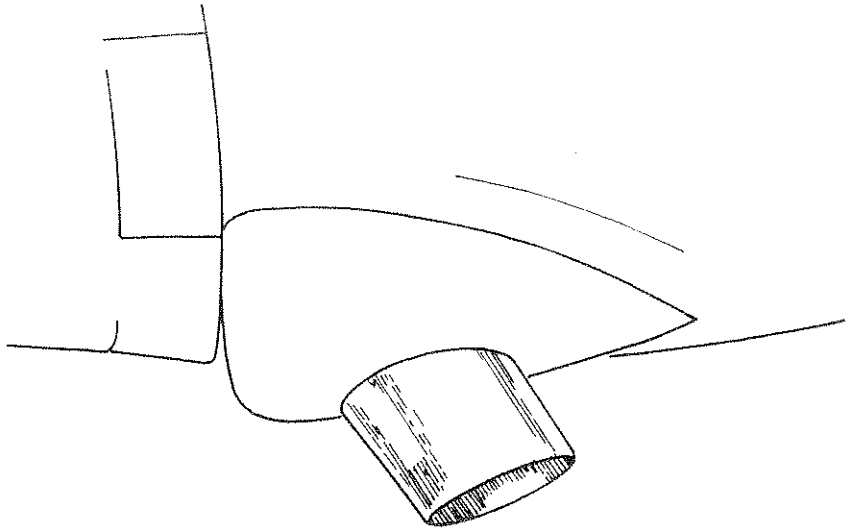

$C_D = 0.0021$ or 16% C_{D_f}

(Exhaust stacks protrude into the airstream)

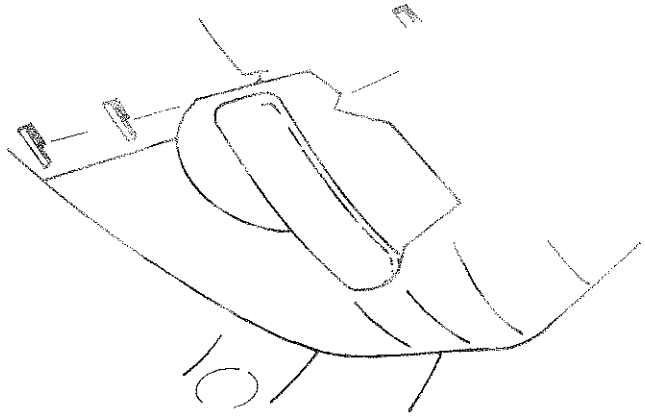

$C_D = 0.0009$ or 7% C_{D_f}
Full Length Fairing, Not Sealed

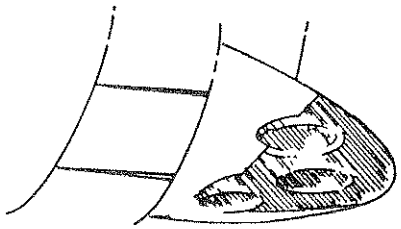

$C_D = 0.0010$ or 8% C_{D_f}

(Cooling air is ejected almost normal to the airstream)

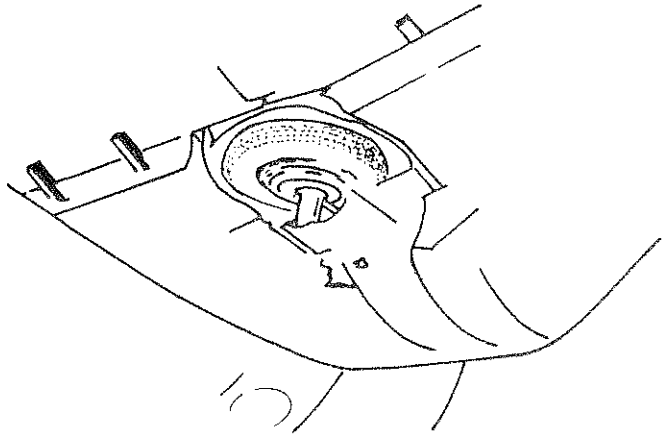

$C_D = 0.0012$ or 9% C_{D_f}
Short Length Fairing

(Drag from retracted landing gears)

Figure 5.31 Examples of Drag Reductions Attainable by Careful Attention to Details (Ref. 5.13)

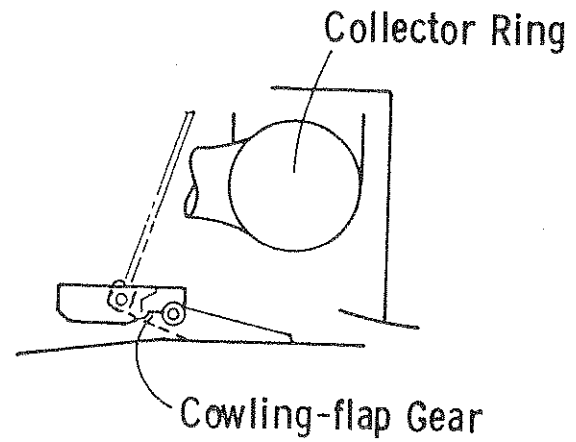

Section at Original Cowling Inlet

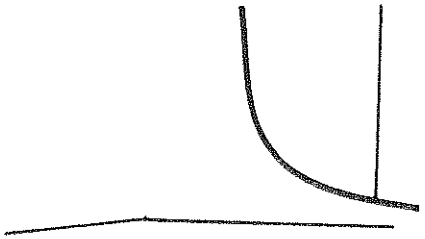

$\Delta C_D = 0.0007$ or 5% C_{D_f}

Section at Smooth Cowling Outlet

(to reduce cooling drag)

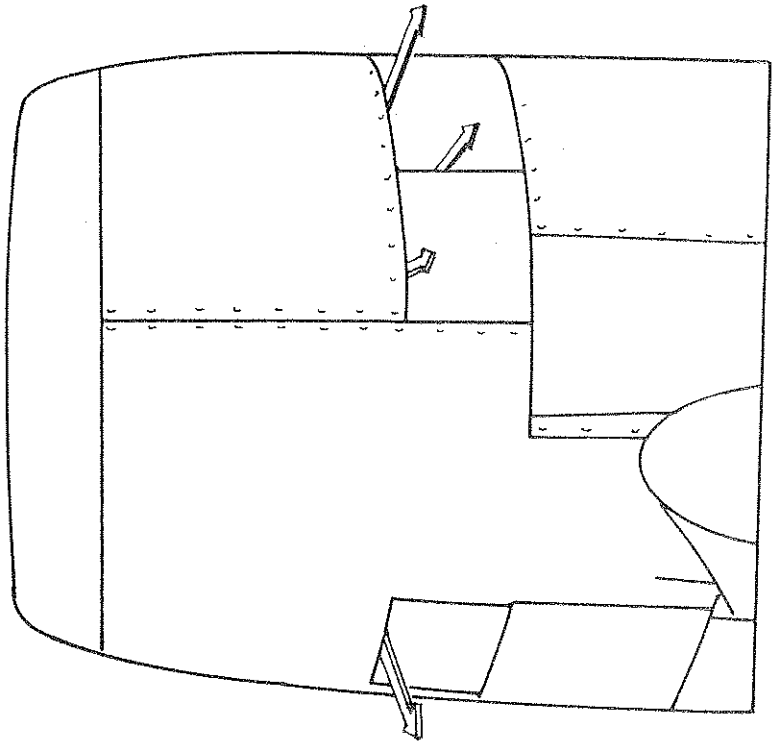

$\Delta C_D = 0.0005$ or 4% C_{D_f}

(Cowling flap leakage drag)

Figure 5.31 (Continued) Example of Drag Reductions Attainable by Careful Attention to Details (Ref. 5.13)

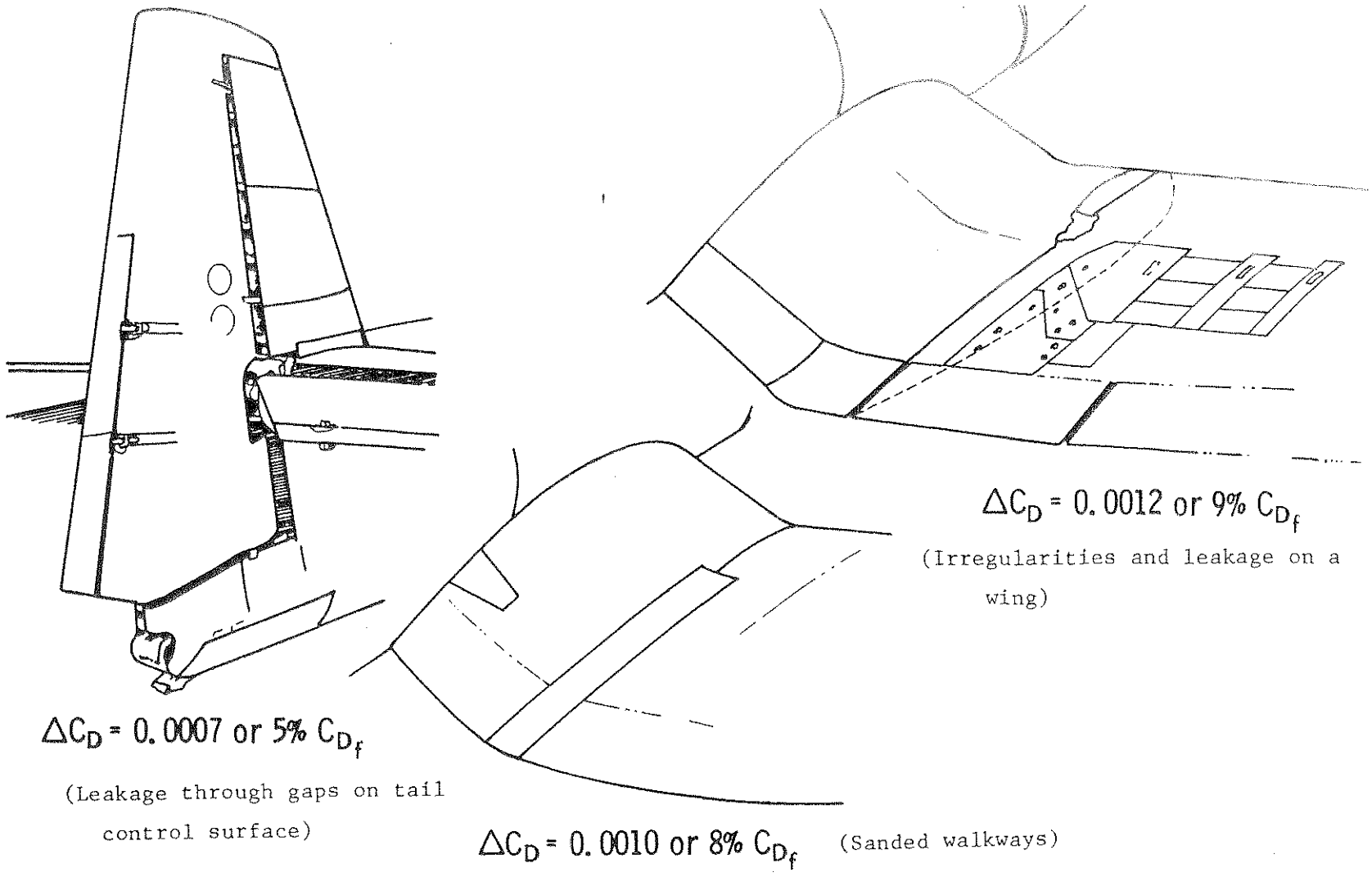

Figure 5.31 (Continued) Example of Drag Reductions Attainable by Careful Attention to Details (Ref. 5.19)

Figure 5.32 Example of a Windtunnel Model for the S211 Jet Trainer Airplane (Courtesy of SIAI-Marchetti, Sesto Calende, Italy)

Figure 5.33 Example of Wing, Wing Flap and Empennage Breakdown for a Windtunnel Model of the Jet Trainer Airplane (Courtesy of SIAI-Marchetti, Sesto Calende, Italy)

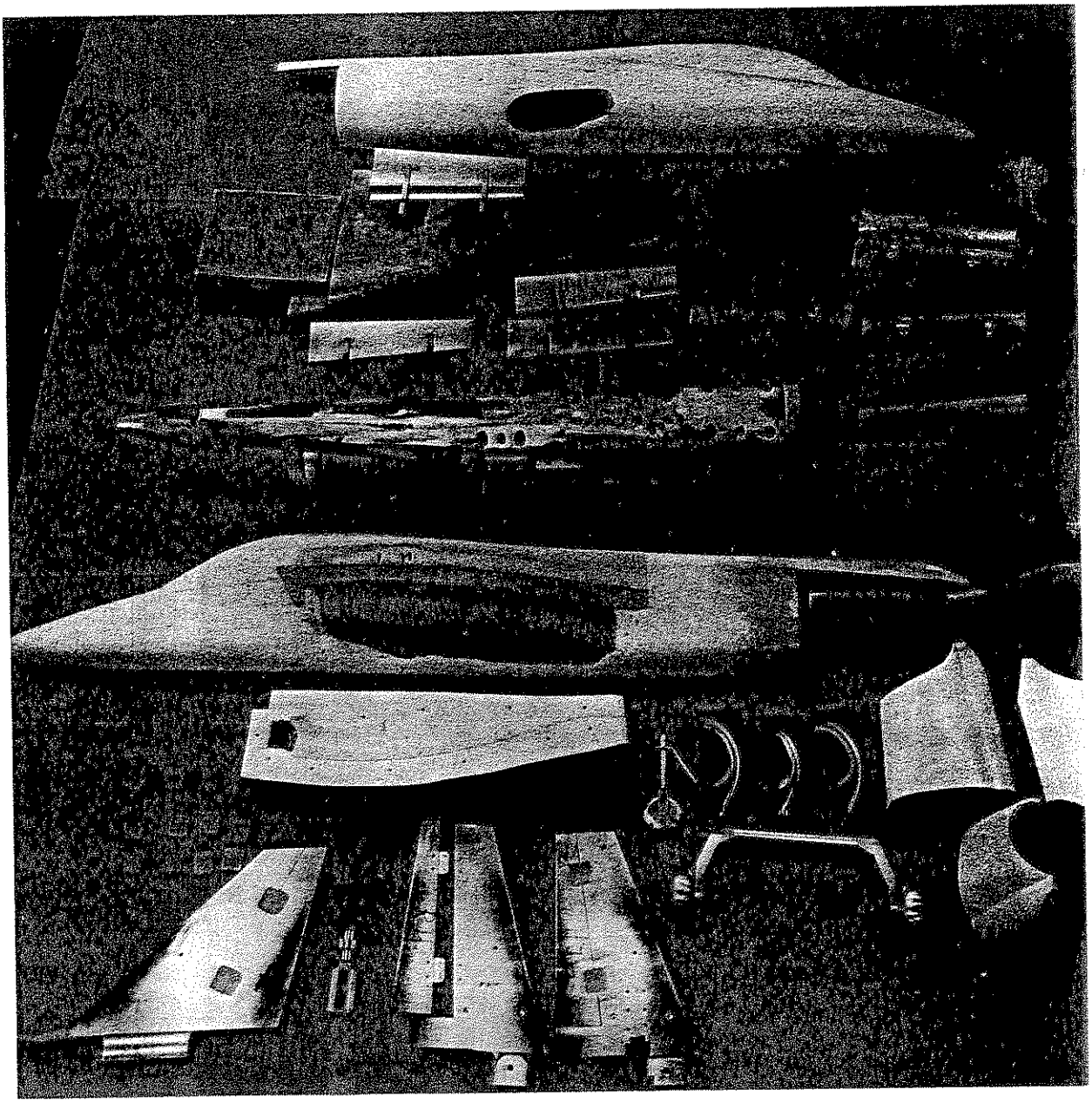

Figure 5.34 Example of Component Breakdown for a Windtunnel Model of S211 Jet Trainer Airplane (Courtesy of SIAI-Marchetti, Sesto Calende, Italy)

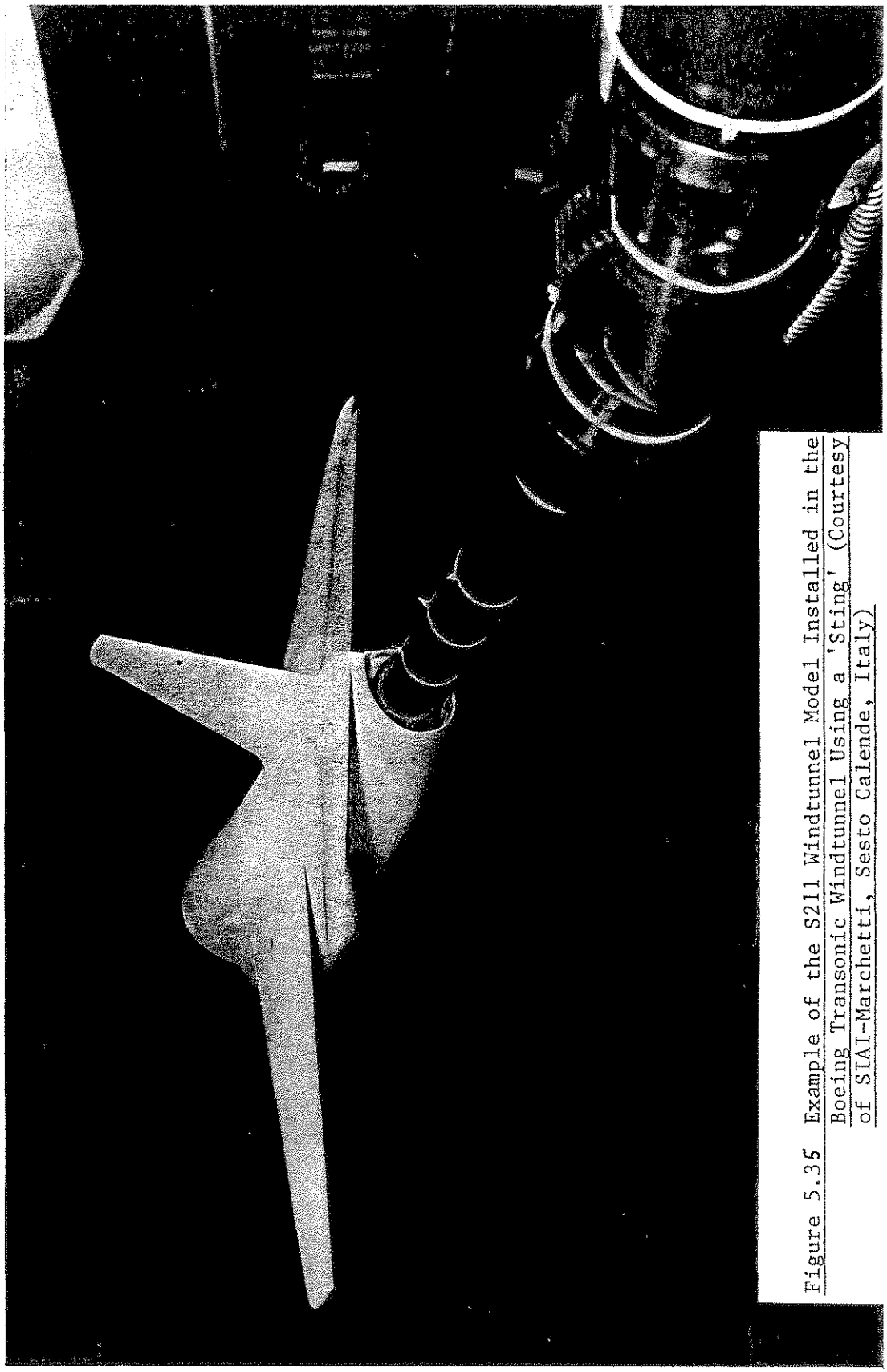

Figure 5.35 Example of the S211 Windtunnel Model Installed in the Boeing Transonic Windtunnel Using a 'Sting' (Courtesy of SIAI-Marchetti, Sesto Calende, Italy)

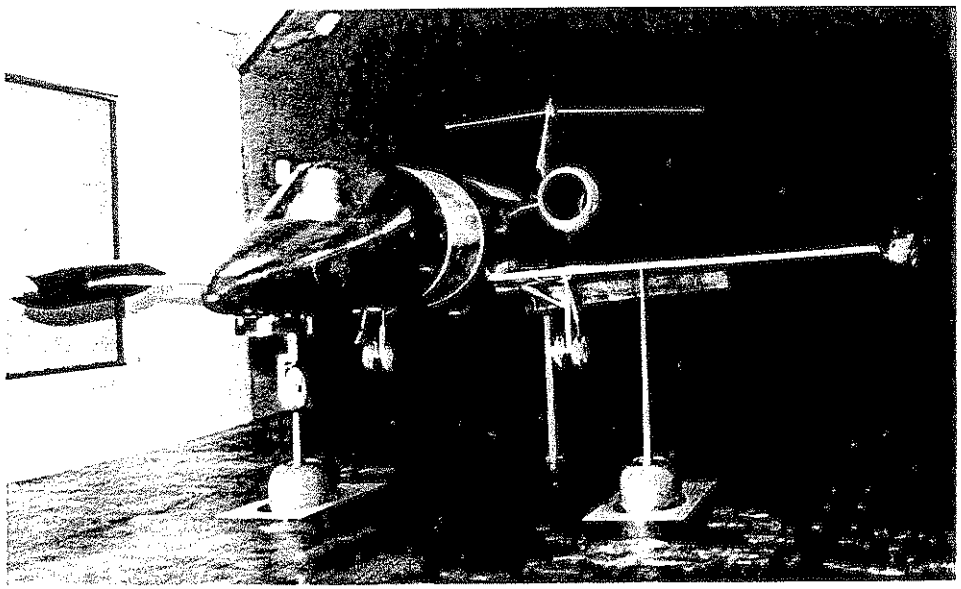

GLC Model 35/36 with Ground Plane

Figure 5.36 Example of a Model Installation Using Struts

Table 5.3 Summary of Advantages and Disadvantages of Sting- and Strut-Type Wind Tunnel Model Installation

	Sting-Type (Fig. 5.35)	Strut-Type (Fig. 5.36)
ADVANTAGES	• No strut interference. This is particularly important for high speed and sideslip testing. • Internal balance.	• No model distortions are required.
DISADVANTAGES	• Rear end model distortions are often needed to accommodate the sting.	• Limited to low speed testing • External balance.

With each model installation some means to measure the three forces and three moments which act on a model must be provided. Fig. 5.37 shows two examples of "internal" strain-gauge balance which are usually employed with "sting"-type model installations. Fig. 5.38 shows an example of an "external" strain-gauge balance which is usually employed with "strut"-type model installations.

The reader is cautioned in general not to use drag or lift data obtained from a wind tunnel test directly. Several corrections are required.

Refs. 5.20 and 5.21 provide detailed discussions for subsonic and supersonic wind tunnel testing and data reduction procedures.

In reducing wind tunnel data for the purpose of predicting the full-scale characteristics, the following steps are important:

(1) Corrections of the data to account for the weight of the model (tares).
(2) Corrections of the data to account for the differences between the flow field in the tunnel and that in free flight.
(3) Extrapolation of the corrected model data to the flight regime of the full-scale airplane.

In the first corrections careful attention must be paid to the weight difference between various model configuration. It will be necessary to take weight tares before each run with a new configuration model.

Corrections of type 1 are discussed in detail in Ref. 5.20.

In the second step, three types of corrections are required:

(a) Tunnel wall corrections to account for the effect of the limited size of the test section.
(b) Corrections to account for the effects of the model suspension system (aerodynamic interference, elastic deflections), and
(c) Corrections to account for imperfections of the tunnel flow.

In corrections of type 2 the effect of turbulence produced in the wind tunnel by the tunnel propellers, the guide vanes, etc. should be included. One way to indicate the degree of turbulence in the wind tunnel is by the use of the turbulence factor (T.F.).

It is known that the critical Reynolds number of a sphere tested in the free air is about 385,000. At this Reynolds number the laminar separation point and the boundary layer transition point coincide. The drag coefficient (based on cross-sectional area)

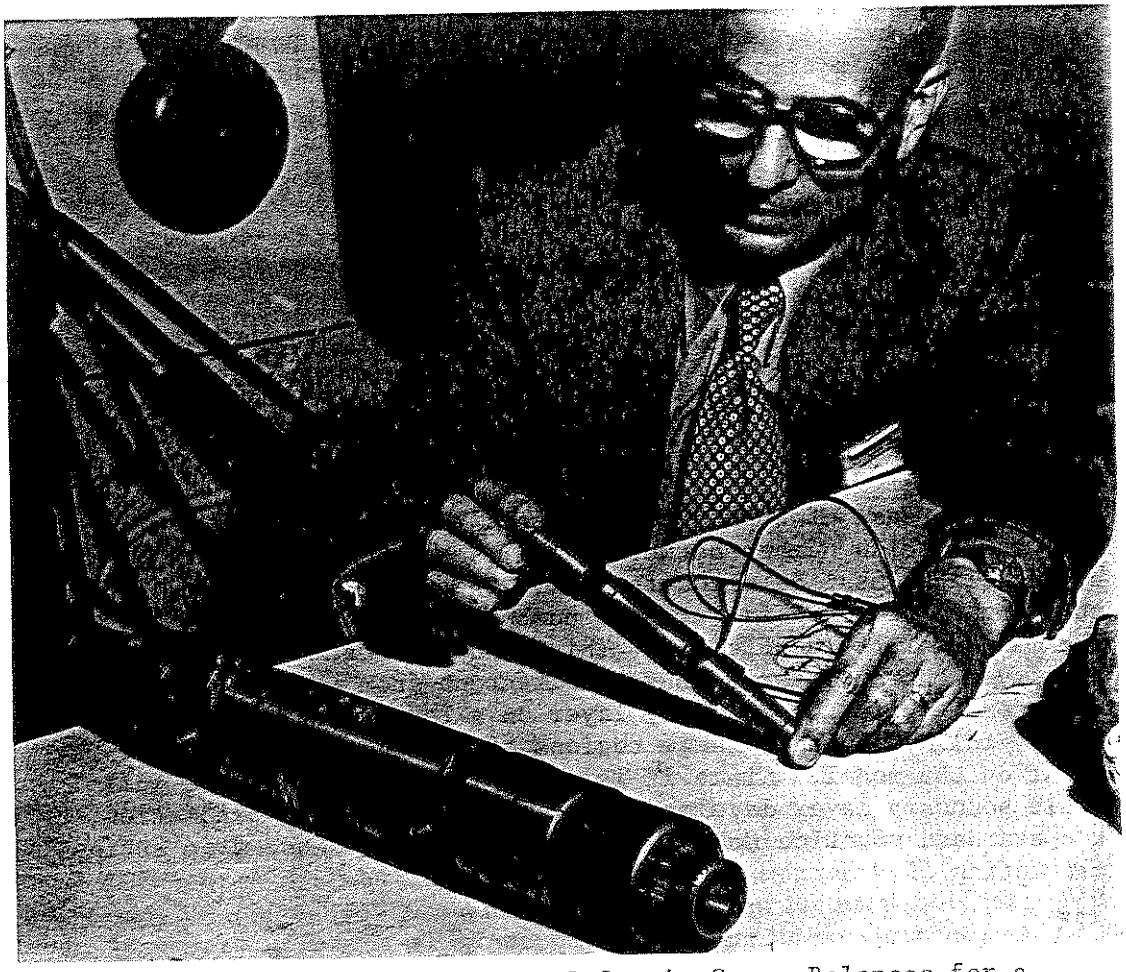

Figure 5.37 Examples of Internal Strain Gauge Balances for a 'Sting'-Type Model (Courtesy of SIAI-Marchetti, Sesto Calende, Italy)

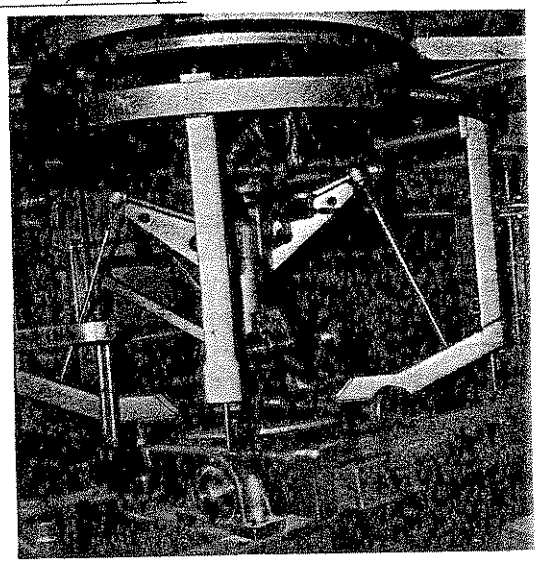

Figure 5.38 Example of an External Strain Gauge Balance System

at this critical Reynolds number is 0.30. If the sphere is now tested in the wind tunnel, the critical Reynolds number at which C_D is 0.30 (based on maximum cross-sectional area) will be denoted by R_{N_C}. The turbulence factor is then defined as:

$$T.F. = \frac{385,000}{R_{N_C}} \tag{5.26}$$

The effective Reynolds number (R_{N_e}) under any testing condition will be:

$$R_{N_e} = (T.F.) \times R_N \tag{5.27}$$

In the case of type 3 corrections, the sometimes large difference in Reynolds number between (small scale) wind tunnel and (full scale) flight must be accounted for. The most important effect of the large difference in Reynolds number is on the drag level and on the maximum lift coefficient. This is because the full-scale boundary layer characteristics may be different from those on the model surfaces. While the boundary layer on a large aircraft is often nearly fully turbulent, large regions of laminar boundary layer may exist on the model. Since it is essential to simulate the full-scale boundary layer development accurately for drag prediction, the standard practice to solve this problem is to use trip strips consisting of a narrow band of carborundum grit.

On the wing and tail, the trip strip is normally placed at about 5% to 10% chord. On the fuselage and on nacelles, the location is usually at about 5% length.

To be more precise, the trip location should be such that $R_{N_K} \geq 600$, where R_{N_K} is based on the roughness height K, the velocity at the top of the roughness U_K, and the kinematic viscosity at the top of the roughness ν_K (Ref. 5.22).

The method of artificially fixing transition on the tunnel model described above has been found to produce wing pressure distributions in good agreement with flight data in subcritical flow. In the supercritical flow range*, the problem of high Reynolds number simulation becomes far more complicated. This is because the turbulent boundary layer thickness must be correctly simulated at the location of the shock wave. If the trip strip is too far forward, the boundary layer will be unrealistically thick at the shock, so that the shock may be at the wrong position or a premature shock-induced separation may occur. Therefore, the trip strip is to be

---

* Defined as flow for which $M > M_{crit}$.

located further aft than the normal position to simulate properly the shock characteristics. The correct location may be calculated by theoretical methods or can be determined empirically. (Refs. 5.22 and 5.23).

It is expected that when the National Transonic Test Facility at NASA-Langley will become operational in the early 80's, significant improvements in transonic testing techniques will occur.

The upshot of all this is that after obtaining the tunnel model data, they must be corrected for the aforementioned Reynolds number effects. A possible way is to adjust C_{D_o} or $C_{D_{min}}$ according to the following equation:

$$\left(\frac{C_{D_{min}}}{C_f}\right)_{\substack{\text{wind}\\\text{tunnel}}} = \left(\frac{C_{D_{min}}}{C_f}\right)_{\substack{\text{full}\\\text{scale}}} \tag{5.28}$$

Another possible way is to calculate $C_{D_{min}}$ as:

$$C_{D_{min(\text{full scale})}} = C_{D_{min(\text{tunnel})}} - \Delta C_{D_{min}} \tag{5.29}$$

where $\Delta C_{D_{min}}$ is the decrease in turbulent skin friction due to the difference in Reynolds numbers. Fig. 5.11 can be used to find C_f (or) $\Delta C_{D_{min}}$ and any adjustment of the drag polar shape can be done empirically by comparing with polar shapes of existing similar airplanes.

Any methods used to account for Reynolds number effects must be checked against flight test data.

Detailed discussions of other corrections are beyond the scope of this text. However, they can be found in Ref. 5.20. The accuracy of extrapolating wind tunnel data to full-scale results is discussed in Ref. 5.24.

Because of the great importance of the effect of turbulence factor and of Reynolds number on skin friction drag the following example is presented.

Example 5.1 The drag of a wing model is measured at a test Reynolds number of 3×10^6 and a turbulence factor of 2.0. The measured drag coefficient is 0.0082. Find the equivalent free-air drag coefficient if the full scale Reynolds number is 9×10^6. Assume zero Mach number.

Solution: The effective Reynolds number is given by Eqn. (5.27):

$$R_N = 2.0 \times 3 \times 10^6 = 6 \times 10^6$$

Using the flat-plate solution of Eqn. (2.97) for turbulent flow, the drag coefficient correction can be obtained as:

$$\Delta C_D = 2.0\left\{\frac{0.455}{(\log_{10}6\times10^6)^{2.58}} - \frac{0.455}{(\log_{10}3\times10^6)^{2.58}}\right\} = -0.0008$$

Hence, the equivalent free-air drag coefficient of the model is:

$$C_{D_{(R_N=6\times10^6)}} = 0.0082 - 0.0008 = 0.0074$$

Using Fig. 5.11 to correct for Reynolds number it is seen that:

$$\Delta C_{D_{min}} = 0.00325 \text{ (at } R_N=6\times10^6) - 0.00305 \text{ (at } R_N = 9\times10^6) = 0.0002$$

Therefore:

$$C_{D_{full\ scale}} = 0.0074 - 0.0002 = 0.0072$$

5.4 SIMPLIFIED METHOD FOR ESTIMATING DRAG POLARS OF CLEAN AIRPLANES

Although the build-up method discussed in Sections 5.2 and 5.3 with the help of the stated References will yield good drag prediction results, it is a very laborious and time consuming procedure.

The purpose of this section is to present a simple method to obtain a rapid estimate of airplane drag polars. The method is based on the so-called 'equivalent-flat-plate' drag of airplanes and assumes that the drag polar is parabolic:

$$C_D = C_{D_o} + \frac{C_L^2}{\pi Ae} \tag{5.29}$$

In this method C_{D_o} is assumed to be determined from:

$$C_{D_o} = \frac{f}{S_{REF}} \tag{5.30}$$

where f is the equivalent parasite area of the airplane. For clean

airplanes (flaps up, gears up, cooling flaps closed, speed brakes retracted), the factor f may be found from Fig. 5.39.

It is seen from Fig. 5.39 that to read f it is necessary to know the airplane wetted area S_{wet} and the equivalent skin friction coefficient C_f.

S_{wet} can be found from:

$$S_{wet} = S_{wet_{fuselage}} + S_{wet_{\substack{wing \\ hor.\ tail \\ vert.\ tail}}} + S_{wet_{nacelles}} - \Delta S_{wet_{intersections}} \qquad (5.31)$$

Values for $S_{wet_{fuselage}}$ and $S_{wet_{nacelles}}$ can be obtained from any reasonable airplane threeview. By plotting the body perimeter versus station and integrating under the curves (as sketched in Fig. 5.40) these wetted area contributions are easily obtained.

For the lifting surfaces it is recommended to use Eqn. (5.8).

The correction to S_{wet}, $\Delta S_{wet_{intersection}}$ is necessary whenever significant areas are counted 'twice' because of intersections of a wing with a fuselage, a nacelle with a wing or an empennage with a fuselage.

The choice of the level of C_f, the equivalent skin friction coefficient, depends on the production technology foreseen for the airplane. The user should not be overly optimistic about the level of aerodynamic smoothness that can be attained in practice. The specific airplane points in Fig. 5.39 have been entered to give the user a yardstick against which to judge his own airplane design when produced with the methods he foresees to be available.

For many airplanes, the value of 'e' in Eqn. (5.29) turns out to be:

$$e \approx .75 \qquad (5.32)$$

This value seems to be largely independent of wing aspect ratio as suggested by Table 5.4, at least for propeller driven airplanes.

Another empirical method for predicting various drag components of military airplanes in clean configuration is presented in Ref. 5.26. The method was derived by analyzing flight data of many military airplanes (mostly trainers and fighters).

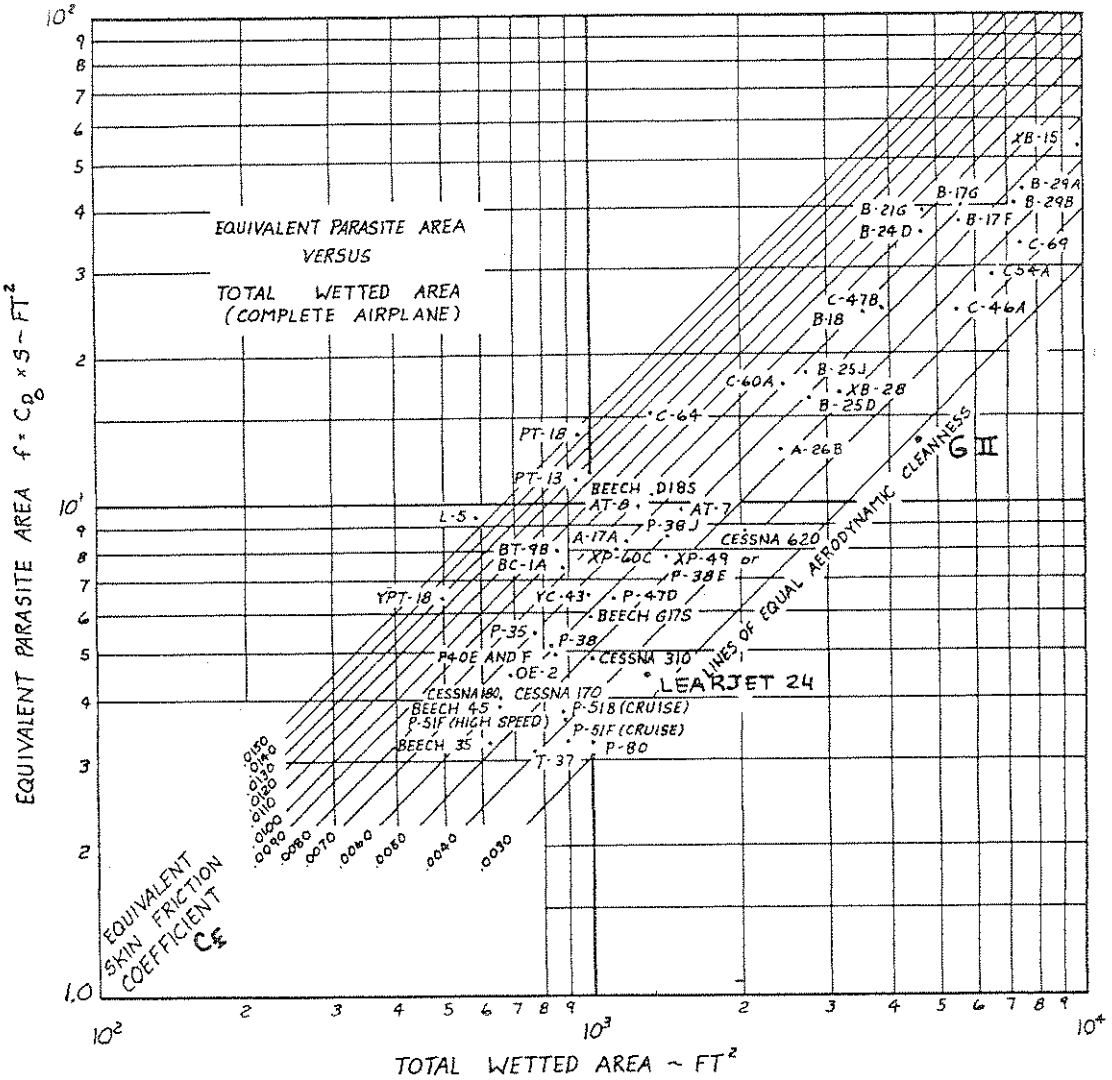

Figure 5.39 Determination of Equivalent Parasite Area

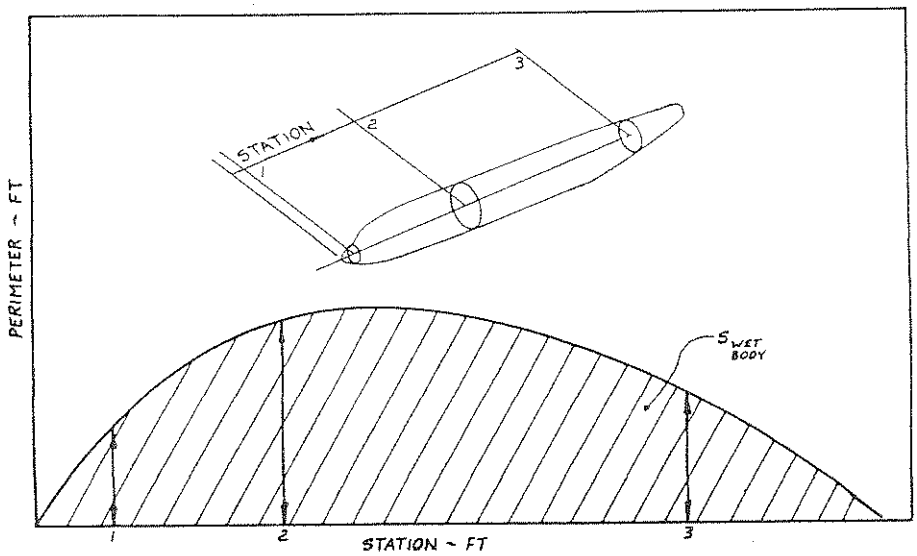

Figure 5.40 Method for Finding Wetted Area for a Body

Table 5.4 a) Summary of Drag Data for Propeller Driven Airplanes

Airplane	C_{D_o}	C_f	e	A	$L/D\|_{max}$
Douglas DC 3	.0249	.0062	.75	9.14	14.7
Boeing B17G	.0236	.0064	.75	7.58	13.8
Seversky P35	.0251	.0076	.75	5.89	11.76
Piper J3 'Cub'	.0373	.0090	.75	5.81	9.6
Beech D17 S (Stagger wing)	.0182	.0050	.75	4.18	11.7
Consolidated B-24J	.0406	.0096	.74	11.55	12.9
Martin B-26	.0314	.0078	.75	7.66	12.0
NAA-P51D	.0163	.0034	.75	5.86	14.6
Grumman F6F-3	.0211	.0049	.75	5.34	12.2
Lockheed 1049G	.0211	.0042	.75	9.17	16.0
Piper Cherokee	.0358	.0088	.76	6.02	10.0
Cessna Skyhawk	.0319	.0070	.75	7.32	11.6
Beech Bonanza V-35	.0192	.0045	.75	6.20	13.8
Cessna Cardinal RG II	.0223	.0049	.75	7.66	14.2
Cessna 310 II	.0267	.0056	.75	7.61	13.0

Data from Ref. 5.25.

TYPE	A	ℓ/d	$\pi d^2/4S_{REF.}$	$S_{WET}/S_{REF.}$	$C_{D_{c_r}}$	$C_{L\ L/D\ MAX}$	e	$(L/D)_{MAX}$
Narrow-body transports								
Boeing 707-320B	7.4	11.8	0.039	5.00	0.0131	0.51	0.85	19.40
McDonnell Douglas DC8-63	7.5	13.59	.051	5.95	.0156	.56	.85	17.92
Boeing 727-200	7.0	11.10	.072	6.29	.0173	.57	.85	16.42
Boeing 737-200	8.8	7.90	.121	6.72	.0190	.67	.85	17.59
McDonnell Douglas DC9-30	8.7	9.00	.111	6.93	.0196	.67	.85	17.23
Wide-body transports								
Boeing 747-100	7.0	10.30	0.069	5.95	0.0148	0.53	0.85	17.74
McDonnell Douglas DC10-30	7.6	8.70	.095	6.31	.0162	.57	.85	17.70
Lockheed L1011-1 Tristar	7.0	9.10	.088	6.23	.0161	.55	.85	17.02
(Europe) Airbus B2	7.7	9.20	.096	6.53	.0171	.59	.85	17.33
Business jets								
Gates Learjet 24B	5.0	8.7	0.085	6.00	0.0199	0.52	0.85	12.94
Grumman Gulfstream II	6.0	9.4	.072	5.80	.0172	.52	.85	15.25

1) ℓ = fuselage length
d = fuselage diameter

2) e = .85 was assumed for all airplanes

3) Data from Ref. 5.25

5.5 SUMMARY

This chapter has given the reader some insight in drag sources and drag prediction (theoretical, empirical and experimental) methods. The importance of airplane drag in determining the operating economy (fuel economy) cannot be overemphasized. Fig. 5.41 illustrates that a very large drag reduction potential still exists, particularly in the case of small airplanes. But even in the case of large airplanes, if complete laminar flow could be realized, Fig. 5.41 shows that significant drag reductions can still be obtained. The achievement of laminar flow will require much ingenuity, but in the light of increasing fuel costs, is worthwhile pursuing.

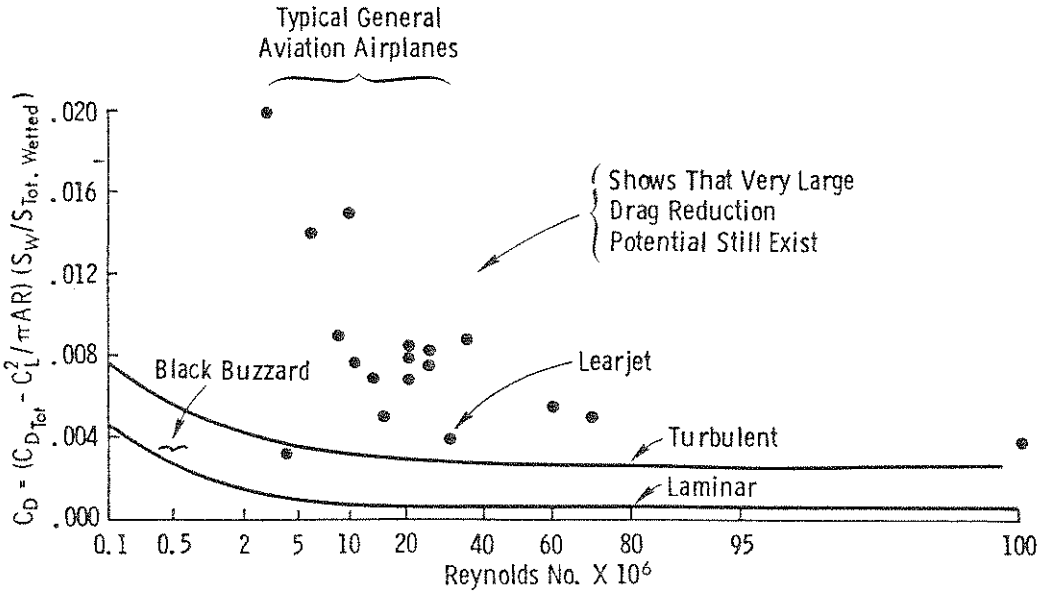

Figure 5.41 State-of-the Art and Theoretically Possible Drag Levels

Problems for Chapter 5

5.1 Verify Eqn. (5.2).

5.2 Show for Eqn. (5.3) that:

$$C_D \text{ for } C_L/C_D\Big|_{max} = 2C_{D_{min}} + \frac{2C_{L_{min}}^2}{\frac{\text{drag}}{\pi Ae}} - \frac{2C_{L_{min}}}{\frac{\text{drag}}{\pi Ae}} \times$$

$$\times \sqrt{\pi Ae\, C_{D_{min}} + C_{L_{min}}^2}$$

and

$$C_L \text{ for } C_L/C_D\Big|_{max} = \sqrt{\pi Ae\, C_{D_{min}} + C_{L_{min}}^2}$$

5.3 Show that for two airplanes having the same wing parasite drag coefficient and the same span efficiency factor, the total wing drag of one airplane can be related to that of the second airplane (called a reference airplane) at the same lift as follows:

$$D_w = D_{o_{WR}} \frac{S}{S_R} + (D_{WR} - D_{o_{WR}}) \frac{S_R}{S} \frac{A_R}{A}$$

where the subscript R indicates reference values.

5.4 Let:

$$r = \frac{D_W}{D_{WR}} \quad , \quad P = \frac{D_{o_{WR}}}{D_{WR}}$$

(1) Show that for rectangular wings, the equation in Problem 5.3 can be written as:

$$r = P \frac{bc}{b_R c_R} + (1 - P) \frac{b_R^2}{b^2}$$

(2) Given the following characteristics for a typical light airplane:

$$W = 2800 \text{ lbs},\ S = 174 \text{ ft}^2,\ A = 7.4,\ C_{D_{oW}} = 0.009$$

$$C_{D_{o_{BVH}}} = 0.017,\ e = 0.75,\ \text{cruise altitude} = 8000 \text{ ft}$$

Determine P for this airplane at the cruise altitude.

(3) If D_T is the total airplane drag, then:

$$D_T = rD_{WR} + C_{D_{o_{BVH}}} \bar{q} S$$

$$D_{T(R)} = C_{D_R} \bar{q} S_R = (C_{D_{oW}} + C_{D_{o_{BVH}}} + \frac{C_L^2}{\pi e A_R}) \bar{q} S_R$$

Assume that $b = b_R$, but $c \neq c_R$. Calculate and plot $D_T/D_{T(R)}$ versus c/c_R for V = 100 mph and 200 mph at 8000 ft. altitude for $c/c_R = 0.4 \sim 1.0$.

5.5 In Problem 5.3, now assume that $c = c_R$. Show that if the span is reduced, there will be a decrease in drag only if:

$$P > \frac{2}{3} .$$

5.6 Assume that the pitching moment characteristics of a propeller-driven airplane are as shown in Fig. 5.28. If the elevator deflection will generate an incremental pitching moment coefficient given by:

$$\Delta C_m = C_{m_{\delta_E}} \delta_E ,$$

calculate and plot the elevator angle (δ_E) to trim versus the thrust coefficient for $\delta_f = 0$. Assume $C_{m_{\delta_E}} = -0.02$ per degree and $\alpha=0°$.

5.7 Test results for a jet trainer are as shown in Fig. 5.42. Determine the drag divergence Mach number (M_{DD}) at different C_L's by both Boeing and Douglas definitions.

References for Chapter 5

5.1 Hoak, D.E., "USAF Stability and Control Datcom," April 1978, Flight Control Division, Air Force Flight Dynamics Laboratory, Wright-Patterson Air Force Base, Ohio.

5.2 Hoerner, S.F., "Fluid-Dynamic Drag," published by the author, 1965.

5.3 Anderson, S.B., "General Overview of Drag," Page 11 in Proceedings of the NASA-Industry-University General Aviation Drag Reduction Workshop," Edited by Jan Roskam, University of Kansas, 1975.

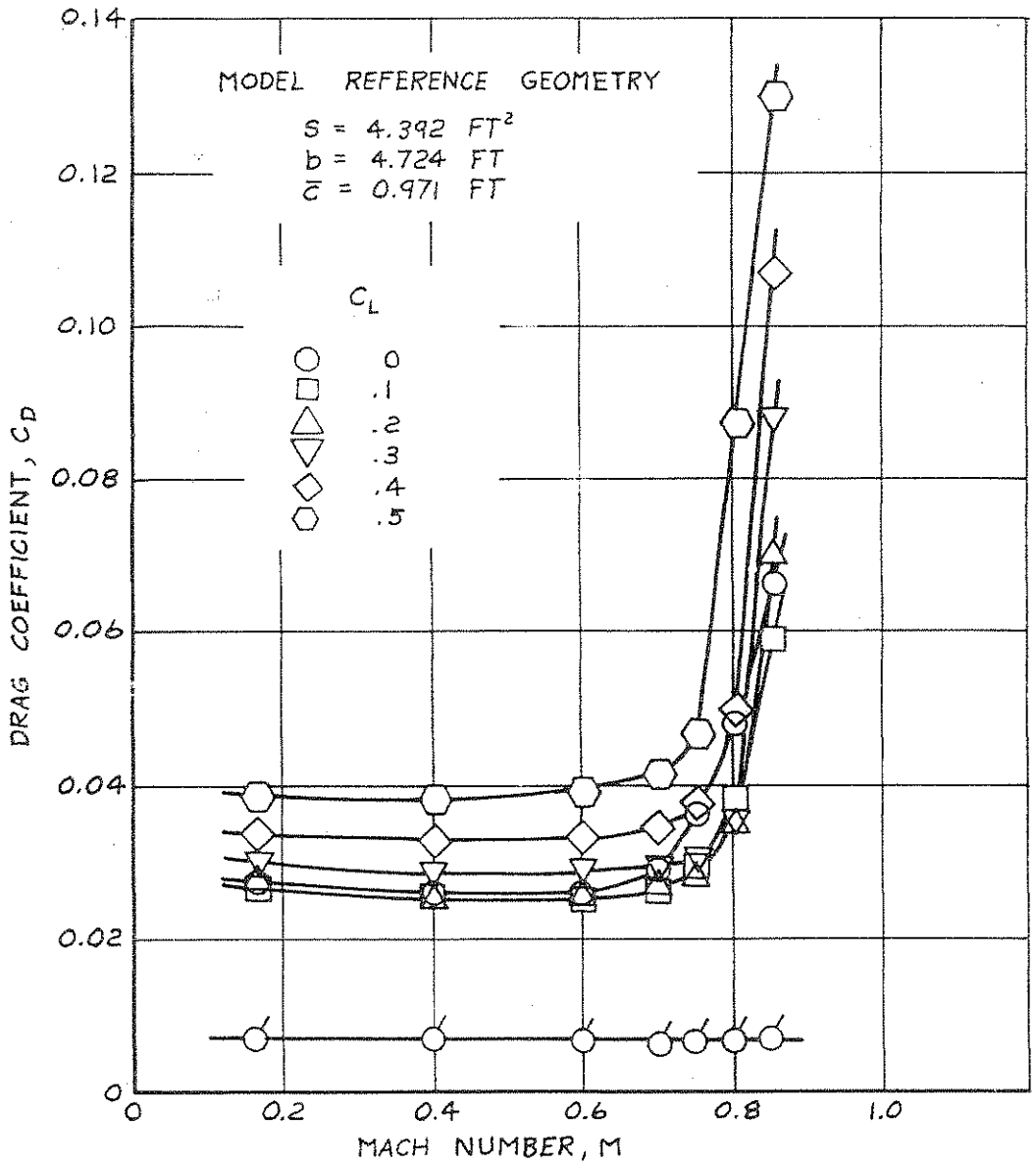

NOTE:

1) WBVH CONFIGURATION - $i_H = -2.4$

2) FLAGGED SYMBOL DENOTES BODY ALONE DATA

Figure 5.42 Drag Rise Data for a Small Jet Trainer